MULTI-FREQUENCY CONTACTLESS ELECTRICAL IMPEDANCE IMAGING USING REALISTIC HEAD MODELS: SINGLE COIL SIMULATIONS

A THESIS SUBMITTED TO
THE GRADUATE SCHOOL OF NATURAL AND APPLIED SCIENCES
OF
MIDDLE EAST TECHNICAL UNIVERSITY

BY

DOĞA GÜRSOY

IN PARTIAL FULFILLMENT OF THE REQUIREMENTS
FOR
THE DEGREE OF MASTER OF SCIENCE
IN
ELECTRICAL AND ELECTRONICS ENGINEERING

JANUARY 2007

Approval of the Graduate School of Natural and Applied Sciences.

Prof. Dr. Canan Özgen
Director

I certify that this thesis satisfies all the requirements as a thesis for the degree of Master of Science.

Prof. Dr. İsmet Erkmen
Head of Department

This is to certify that we have read this thesis and that in our opinion it is fully adequate, in scope and quality, as a thesis for the degree of Master of Science.

Prof. Dr. Nevzat G. Gençer
Supervisor

Examining Committee Members

Prof. Dr. Y. Ziya İder	(Bilkent Unv., EE)	
Prof. Dr. Nevzat G. Gençer	(METU, EE)	
Prof. Dr. B. Murat Eyüboğlu	(METU, EE)	
Prof. Dr. Mustafa Kuzuoğlu	(METU, EE)	
Assoc. Prof. Dr. Sencer Koç	(METU, EE)	

I hereby declare that all information in this document has been obtained and presented in accordance with academic rules and ethical conduct. I also declare that, as required by these rules and conduct, I have fully cited and referenced all material and results that are not original to this work.

Name, Last name :

Signature :

ABSTRACT

MULTI-FREQUENCY CONTACTLESS ELECTRICAL IMPEDANCE IMAGING USING REALISTIC HEAD MODELS: SINGLE COIL SIMULATIONS

Gürsoy, Doğa
Ms, Department of Electrical and Electronics Engineering
Supervisor: Prof. Dr. Nevzat G. Gençer

January 2007, 97 pages

Contactless electrical impedance imaging technique is based upon the measurement of secondary electromagnetic fields caused by induced currents inside the body. In this study, a circular single-coil is used as a transmitter and a receiver. The purpose of this study is twofold: (1) to solve the induced current density distribution inside the realistic head model resulting from a sinusoidal excitation, (2) to calculate the impedance change of the same coil from the induced current distribution inside the head model (forward problem). The Finite Difference Method is used to solve the induced current density in the head. The numerical solutions are compared with the analytical solutions for simple head geometries. The accuracy in the numerical solutions are found to be greater than 95%. The realistic head model is formed by seven tissues (cerebrospinal fluid, gray matter, white matter, fat, skull, muscle, skin) with a $1 \times 1 \times 1$ mm fine resolution. The electrical properties of the model (conductivity and permittivity) are assigned as a function of frequency. The

quasi-stationary assumptions, especially for head tissues, are explored. It is concluded that the displacement currents should not be neglected for head applications, whereas the propagation and inductive effects can be neglected below 10 MHz operating frequency. It is shown that, numerical solution of only the scalar potential is sufficient to obtain the induced current density in the head. This simplification not only reduce the excessive size of the solution domain, but also reduces the number of unknowns by a factor of 4. For higher frequencies $>$ 10 MHz (depending on the application) induction and propagation effects become important. Possible applications of this novel imaging technique are explored and it is found that, to distinguish the soft tissues of the brain (i.e., cerebellum, gray and white matter) the operating frequency should be $>$ 1 MHz. It is also observed that, for each frequency, there is a conductivity contrast relative to blood. Thus dynamic monitoring of hemorrhage at any frequency seems feasible. It is concluded that the methodology provides useful information about the electrical properties of the human head via contactless measurements and has a potent as a new imaging modality for different clinical applications.

Keywords: Magnetic induction, Electrical Impedance Imaging, Contactless Methods, Finite Difference Method, Successive Over Relaxation

ÖZ

GERÇEKÇİ KAFA MODELLERİ KULLANARAK ÇOKLU-FREKANS KONTAKSIZ ELEKTRİKSEL EMPEDANS GÖRÜNTÜLEMESİ: TEK BOBİN BENZETİMLERİ

Gürsoy, Doğa
Yüksek Lisans, Elektrik ve Elektronik Mühendisliği Bölümü
Tez Yöneticisi: Prof. Dr. Nevzat G. Gençer

Ocak 2007, 97 sayfa

Kontaktsız elektriksel empedans görüntüleme tekniği vücuda indüklenen akımların sebep olduğu ikinci elektromanyetik alanların ölçümü esasına dayanmaktadır. Bu çalışmada, hem verici hem de alıcı olarak çembersel tek-bobin kullanıldı. Bu çalışmanın amacı iki yönlüdür: (1) sinüsoidal uyarım sonucu gerçekçi kafa modelinin içinde indüklenen akım yoğunluğunu dağılımnın çözümlenmesi, (2) kafanın içinde indüklenen akım yoğunluğunu dağılımının aynı bobin üzerinde yarattığı empedans değişiminin ölçülmesi (ileri problem). Kafada indüklenen akım yoğunluğunun çözümlenmesinde Sonlu Farklar Yöntemi kullanıldı. Basit kafa modelleri için sayısal çözümler analitik çözümlerle karşılaştırıldı. Sayısal çözümlemelerdeki kesinlik 95%'in üzerinde bulundu. Yedi doku (Serebrospinal sıvı, gri madde, beyaz madde, yağ, kafatası, kas, deri) içeren $1 \times 1 \times 1$ mm çözünürlüklü gerçekçi kafa modeli oluşturuldu. Modelin elektriksel özellikleri (iletkenlik ve sığallık) frekansın bir fonksiyonu olarak atandı. Özellikle kafa dokuları için quasi-statik kabuller incelendi. Yerdeğiştirme akımlarının kafa

uygulamalarında ihmal edilemeyeceği ama bunun yanında yayılma ve indüktif efektlerin 10 MHz'in altındaki çalışma frekanslarında göz ardı edilebileceği sonucuna varıldı. Kafadaki indüklenen akım yoğunluğunu elde etmek için sadece skalar potansiyelin sayısal olarak çözümlenmesinin yeterli olduğu gösterildi. Bu basitleştirme, sadece çözüm domainini azaltmakla kalmayıp, bilinmeyenlerin sayısını da 4 kat oranında azaltmıştır. Daha yüksek frekanslarda (uygulamaya bağlı olarak) indüktif ve yayılma efektleri daha önem kazanır. Bu yeni görüntüleme tekniğinin olası uygulama alanları araştırıldı ve beynin yumuşak dokularını (örn., beyincik, gri ve beyaz madde) ayıştırmak için çalışma frekansının $> 1\ MHz$'in üzerinde olmasının gerektiği bulunmuştur. Ayrıca gözlenmiştir ki, her frekansta, kana göre iletkenlik kontrastı mevcuttur. Bu yüzden kanamanın her frekansta dinamik monitörlemesi olası görülmektedir. Bu metodun kontaktsız ölçümlerle insan kafasının elektriksel özellikleri hakkında işe yarar bilgiler edinilebileceği fikrine varılmıştır ve yeni bir görüntüleme modeli olarak farklı klinik uygulamalar için potansiyel kullanım alanı olduğu sonucuna varılmıştır.

Anahtar Kelimeler: Manyetik indüksiyon, Elektirsel Empedans Görüntüleme, Kontaksz Yntemler, Sonlu Farklar Yntemi, Successive Over Relaxation

To My Parents

ACKNOWLEDGMENTS

I would like to express my gratitude to my supervisor Prof. Dr. Nevzat Güneri Gençer for his guidance throughout the research. I would also wish to express my appreciation to Emre Arpınar for his advices and comments, as well as to Taha Ahi and Sedat Doğru for his assistances. Also I would like to thank to my laboratory partners and my friends Evren Değirmenci, Koray Özdal Özkan and İlyas Evrim Çolak for their encouragements. My special thanks are to Gözde Göksu who has a natural talent capable of keeping me motivated all the time and of course my parents for everything.

TABLE OF CONTENTS

LIST OF TABLES

TABLES

LIST OF FIGURES

FIGURES

CHAPTER 1

INTRODUCTION

Medical imaging modalities are indispensable for the clinical environments. The acceleration of imaging technologies in biomedical sciences has caused many conveniences for both research and medical purposes. However there are still many deficiencies of these existent modalities. Therefore additional effort should be maintained in order to improve the existing technologies or to develop new ones. In this study, a new imaging modality based on electrical impedance measurements will be presented. The safety considerations and application areas will be explored and feasibility of different applications will be investigated by simulations using realistic models.

1.1 Medical Imaging

Medical imaging is simply taking the pictures of the interior body for clinical or research purposes. From this point of view, medical imaging looks like photography. The difference between medical imaging and photography is that, photography concerns with the surface images of the objects where medical imaging tends to obtain interior images of the body.

In photography, in order to take a picture, the photographer needs light patterns directed to the object and the reflected or emitted light patterns from the object are recorded. As in photography most medical imaging techniques need a radiation source and try to form an image by using different interactions of the radiated field with body. Therefore all imaging modalities uses a specific

physical property of tissues that causes a change in the exposed radiated field.

There are several imaging modalities which are extensively used for clinical purposes. Currently, the widely preferred modalities are Ultrasonography, Computerized Tomography (CT) and Magnetic Resonance Imaging (MRI), as well as Mammography, Fluoroscopy, Positron Emission Tomography (PET), etc. for other specific applications. Each imaging modality has strengths and weaknesses. For example, Ultrasonography is extensively used to visualize soft tissues as muscles or internal organs, their shapes, and some pathological conditions. It is also capable of taking dynamic images and comparably cheaper than the other imaging modalities. The operation can easily be performed and no disadvantages have been reported yet. Similarly, CT is frequently used to diagnose cerebrovascular accidents which is known as stroke and intracranial hemorrhage. Additionally, CT is more sensitive to skull tissue and fractures of the skull can easily be diagnosed. Also it is used extensively for chest and abdomen imaging for the detection of cancerous tissues and to determine the stage of cancer. However high amounts of radiation exposed to the body can be a trigger for cancer development. Apart from other modalities MRI best distinguishes the brain tissues and used for diagnosing tumorous tissues inside the head. However, MRI is still the most expensive imaging modality.

The above mentioned modalities which are used for diagnosing purposes, can also be employed in therapeutic applications. For instance, Focused Ultrasound Surgery (FUS) or High Intensity Focused Ultrasound (HIFU) is used for heating and annihilating the pathological tissues. Similarly focused ultrasound is used to break up kidney stones. It also has application areas for cataract treatment to emulsify the lens of the eye.

In this section the Medical Imaging concept is introduced. Extensively used imaging modalities in clinical environments and their application areas are presented briefly. Next section will demonstrate the existing Electrical Impedance Imaging (EII) modalities in the literature.

1.2 Electrical Impedance Imaging

Electrical Impedance Imaging attempts to visualize the conductivity and permittivity distribution of the body by electrical measurements. Typically, currents are applied to the body and electrical measurements are obtained from the body surface. There are different variants of this technique depending on how the current is applied to the body and how the measurements are taken.

1.2.1 Basic Principles

In essence, the basis of EII approaches can be listed as follows:

1. Electrical impedances of body tissues are different from each other.

2. Tissue electrical impedances change as a function of frequency.

The first phenomenon was nearly known from the beginning of 20^{th} century [28] and leaded to the development of EII modalities. Later on, the second phenomenon lead to Multi-Frequency Electrical Impedance Imaging (MFEII) modalities. Table 5.1 shows the electrical impedance differences between several body tissues at 50 kHz and 10 MHz.

1.2.2 An Overview of EII Techniques

The earliest electrical impedance imaging technique is the Electrical Impedance Tomography (EIT). The term tomography (tomo-graphy) corresponds to "slice imaging". Thus EIT aims to reconstruct electrical impedance images of slices. For this purpose, currents are either applied from the electrodes attached on the body surface or induced by time-varying magnetic fields. For both cases, the voltages are measured using the surface electrodes which surrounds the body. The former one is named as Applied Current EIT (ACEIT), and the latter one is called Induced Current EIT (ICEIT).

In conventional ACEIT, currents are applied via electrodes attached on the body surface [10], [19], [21], [35]. However, current injection from the surface electrodes has some limitations that affects the performance of the

Table 1.1: The electrical properties of several body tissues at 50 kHz and 10 MHz.

	50 kHz		**10 MHz**	
	$\sigma(S/m)$	$\epsilon_r(H/m)$	$\sigma(S/m)$	$\epsilon_r(H/m)$
CSF	2.0000	109.0	2.0022	108.6
Gray Matter	0.1275	546.1	0.2917	319.7
White matter	0.0776	354.8	0.1585	175.7
Fat	0.0433	16.3	0.0526	29.6
Muscle	0.3518	1009.4	0.6168	170.7
Skin	0.0290	2187.6	0.3656	221.8
Skull	0.0206	26.4	0.0428	36.8
Inflated Lung	0.1027	4273.0	0.2252	123.7
Deflated Lung	0.2620	8531.0	0.4380	180.3
Heart	0.1954	16980.0	0.5014	293.5
Blood	0.7001	5198.0	1.0970	280.0
Breast Fat	0.0255	117.8	0.0280	7.9
Stomach	0.5337	3551.0	0.7844	246.4
Kidney	0.1594	11430.0	0.5081	371.1
Spleen	0.1179	5493.0	0.5057	440.5
Liver	0.0725	10690.0	0.3167	223.1

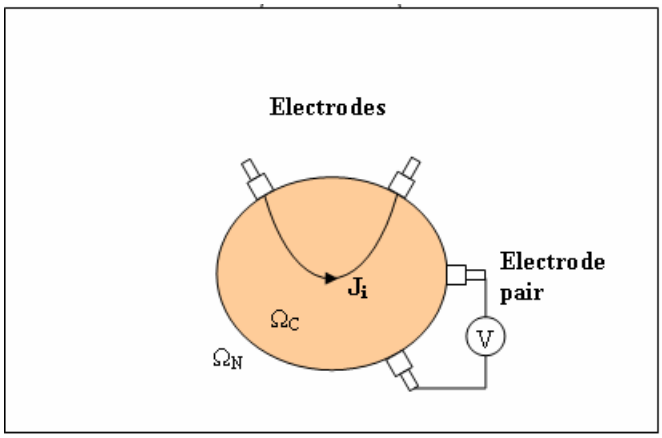

(a)

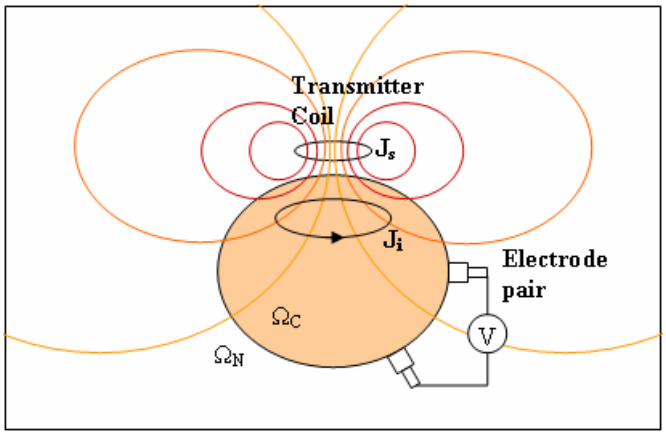

(b)

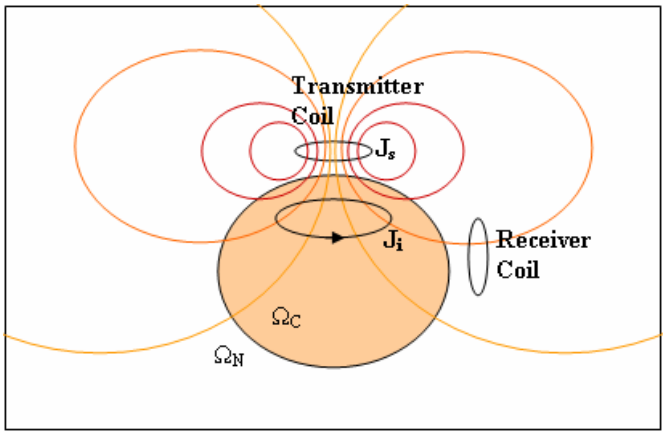

(c)

Figure 1.1: (a) ACEIT, (b) ICEIT, (c) CEII.

imaging system [22], [34]. In addition, an insulating layer (like bone) nearby the injection electrodes reduces the injected current strength in the deep-lying tissues. This is an important problem especially when the head is to be imaged.

In ICEIT, currents are induced into the body [22], [23], [27], [29], [34]. In that approach, it is possible to eliminate the screening effect of bones. In addition, by applying different magnetic fields it is possible to increase the number of measurements. This can be achieved by using different coil shapes or by changing the position of a given coil. In ACEIT the number of measurements can be increased by increasing the number of electrodes attached on the body surface. In that sense, ICEIT is more flexible compared to ACEIT. However, a common problem of both techniques is the attachment of electrodes to the body surface to measure the voltages.

In Contactless Electrical Impedance Imaging (CEII) the currents are applied via magnetic induction and the secondary electromagnetic fields are sensed via magnetic induction as well [6], [46], [49], [52], [61]. This eliminates the common problem of both techniques due to attachement of llarge number of electrodes on the body surface. In addition, the advantages of ICEIT over ACEIT are still maintained.

At present much research about EII is being concentrated on breast cancer detection and brain imaging. There were not much clinical applications for a long period of time, but in 1999, TransScan, a commercial EIT system is approved by Federal Drug Adminstration (FDA) in the USA to detect breast cancer. The electrode-based methods are still, however, not convenient for imaging head tissues because of the insulating skull layer.

1.3 Literature

Literature will be discussed in three main sections: Experimental studies, simulation studies and biomedical applications.

Table 1.2: Review of literature.

Group	Year	Frequency	Comments
Tarjan *et al.*	1968	100 kHz	First biomedical application. Monitoring cardiac activities and respirations are presented.
Hart *et al.*	1988	1-10 MHz	Single coil simulations and experiments.
Al Zeibak *et al.*	1993	2 MHz	Saline phantoms are used and backprojection is offered for image reconstruction.
Netz *et al.*	1993	100 kHz	Subsurface measurements via miniaturized coils.
Gencer *et al.*	1996	50 kHz	Feasibility for safety conditions are explored. 3D numerical model is developed based on Finite Element Method (FEM). An experimental system is realized. SVD is offered for image reconstruction.
Korzhenevskii *et al.*	1997	20 MHz	Simulations based upon a dipole field approximation and experimental realization.
Scharfetter *et al.*	2000	20-370 kHz	A hardware developed for multi-frequency measurements.
Morris *et al.*	2001	10 MHz	FD solver is developed
Merwa *et al.*	2003	700 kHz	3D FEM solutions are presented and feasibility of detecting brain oedema is discussed.
Watson *et al.*	2004	–	Array sensors are presented
Igney *et al.*	2005	–	Performance of array sensors are discussed.

1.3.1 Experimental Setups

In 1968, Tarjan and McFee, proposed this measurement approach for medical purposes, and built an experimental system to determine the effective electrical resistivity of the human torso and head at a single low frequency (100 kHz) [6]. The electrical conductivity fluctuations as a result of the cardiac activities and respirations were also presented [5]. This was the first contactless system used for impedance measurements and impedance monitoring in the literature.

In the previous studies Hart *et al.* used a single coil system, which operates at 1-10 MHz operating range [14]. A single coil system acting as a receiver and a transmitter was employed instead of using separate coils. The suggested methods for impedance measurements was an impedance meter based on a Collpits oscillator.

Netz *et al.* used a miniaturized differential coil system and showed that the system has an ability to detect cytotoxic oedema conditions in a head phantom [25].

Gencer *et al.* chose lower frequencies (<100 kHz) to cope with the difficulties arising from displacement currents and wave propagation delays [45]. A data acquisition system was developed and implemented [51], [61] at 11.2 kHz. It was shown that low frequency measurements can be used to detect electrical conductivities of biological tissues. The reconstructed images of saline filled glass tubes show the potent of this approach as a new subsurface imaging modality. The linearity of the system is found to be 7.2% at full scale and the sensitivity is found to be 21.47 $mV/(S/m)$ [77]. Multi-frequency measurements are also achieved [78]. Potential distribution of leech (Hirudo medicinalis) from the surface is obtained.

Korjenevsky *et al.* also realized a system employing 16 electronically switched excitation and detection coil units arranged in a circle [47], [49]. The carrier frequency of the system was 20 MHz and this was down-converted to 20 kHz for processing. The images of cylindrical objects with positive and negative conductivity contrast in a saline bath were presented in the same study. The objects, each with diameter 29 % of the array diameter, were clearly resolved

using a filtered-back projection algorithm. Korjenevsky and Sapetsky showed that reduced spatial distortion could be achieved when images were reconstructed by a neural network for some simple distributions of conductivity [50].

Scharfetter *et al.* implemented a new system that operates at relatively low frequencies (20-370 kHz) [52]. Multi-frequency measurements are established by using a potato. The measurement system consists of a solenoid transmitter, a planar gradiometer as a receiver and a sensitive phase detector [52], [72].

Watson *et al.* implemented a new sensor which in principle cancels the primary magnetic field by a single receiver mounted such that no magnetic flux runs through it, instead of using an additional back-off coil [65]. The implementation of an array system was demonstrated by Igney *et al.* by using array of receiving coils [75].

1.3.2 Simulation Studies

Korzhenevskii and Cherepenin presented a theoretical study of the two-coil arrangement and proposed the direct measurement of phase angle for detecting the conduction eddy currents [39]. A filtered-back projection algorithm is proposed for image reconstruction.

Gencer and Tek offered a subsurface imaging arrangement consisting of uniformly distributed 49 transmitter and 49 separate receiver coils above a conducting object. A three-dimensional (3D) FEM model was developed to solve the fields. To reconstruct conductivity images, the Newton-Raphson method was applied with the trucated SVD Pseudoinverse of the sensitivity matrix (that relates conductivity perturbations to the change in measurements) [46]. Images of single voxel perturbations were presented for a specific noise level in the measurements.

Morris *et al.* used the Finite Difference Method (FDM) to test the previous experimental setup realized by Griffiths *et al.* [44]. The numerical models and solutions obtained by Morris *et al.* [56] are used for simulation studies of this type of sensors compared the axial gradiometers [74]. The frequency is selected

between 1-10 Mhz.

Merwa *et al.* developed a FEM solver to test their agar experiments [60]. For the image reconstruction, the computation of sensitivity map is developed in order to be used in inverse solvers [69]. They proposed an inverse problem solver based on Newton-Raphson method to their experimental setup to reconstruct images, which they called 3D inverse eddy current solution [73].

1.3.3 Biomedical Applications

Diagnosing oedema is the most popular research area in this contactless method. Hart *et al.* realized a contactless sensor based on this method and proposed that the sensor can diagnose brain oedema at high frequencies [14]. They used a spherical head model with two tissue types, white and grey matter and they calculated the conductivity difference between the normal brain measurements and the measurements where the oedema is present. They modeled the oedema by either increasing the radius or the conductivity of white matter relative to grey matter. Netz *et al.* also worked on studies to show the feasibility of detecting the oedematous tissue of the brain [25]. The head model was formed by separating the brain hemispheres and filling them with saline solutions of different concentrations to simulate the normal and oedematous tissue in the brain. Another oedema model is formed by Merwa *et al.* [67]. They used a more realistic model by using segmented data from head images. The oedema was modeled by a sphere position and size of which can be varied. They showed that a large oedema (2 cm in radius) can be detected even at low frequencies (100 kHz).

In medical devices, safety is a major concern and should be investigated. Although the method is new and has no regular standardization, in 1999, Gencer and Tek offered using EIT standards and used the applicable upper limit of injected current inside the body as the constraint [41]. According to that study, induced currents are much below than the safety limits for low frequencies [45]. There is no study, however, on more realistic cases and for multi-frequency experiments. It must be noted that, the radiation in high-

frequency region can induce hazardous currents. Thus, the feasibility of operating at upper frequency bands and sensor configurations should be further investigated for medical purposes.

Up to present time, it was shown that this new (contactless) electrical impedance imaging technique is a promising approach for diagnosing and monitoring purposes. However, there is still limited research on its possible biomedical applications. There is no source of preliminary imaging results of the human in the literature since both the sensitivity of the sensors are still low and the inverse problem solution methods are incapable.

1.4 Motivations and Objectives

Since this is an emerging new imaging modality there are many research opportunities. The specific goals of this thesis study and motivations are listed below.

1. *Developing a numerical solver* This study is focused on developing a numerical solver for the computation of fields in an arbitrary shaped, inhomogeneous body nearby a bioimpedance sensor. It is found that the operating frequency of the sensor should cover 10 kHz to 1 GHz frequency band in order to test general applications and for other uses in future. To obtain solutions at this frequency band, two solvers must be developed: a solver for uncoupled field equations at low operating frequencies and a solver for coupled field equations solver at high operating frequencies.

2. *Electrical properties of tissues* It is desired to develop realistic models for multi-frequency applications. Therefore the 10 kHz to 1 GHz frequency impedance spectra of the tissues must be investigated. By using this data, the quasi-static approximations should be tested for low operating frequencies. Additionally some preliminary proposals for operation frequencies and quasi-static ranges for EII modalities should be discussed.

3. *Realistic Models* One objective of this study is to develop high resolution realistic head models. To use a head model at MR resolution, the sizes

of grids must be $1 \times 1 \times 1$ mm. In addition, more detailed models of pathological cases must be constructed for multi-frequency applications (compared to, for example, the simple oedema model investigated in the previous studies).

4. *Investigation of application areas* The developed solver will be used to test the feasibility of possible applications. It is impossible, for example, to distinguish intracranial hemorrhage and oedema from MRI images, or by using other imaging modalities. Usual procedure in hospitals is taking a second MRI image of the patient after waiting some time and deciding whether the pathological tissue is intracranial hemorrhage or oedema depending on the difference on the MRI image. Since the electrical properties of these pathological tissues are different it will be useful to investigate these two situations by using this adopted measurement approach.

5. *Parallelization* The solver requires large amount of computational resources, both time and memory storage. Therefore an implementation of the solution method should support the parallelization for the future use.

6. *Safety Standardization* There is no safety standardization for this imaging modality. Therefore one objective of this study should be to introduce safety limits for sensor's excitation current (and/or number of turns) for multi-frequency applications.

1.5 Outline

In this Chapter an introduction to EII modalities and a literature survey is given. The major differences of contactless methods versus electrode methods are discussed. The objectives/motivations of this study are explained.

In Chapter 2, the electrical properties of tissues are investigated. The basic phenomenons, responsible for the frequency dependent behavior of tissue

conductivities are mentioned and modeling functions are presented. The quasi-static approximations are investigated. The major stages in realistic head model construction are shown.

In Chapter 3, the electromagnetic formulation for an inhomogeneous, linear, isotropic and arbitrary shaped object is derived from Maxwell's equations. The quasi-static formulation is also derived in parallel.

In Chapter 4 and 5, the solutions for different geometries are presented. Analytical and numerical solutions for simple axisymmetric models and realistic head models are presented. Also distinguishability of intracranial hemorrhage and oedema by using this modality is investigated.

In Chapter 6, the discussions and conclusions are presented.

CHAPTER 2

SELECTION OF MODEL PARAMETERS

In this thesis study, one objective is to develop a numerical solver for the computation of electromagnetic fields near the bioimpedance sensor. In these computations, the electrical properties of the biological tissues must be appropriately modeled in a broad frequency band. Although this study mainly concerns the head models and possible applications for the head, the electrical properties of other body tissues will also be introduced for sake of future use and complementary information.

In this chapter, first, the mechanisms behind the changes in the electrical impedances of biological tissues as a function of operating frequency will be presented. Next, the quasi-static approximation for different tissues and tissue groups will be discussed. The electrical conductivity and permittivity plots will also be introduced to determine the optimum frequency bands for different clinical applications.

2.1 Electrical Properties of Biological Media

The biological tissues have a nonuniform structure causing a varying electrical impedance spectrum for different frequencies. This phenomenon can be explained in terms of polarizations in atomic levels and the reasons for this frequency dependence will be discussed in this section.

2.1.1 Polarization in Biological Media

At the presence of an external electric field, electric dipoles are induced inside the dielectric material. This causes local molecular polarizations in the material. It is assumed that this polarization is linearly proportional to electric field for weak excitations and can be expressed as,

$$\mathbf{P} = \alpha(w)\mathbf{E} \tag{2.1}$$

where $\mathbf{P}$ is the polarization vector, $\mathbf{E}$ is the applied electric field and $\alpha(w) = \epsilon_0(\epsilon_r - 1)$. At low frequencies it is assumed that there is no dielectric loss inside the media resulting in a high permittivity and low static conductivity. However by increasing frequency there will be a lag between the polarization and the electric field variation depending on the size and shape of the media. This will lead to a dielectric loss resulting a decrease in permittivity and increase in conductivity. It is known that these dependency in frequency is not linear and some different phenomenons named as *relaxation mechanisms* are present.

2.1.1.1 Relaxation Mechanisms

The movement of the dipoles and electric charges inside the media due to an applied electric field will cause the relaxation mechanisms. There are three major relaxation types for the biological tissues: dipolar relaxation, Maxwell-Wagner relaxation and Counterion relaxation:

1. *Dipolar Relaxation*: Dipolar relaxation arise in high frequency range. Only at high frequencies the torque of the applied electrical field will be dominant over the thermal forces to align the permanent and induced dipoles. However the thermal forces still interrupt the alignment. The time needed for dipoles to relax will be different depending on the molecular properties of the tissues. Therefore it is strictly dependent upon the molecular shape, size, and structure as well as the temperature.

2. *Maxwell-Wagner Relaxation*: It is dominant at radio frequencies and arises from the heterogeneity of the medium.

3. *Counterion Relaxation*: It is known that this phenomenon is dominant at low frequencies. It occurs from the semipermeable membranes like ionic diffusion channels which arises charge accumulation on the surface.

2.1.1.2 Dielectric Dispersions in Biological Media

As explained previously, in biological media, different relaxation mechanisms are dominant in different frequency bands. A typical representation of this phenomena is shown in Fig 1. These relaxation regions are named as α, β and γ dispersion regions. At low frequencies conductivity is nearly static and very low. On the contrary permittivity is high at low frequencies and decreasing with the increase of frequency.

In α dispersion region, the ionic diffusion is not very fast causing an increase in the capacitance of the membrane which means a high permittivity due to counterion relaxation. This means the charges will only travel across the extracellular medium because of the lack of ionic diffusion. Therefore at α dispersion region, the measured electric field is not relevant with the intracellular medium.

In β dispersion region the membrane capacitance is not as high as in α dispersion region. Therefore the cell behaves like a heterogenous medium and Maxwell-Wagner relaxation effects are present. Some leakage currents starts to pass across the intracellular medium as well as the extracellular medium causing an increase in conductivity and also decrease in permittivity because of reduction in charging.

In γ dispersion region the membrane capacitance will be zero and water molecules will be polarized due to counterion relaxations. Since most of the biological media has large amounts of water molecules, at γ dispersion region it is very hard to distinguish the electrical properties of the tissues accurately.

Therefore at low frequencies the extracellular content of the tissues are measurable and as frequency increases the information of both the intracellular and extracellular content seems to be measurable practically.

2.1.2 Modeling of Dispersion Regions

By using dielectric measurement data of a frequency band, it is advantageous to form a parametric function that best fits the behavior of electrical properties for that frequency range. This permits to make simulations in different frequencies other than the measured frequencies. In order to model these functions the relaxation mechanisms are explained previously and the parametric functions which will model this frequency behavior of tissues will be discussed in this section.

2.1.2.1 Debye Equation

As a first order approximation to the dielectric behavior, Debye's equation is defined as,

$$\hat{\epsilon}(w) = \epsilon_\infty + \frac{\Delta\epsilon}{1 + jw\tau} \tag{2.2}$$

where $\hat{\epsilon}(w)$ gives the complex permittivity. The magnitude of dispersion is $\Delta\epsilon = \epsilon_s - \epsilon_\infty$. ϵ_∞ is the permittivity at high frequencies where $w\tau \gg 1$, ϵ_s is the permittivity at low frequencies where $w\tau \ll 1$ and ϵ_0 is the permittivity of free space. τ is a time constant which states the polarization mechanism for different relaxation regions. In dipolar relaxation region it is estimated by,

$$\tau = \frac{4\pi\eta a^3}{kT} \tag{2.3}$$

where T is the temperature, η is the viscosity of the medium and k is the Boltzmann's constant. In Maxwell-Wagner dispersion region τ is dependent on the electrical properties of the heterogenous object. Since counterion relaxation is a more complicated process, modeling of this phenomena is not accurately known. However τ is assumed to behave like,

$$\tau = \frac{L^2}{D} \tag{2.4}$$

where D is a diffusion constant and L is the length of the diffusion path.

However Debye model is used to model the dielectric dispersions. Therefore a modified term can be added to model the static conductivity as,

$$\hat{\epsilon}(w) = \epsilon_\infty + \frac{\sigma_s}{jw\epsilon_0} + \frac{\Delta\epsilon}{1 + jw\tau} \tag{2.5}$$

Since each polarized molecule can have different time constants, therefore a more broadening modeling of tissues can be made by superposition of frequency responses as given,

$$\hat{\epsilon}(w) = \epsilon_\infty + \frac{\sigma_s}{jw\epsilon_0} + \sum_{n=1}^{m} \frac{\Delta\epsilon_n}{1 + jw\tau_n} \tag{2.6}$$

2.1.2.2 Cole-Cole Equation

Cole-Cole equation is a modified version of the Debye's equation as,

$$\hat{\epsilon}(w) = \epsilon_\infty + \frac{\sigma_s}{jw\epsilon_0} + \sum_{n=1}^{m} \frac{\Delta\epsilon_n}{1 + (jw\tau_n)^{(1-\alpha_n)}} \tag{2.7}$$

where the added term α represents the broadening of dispersion for different tissue types.

2.2 Investigation of Distinguishability

To distinguish tissues from each other by using this imaging modality, their electrical properties should be different. Since the electrical properties of tissues strictly dependent upon the operating frequency as explained, this parameter can be optimized in order to increase the sensitivity of the sensor. Therefore operating frequencies for possible different clinical applications can be investigated by using the contrast information between the electrical properties of the body tissues.

It should be mentioned that the organs can not be thought independently from each other since their position inside the body do not change. Therefore, for convenience, the body is divided into three regions: head (white and grey brain matter, CSF, cerebellum, blood), torso (heart, breast fat, deflated and inflated lungs) and abdomen (stomach, liver, spleen, kidney, blood). In Figure 2.1-2.3 show the relative changes in the electrical properties (that is, $(\sigma_1 - \sigma_2)(f)$, $(\epsilon_1 - \epsilon_2)(f)$) of selected tissues in the 10 kHz-1 GHz frequency range.

Some important inferences obtained from these plots are given below. For head applications,

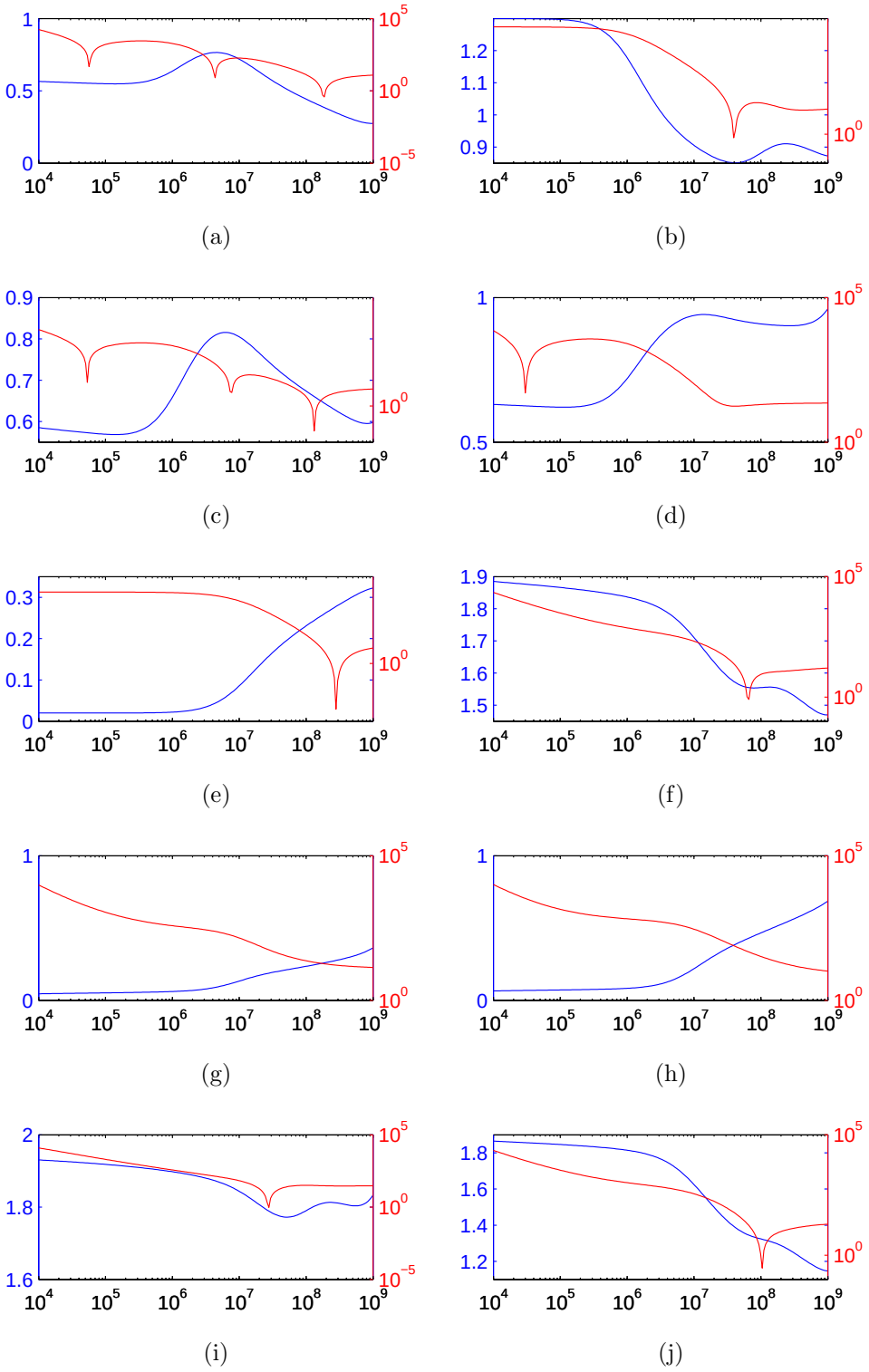

Figure 2.1: Relative changes in the electrical properties (conductivity (blue), permittivity (red)) of selected *head* tissues in the 10 kHz-1 GHz frequency range (a) blood-cerebellum, (b) blood-CSF, (c) blood-gray matter, (d) blood-white matter, (e) gray matter-cerebellum, (f) gray matter-CSF, (g) gray matter- white matter, (h) white matter-cerebellum, (i) white matter-CSF, (j) cerebellum-CSF. The permittivity difference between the tissues are in logarithmic scale.

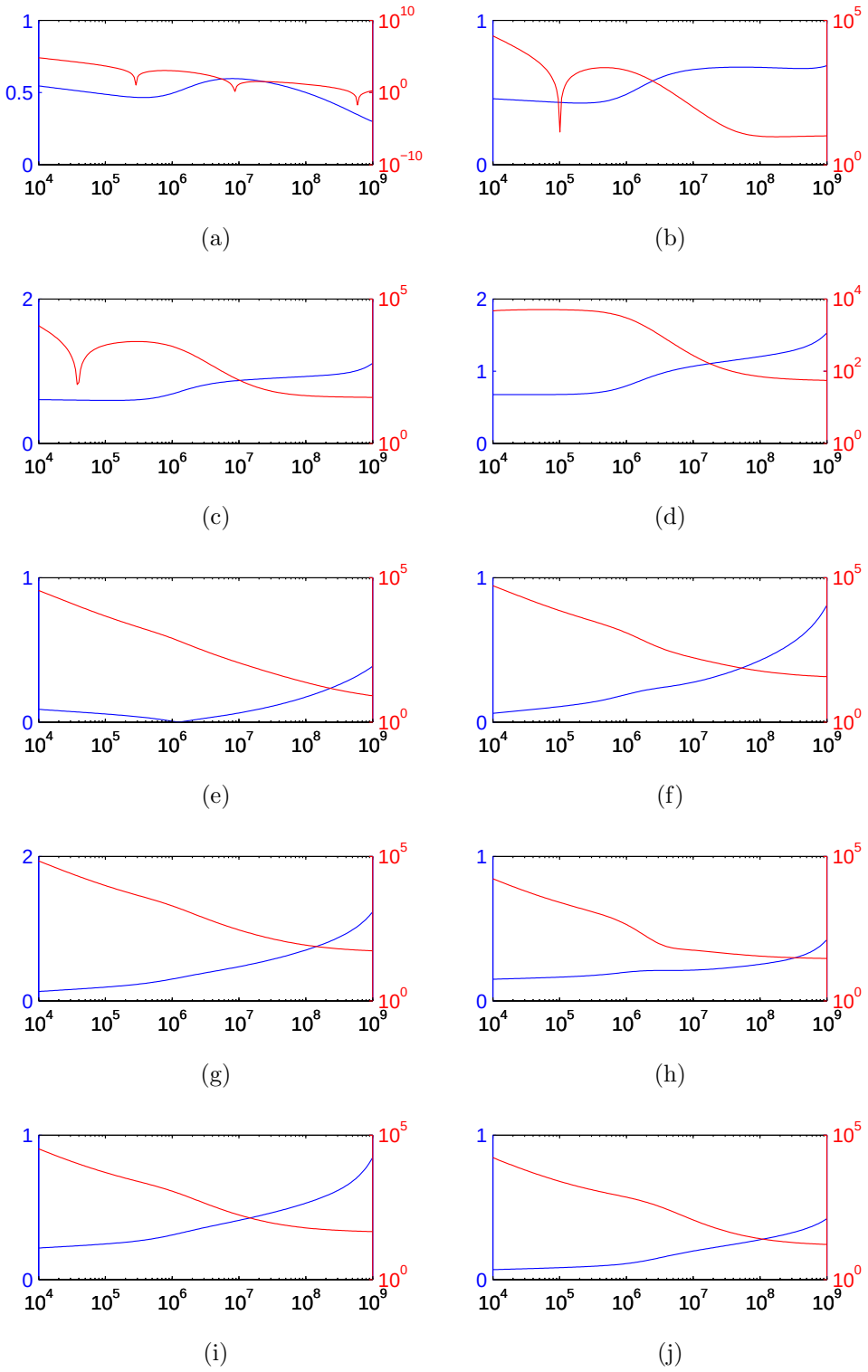

Figure 2.2: Relative changes in the electrical properties (conductivity (blue), permittivity (red)) of selected *torso* tissues in 10 kHz-1 GHz frequency range (a) blood-heart, (b) blood-deflated lung, (c) blood-inflated lung, (d) blood-breast fat, (e) heart-deflated lung, (f) heart-inflated lung, (g) heart- breast fat, (h) deflated lung-inflated lung, (i) deflated lung-breast fat, (j) inflated lung-breast fat. The permittivity difference between the tissues are in logarithmic scale.

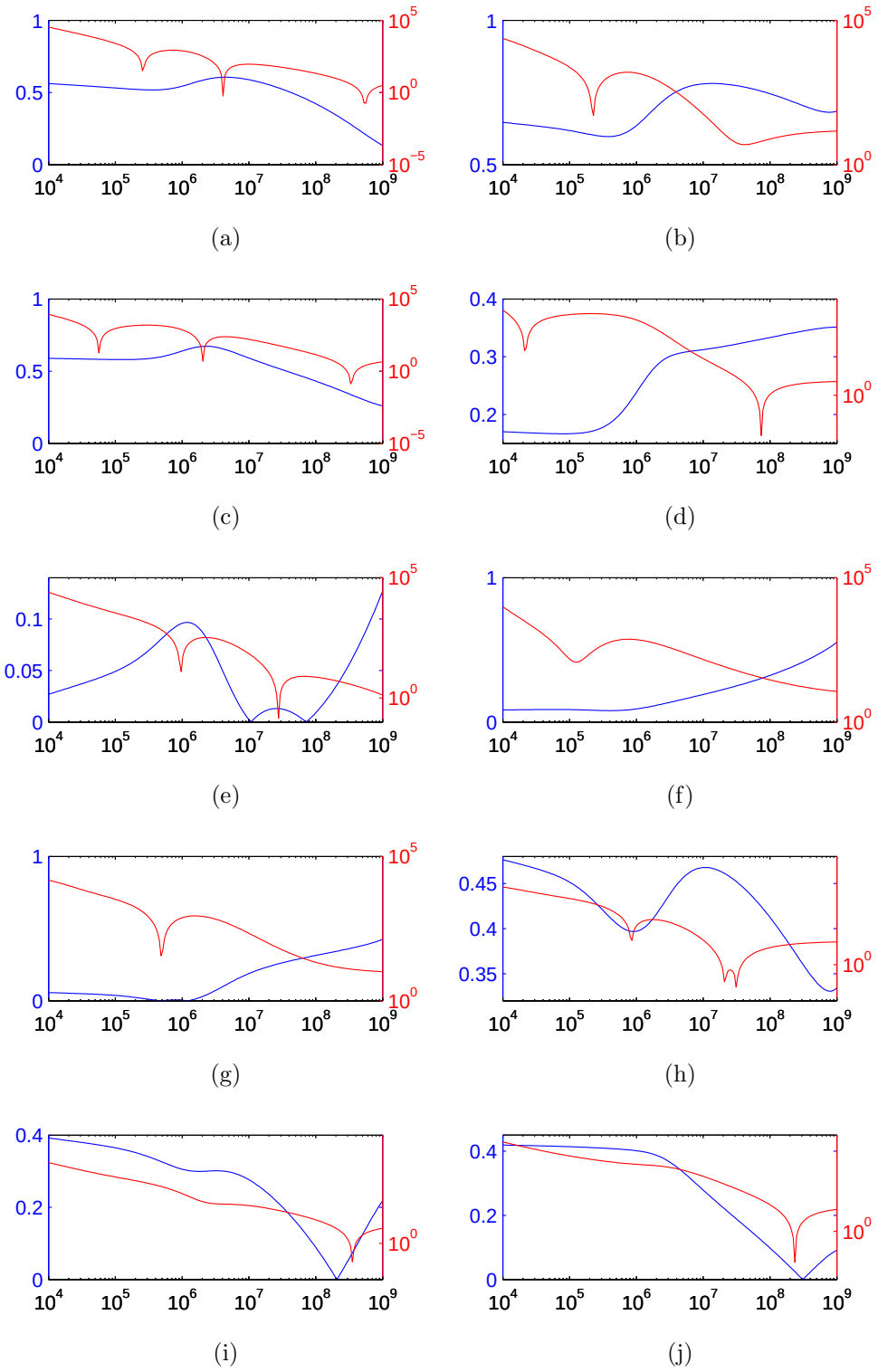

Figure 2.3: Relative changes in the electrical properties (conductivity (blue), permittivity (red)) of selected *abdomen* tissues in 10 kHz-1 GHz frequency range (a) blood-kidney, (b) blood-liver, (c) blood-spleen, (d) blood-stomach, (e) kidney-spleen, (f) liver-kidney, (g) liver-spleen, (h) liver-stomach, (i) stomach-kidney, (j) stomach-spleen. The permittivity difference between the tissues are in logarithmic scale.

- Contrast of soft tissue conductivities of the head (Gray matter, white matter and cerebellum) is prominent for the frequencies higher than 2 MHz. Therefore high frequency operations should be used to distinguish these tissues.

- Although CSF conductivity is nearly independent of the frequency, low operating frequencies are best to differentiate this tissue, since conductivity of other tissues increases with frequency.

- Electrical conductivity of CSF tissue is very high compared to other tissues. Thus it should not be neglected in the forward problem models for electrical impedance imaging, in general.

- Diagnosing the intracranial hemorrhage inside the head seems possible and best detected at 1-10 MHz range.

For torso applications,

- Monitoring the respiration system can be achieved and frequency do not play a significant role in this application.

- Since the blood and heart conductivity differs, monitoring the circulation system also seems feasible.

- For hemorrhage inside torso tissues, it is best to choose 10 MHz as the operating frequency.

For abdomen applications,

- Hemorrhage inside stomach tissue can be best sensed above 500 kHz.

- Kidney and spleen are undistinguishable between 10 MHz and 100 MHz and best distinguished at 1 MHz.

- To distinguish the stomach lower operating frequencies should be chosen. The lower the frequency (less than 1 MHz) the better the distinguishability performance.

- Liver and kidney are best distinguished at high frequencies.

2.3 Investigation of Quasi-Static Approximations

It is essential to investigate the quasi-static approximations for a range of frequencies used in EII. Under quasi-static conditions, the formulations are considerably simplified and the required computational resources are quite low. To investigate the validity of these approximations, the medium is assumed unbounded and homogenous in conductivity. If the excitation current is sinusoidally time varying, the electromagnetic fields can be represented by means of the two potentials, namely, the magnetic vector potential $\mathbf{A}$ and scalar potential ϕ. The electric field $\mathbf{E}$ and magnetic flux density $\mathbf{B}$ can be expressed in terms of these potentials as follows:

$$\mathbf{E} = -\nabla\phi - jw\mathbf{A} \tag{2.8}$$

$$\mathbf{B} = \nabla \times \mathbf{A} \tag{2.9}$$

The solution of these fields can be obtained by solving the following equations,

$$\nabla^2\phi - \gamma^2\phi = -\frac{\rho_s}{\epsilon} \tag{2.10}$$

$$\nabla^2\mathbf{A} - \gamma^2\mathbf{A} = -\mu\mathbf{J}_s \tag{2.11}$$

where ρ_s is the source charge density, $\mathbf{J}_s$ is the source current density. The propagation constant is,

$$\gamma = \alpha + j\beta = \sqrt{-jw\mu(\sigma + jw\epsilon)} \tag{2.12}$$

where α and β are the attenuation (Np/m) and phase (rad/m) constants, respectively. The analogy between the among the above equations can easily be seen ($\rho_s \leftrightarrow \mathbf{J}_s$, $\phi \leftrightarrow \mathbf{A}$, $\mu \leftrightarrow \frac{1}{\epsilon}$). The solution of the potentials are given by [2],

$$\phi = \frac{1}{4\pi(\sigma + jw\epsilon)} \int_V \frac{I_s e^{\gamma R}}{R} dV \tag{2.13}$$

$$\mathbf{A} = \frac{\mu}{4\pi} \int_V \frac{\mathbf{J}_s e^{\gamma R}}{R} dV \tag{2.14}$$

where R is the distance of the source to the field point.

Table 2.1: The maximum operating frequencies which the displacement currents are assumed to be negligible at 1 kHz and 1 GHz frequency band.

Tissue	**Frequency (kHz)**
CSF	6×10^5
Gray Matter	1.7
White matter	10
Cerebellum	30
Fat	1.7×10^3
Muscle	72
Skin	–
Skull	180
Inflated Lung	1
Deflated Lung	81
Heart	280
Breast Fat	4×10^3
Stomach	500
Kidney	–
Spleen	29
Liver	–

* – means that the displacement currents can not be neglected.

2.3.1 Capacitive Effects

For sinusoidal excitations, the electrical properties of biological tissues can be expressed as follows:

$$\sigma + jw\epsilon = \sigma(1 + j\frac{w\epsilon}{\sigma}) \tag{2.15}$$

The imaginary part of above equation can be neglected when $\frac{w\epsilon}{\sigma} << 1$. The changes in the displacement to conduction current ratio $\frac{w\epsilon}{\sigma}$ are presented for various tissue groups in Figure 2.8.(c) 2.9.(c) and 2.10.(c). If the ratio $\frac{w\epsilon}{\sigma}$ is less than 0.1, it is defined that the capacitive effects can be neglected. Therefore the maximum operating frequencies which the displacement currents are assumed to be negligible are listed in Table 2.1.

Since the main concern in this thesis study is to model the head, capacitive effects of the head tissues are highlighted in Table 2.2. It is noted that even for 100 kHz the percent ratio ($100 \times \frac{w\epsilon}{\sigma}$) is around $10 - 15\%$ and at 1 MHz

Table 2.2: The capacitive effects (%) at head tissues for different frequencies.

	10 kHz	**100 kHz**	**1 MHz**	**10 MHz**	**100 MHz**
CSF	0.00	0.03	0.30	3.02	23.39
Gray Matter	10.77	13.41	29.31	60.96	79.69
White matter	9.98	14.33	26.11	61.70	97.52
Fat	1.18	16.3	6.42	31.28	103.29
Muscle	4.23	12.44	20.32	15.40	51.87
Skin	637.50	130.56	46.14	33.75	70.20
Skull	1.42	6.09	33.01	47.77	132.20

it increases to $20-30\%$. This means that ignoring the displacement currents may cause considerable error in the numerical results.

2.3.2 Inductive Effects

The induced currents will also contribute to the time-varying magnetic field inside the body. However, the secondary magnetic field, $-jw\mathbf{A}$ at the right hand side of the electric field equation, (Equation 2.8) can be neglected, if $\nabla\phi >> |w\mathbf{A}|$. This condition is established when $(kR)^2 << 1$. In such a case, the electrical field caused the by the gradient of the scalar potential dominates the electric fields caused by magnetic induction. Considering a maximum distance of $R = 10cm$, the inductive effects $|(kR)^2|$ are calculated for different head tissues and operating frequencies (Table 2.3). As can be seen from Table 2.3, the error at the soft tissues are less than 2% even at 10 cm distance from the excitation source. Also the inductive effects for body tissues other than head tissues are given in Figure 2.8.(f), Figure 2.9.(f) and Figure 2.8.(f).

2.3.3 Propagation Effects

The propagation constant can be decomposed into real and imaginary components where α is the attenuation constant and β is the phase constant,

$$\alpha = \omega\sqrt{\frac{\mu\varepsilon}{2}\left(\sqrt{1+(\frac{\sigma}{\omega\epsilon})^2}-1\right)} \tag{2.16}$$

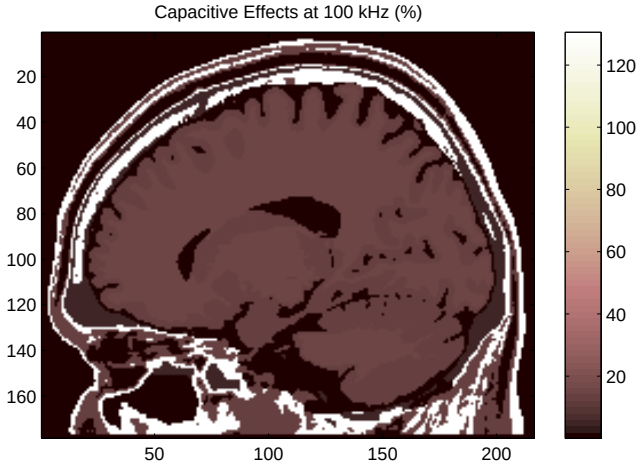

(a)

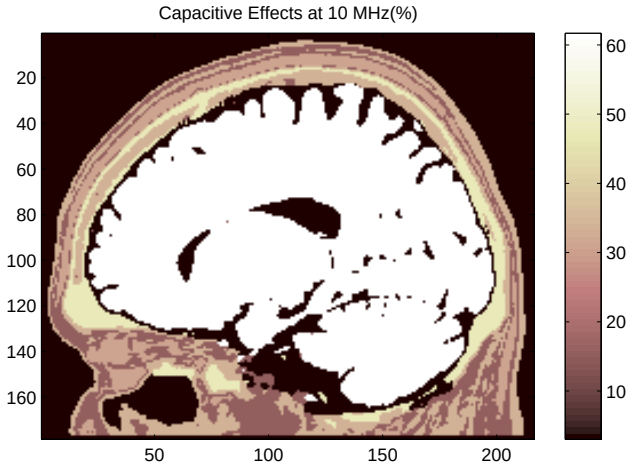

(b)

Figure 2.4: Capacitive effects (%) at head (a) 100 kHz, (b) 10 MHz.

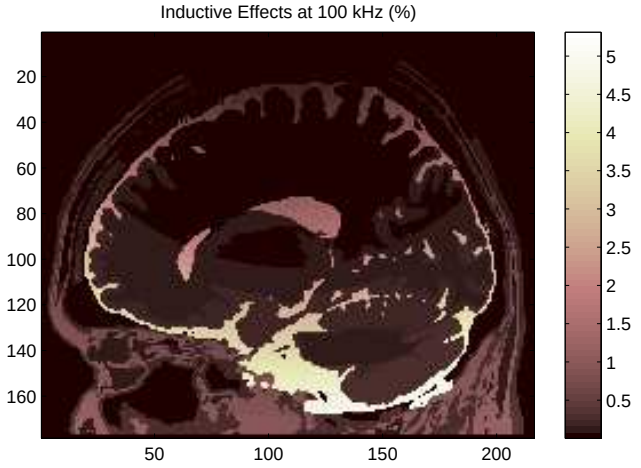

(a)

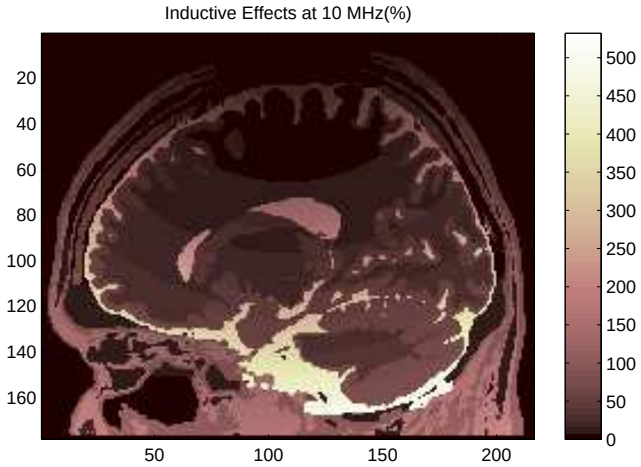

(b)

Figure 2.5: Inductive effects (%) at head (a) 100 kHz, (b) 10 MHz.

Table 2.3: The inductive effects (%) at head tissues for different frequencies at 10 cm away from the excitation.

	10 kHz	**100 kHz**	**1 MHz**	**10 MHz**	**100 MHz**
CSF	0.15	1.58	15.79	158.16	1714.45
Gray Matter	0.01	0.11	1.34	26.97	564.85
White matter	0.00	0.06	0.83	14.70	357.85
Fat	0.00	0.03	0.35	4.35	77.66
Muscle	0.03	0.28	4.05	49.27	629.38
Skin	0.00	0.85	1.92	30.46	504.34
Skull	0.00	0.01	0.20	3.74	84.17

$$\beta = \omega\sqrt{\frac{\mu\varepsilon}{2}\left(\sqrt{1+(\frac{\sigma}{\omega\epsilon})^2}+1\right)} \tag{2.17}$$

Therefore propagation term in in 2.16 and 2.17 can be decomposed into two components as $e^{\gamma R} = e^{\alpha R}e^{j\beta R}$. The exponential functions can be written in terms of infinite serie sums as,

$$e^{\alpha R} = 1 + \alpha R + \frac{(\alpha R)^2}{2!} + \frac{(\alpha R)^3}{3!} + \cdots \tag{2.18}$$

$$e^{j\beta R} = 1 + j\beta R - \frac{(\beta R)^2}{2!} + j\frac{(\beta R)^3}{3!} - \cdots \tag{2.19}$$

The attenuation term can be neglected when $\alpha R << 1$ and phase delays can be neglected when $\beta R << 1$.

Skin depth δ is defined as the distance through which the amplitude of a traveling plane wave decreases by a factor e^{-1} and expressed in terms of the attenuation constant as,

$$\delta = \frac{1}{\alpha} = \frac{1}{\omega\sqrt{\frac{\mu\varepsilon}{2}\left(\sqrt{1+(\frac{\sigma}{\omega\epsilon})^2}-1\right)}} \tag{2.20}$$

and when $\frac{w\epsilon}{\sigma} << 1$ the skin depth reduces to,

$$\delta = \sqrt{\frac{2}{\sigma\mu w}} \tag{2.21}$$

The attenuation effects are tested by evaluating $1 - |e^{\alpha R}|$ for different tissues and presented in Figure 2.8.d 2.9.d and 2.8.d. The propagation delays are tested by evaluating $|\angle e^{j\beta R}|$ and the results are plotted in Figure 2.8.(e), Figure 2.9.(e) and Figure 2.8.(e).

Table 2.4: The attenuations errors (%) of head tissues for different frequencies at a 10 cm distance from the excitation coil.

	10 kHz	**100 kHz**	**1 MHz**	**10 MHz**	**100 MHz**
CSF	2.77	8.5	24.46	58.35	92.37
Gray Matter	0.64	2.13	6.71	22.45	64.36
White matter	0.50	1.66	5.43	17.04	52.02
Fat	0.41	1.29	3.96	11.62	28.15
Muscle	1.13	3.49	11.96	31.68	72.83
Skin	0.00	0.93	7.20	27.52	64.51
Skull	0.28	0.87	2.60	9.81	25.32

Table 2.5: The propagation delays (°) of head tissues for different frequencies at a 10 cm distance from the excitation coil.

	10 kHz	**100 kHz**	**1 MHz**	**10 MHz**	**100 MHz**
CSF	1.61	5.09	16.12	51.71	174.12
Gray Matter	0.40	1.40	5.31	25.94	122.67
White matter	0.31	1.10	4.14	19.18	99.80
Fat	0.23	0.75	2.46	9.63	46.80
Muscle	0.67	2.30	8.92	30.52	122.83
Skin	0.20	1.58	6.69	25.69	114.16
Skull	0.16	0.53	2.08	9.38	49.83

Starting from 1 MHz the propagation effects gradually increases. In practice, the depth sensitivity of the sensor is nearly twice the coil radius. Thus, for a coil of 1 cm radius, the attenuation errors and propagation delays are tested at a 2 cm distance. For an operation frequency of 10 MHz, the attenuation error and phase delay are found as $2-5\%$ and $2-5°$, respectively.

2.4 Head Model Construction

Generally, both MRI and CT images are used to obtain realistic head models by applying different segmentation algorithms. In this thesis study, a simulated MRI data [43] is used in the head model construction . The model includes 7 different types of tissues: cerebrospinal fluid (CSF), grey matter, white matter, fat, muscle, muscle/skin, skull. The electrical conductivity and permittivity

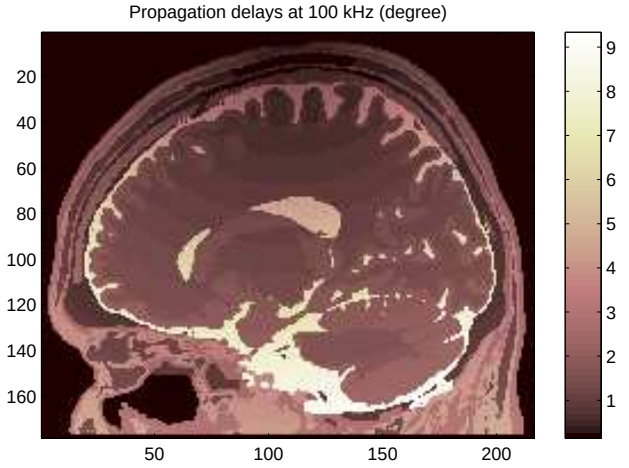

(a)

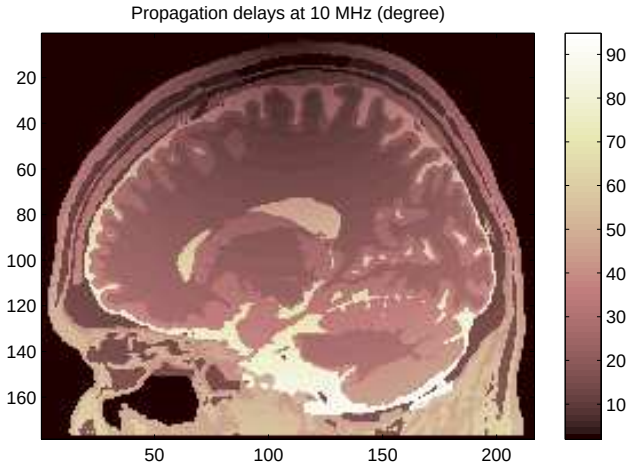

(b)

Figure 2.6: Phase delay effects (°) at head (a) 100 kHz, (b) 10 MHz.

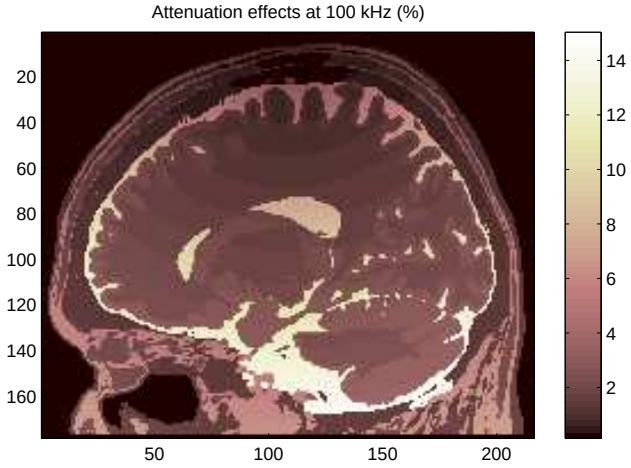

(a)

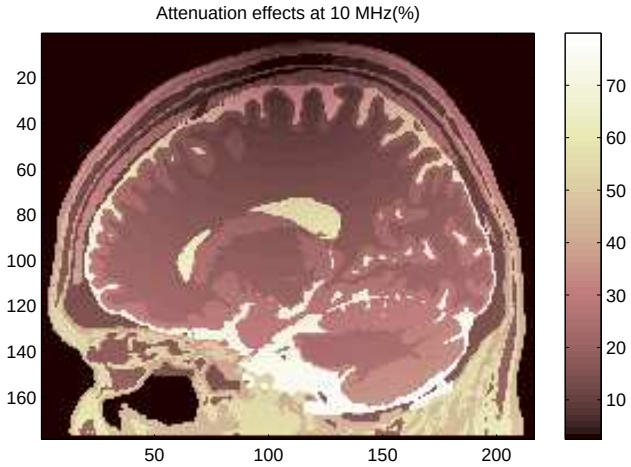

(b)

Figure 2.7: Attenuation effects at head (a) 100 kHz, (b) 10 MHz.

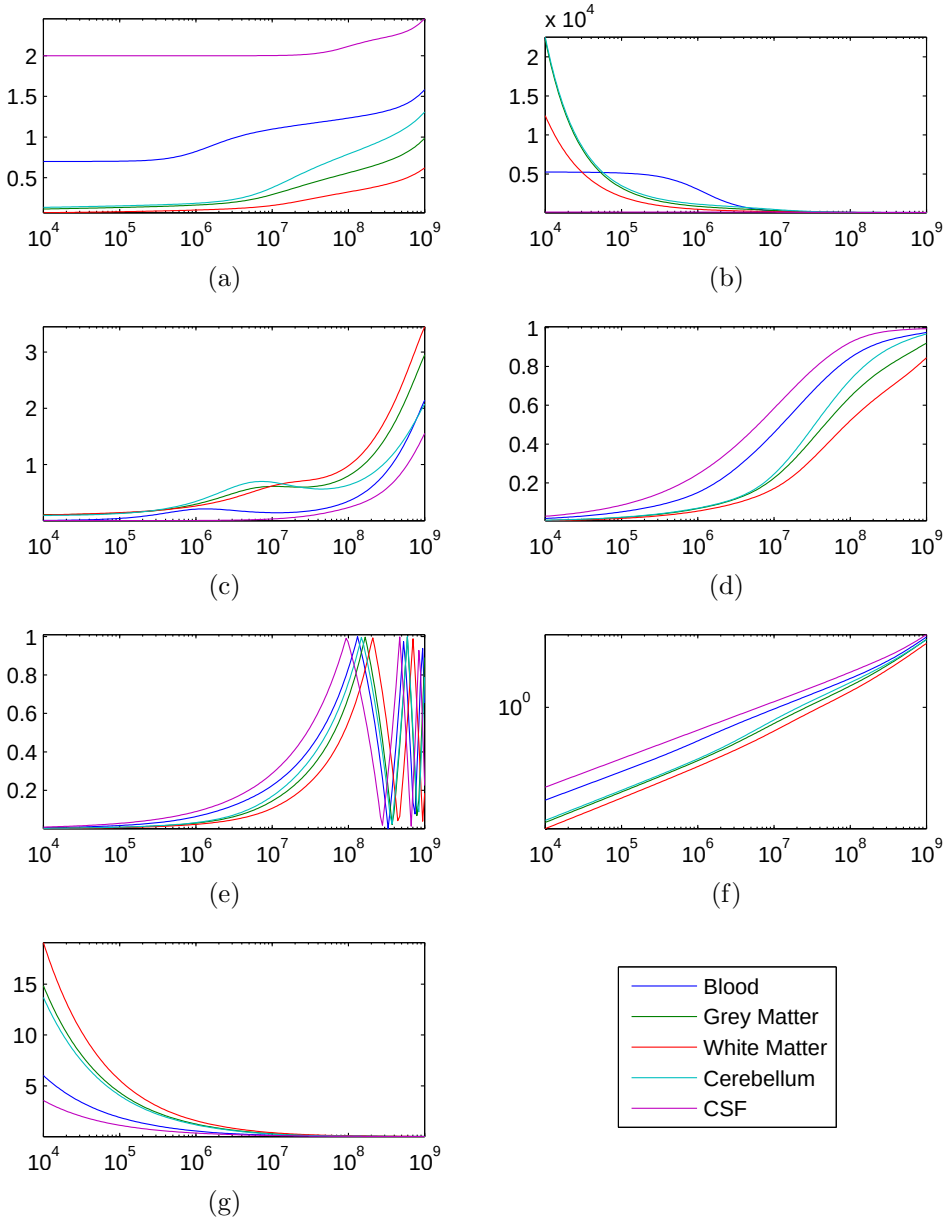

Figure 2.8: Electrical properties of *head* tissues in 10 kHz-1 GHz frequency range and investigation of quasi-static conditions (a) electrical conductivity, (b) electrical permittivity, (c) capacitive effects, (d) attenuation effects, (e) phase delaying effects, (f) inductive effects, (g) skin depth.

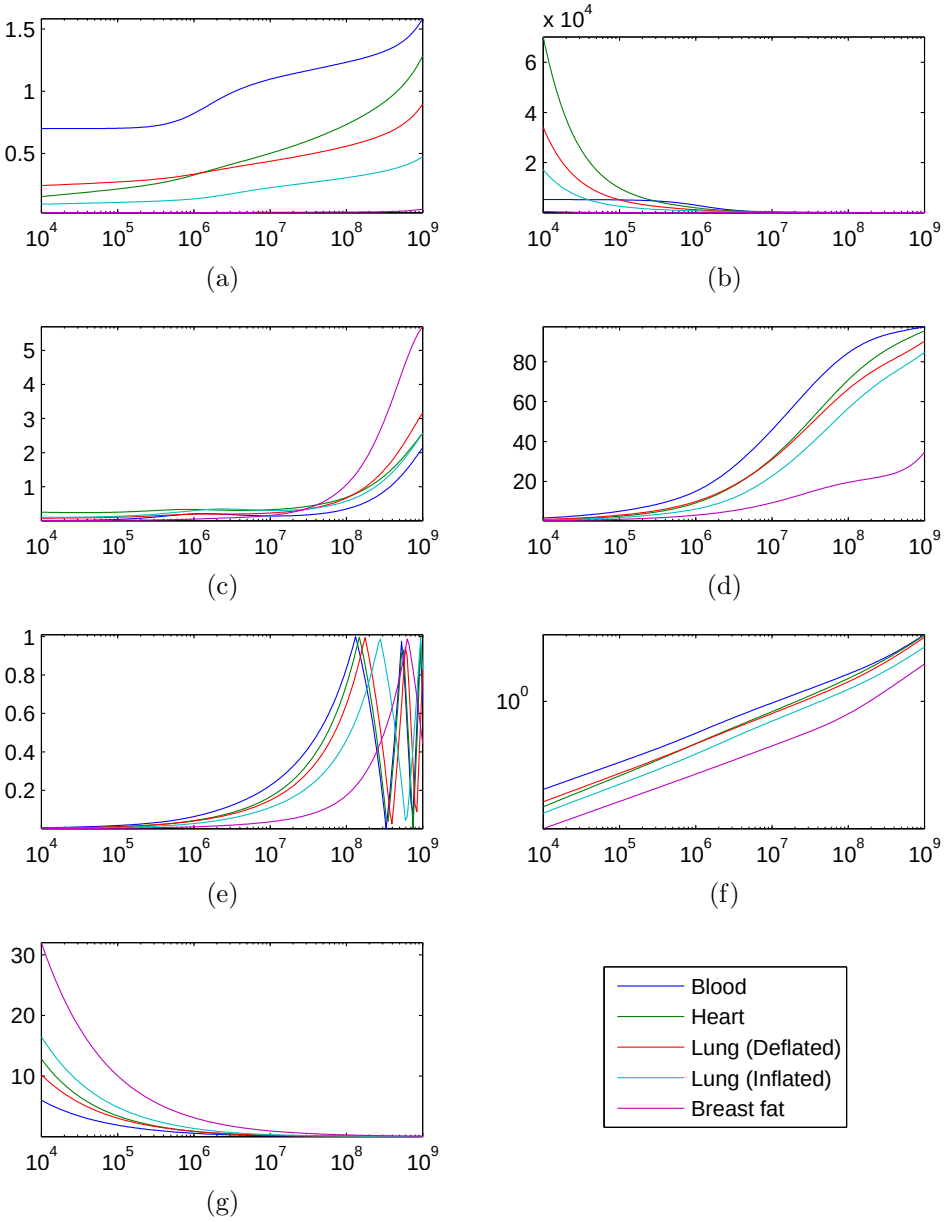

Figure 2.9: Electrical properties of *torso* tissues in 10 kHz-1 GHz frequency range and investigation of quasi-static conditions (a) electrical conductivity, (b) electrical permittivity, (c) capacitive effects, (d) attenuation effects, (e) phase delaying effects, (f) inductive effects, (g) skin depth

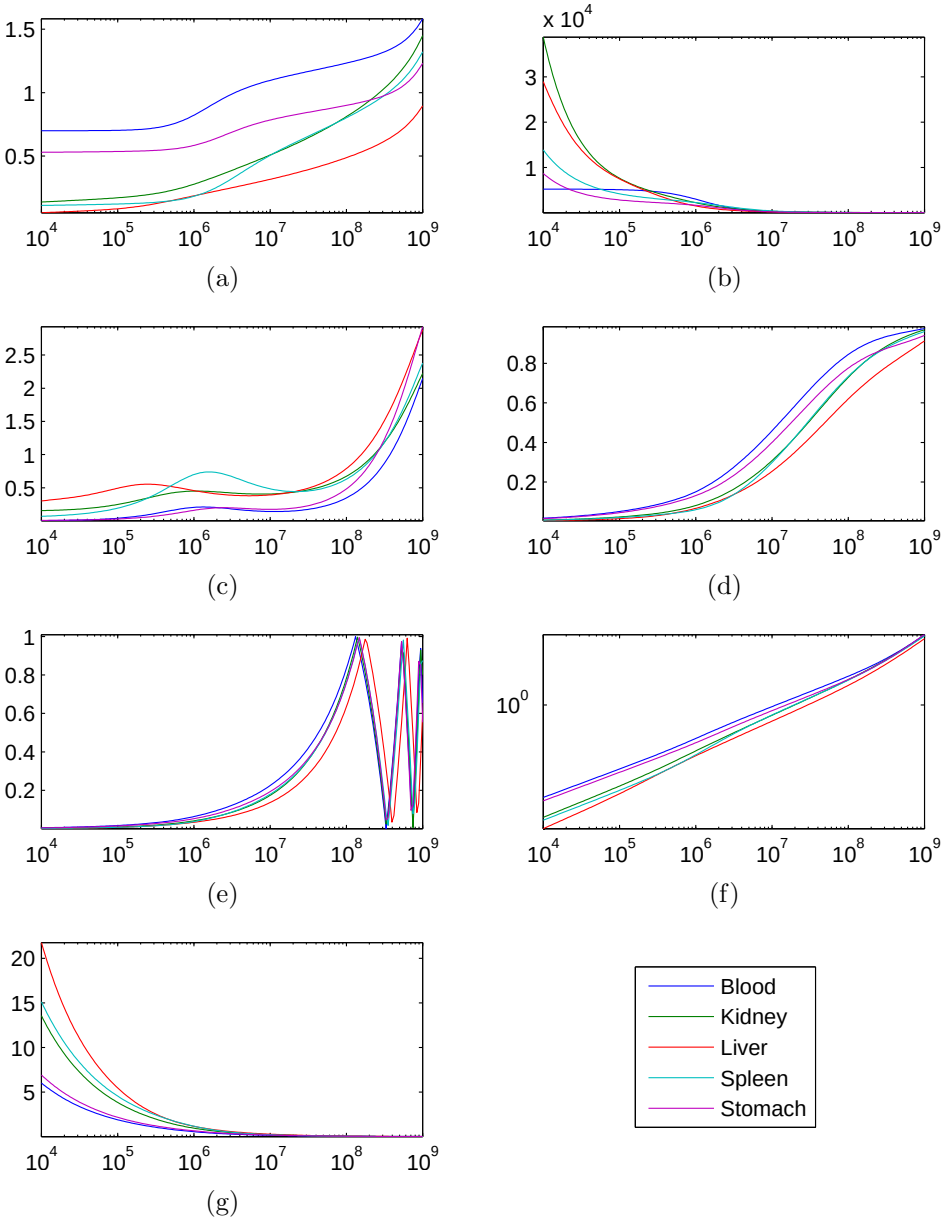

Figure 2.10: Electrical properties of *abdomen* tissues in 10 kHz-1 GHz frequency range and investigation of quasi-static conditions (a) electrical conductivity, (b) electrical permittivity, (c) capacitive effects, (d) attenuation effects, (e) phase delaying effects, (f) inductive effects, (g) skin depth

Table 2.6: The electrical properties of the head tissues at 50 kHz and 10 MHz.

	50 kHz		**10 MHz**	
	$\sigma(S/m)$	$\epsilon_r(F/m)$	$\sigma(S/m)$	$\epsilon_r(F/m)$
CSF	2.0000	109	2.0022	108.6
Gray Matter	0.1275	5461	0.2917	319.7
White matter	0.0776	3548	0.1585	175.7
Fat	0.0433	163	0.0526	29.6
Muscle	0.3518	10094	0.6168	170.7
Skin	0.0290	21876	0.3656	221.8
Skull	0.0206	264	0.0428	36.8

Table 2.7: The electrical properties of tissues for 100 MHz and 500 MHz.

	100 MHz		**500 MHz**	
	$\sigma(S/m)$	$\epsilon_r(F/m)$	$\sigma(S/m)$	$\epsilon_r(F/m)$
CSF	2.1140	88.9	2.2780	70.1
Gray Matter	0.5595	80.1	0.7791	55.8
White matter	0.3240	56.8	0.4739	41.0
Fat	0.0299	5.7	0.0368	5.5
Muscle	0.7076	66.0	0.8225	56.5
Skin	0.5228	66.0	0.7041	48.6
Skull	0.0643	15.3	0.1005	12.9

values of the tissues at a prescribed operating frequency are obtained by using a parametric function [33] as explained at the previous section,

$$\hat{\epsilon}(w) = \epsilon_\infty + \frac{\sigma_s}{jw\epsilon_0} + \sum_{n=1}^{4} \frac{\Delta\epsilon_n}{1 + (jw\tau_n)^{(1-\alpha_n)}} \tag{2.22}$$

The parametric function has 14 parameters and is valid at a frequency range of 10 Hz - 20 GHz. The electrical properties of the head tissues for different frequencies are listed in Table 2.6-2.7. Figure 2.11 ((a) and (b)) shows the conductivity and permitivity images of a selected slice formed using the calculated model parameters at 50 kHz. The 3D realistic head model is presented in Figure 2.12.

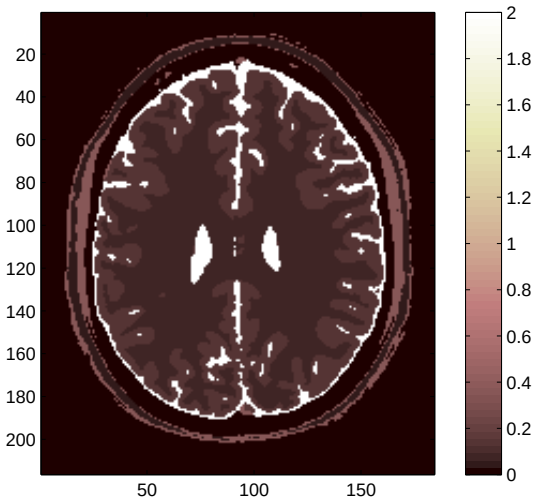

(a)

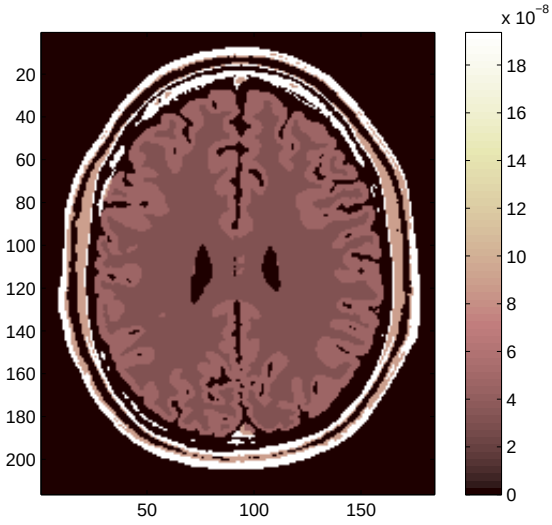

(b)

Figure 2.11: Electrical properties of the realistic head phantom at 50 kHz operating frequency. (a) conductivity (S/m) map (b) relative permitivity (F/m) map.

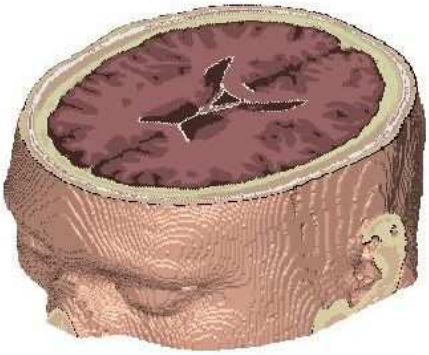

(a)

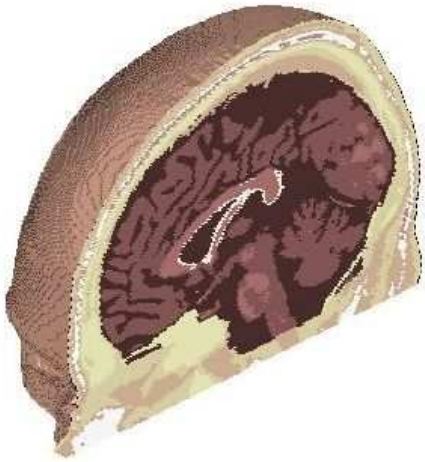

(b)

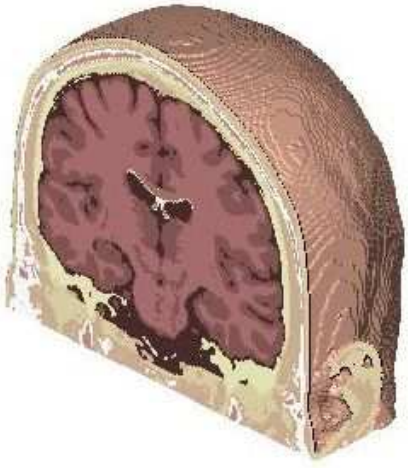

(c)

Figure 2.12: Simulated head model. (a) z slice, (b) y slice, (c) x slice

CHAPTER 3

FORMULATION OF THE FORWARD PROBLEM

3.1 Problem Definition

The measurements of this imaging system are the time-varying magnetic fields detected from the body surface. Thus the *forward problem* is defined as finding the secondary electromagnetic fields caused by the induced currents inside the body (Ω_C in Figure A.1) given the electrical properties of the body and the coil configuration. The primary sources, in this thesis study, are circular coils.

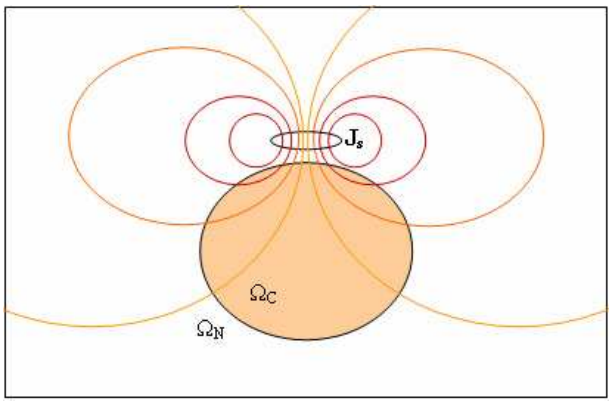

Figure 3.1: The solution domain. Ω_C: Conducting region, Ω_N: Nonconducting region, $\mathbf{J}_s$: Source current density.

3.2 Computation of Electromagnetic Fields

3.2.1 Maxwell's Equations

The behavior of electromagnetic fields in space are described by Maxwell's equations [1]. Since, in this study, the time variation is assumed to be sinusoidal (e^{jwt} time dependence is assumed), phasor notation will be more appropriate to cope with these equations. Maxwell's equations for a linear and isotropic medium and can be written as follows,

$$\nabla \times \mathbf{E} = -jw\mathbf{B} \tag{3.1}$$

$$\nabla \times \mathbf{H} = jw\mathbf{D} + \mathbf{J} \tag{3.2}$$

$$\nabla \cdot \mathbf{D} = \rho \tag{3.3}$$

$$\nabla \cdot \mathbf{B} = 0 \tag{3.4}$$

$$\nabla \cdot \mathbf{J} = -jw\rho \tag{3.5}$$

with the constitutive relations which defines the material properties,

$$\mathbf{B} = \mu\mathbf{H} \tag{3.6}$$

$$\mathbf{D} = \epsilon\mathbf{E} \tag{3.7}$$

$$\mathbf{J} = \sigma\mathbf{E} \tag{3.8}$$

where **E**, **H**, **B**, **D**, **J** are the electric field, magnetic field, magnetic field density, electric field density and current density, respectively. The material properties μ, σ, and ϵ, are the permeability, conductivity and permittivity values of the medium.

3.2.2 E-B Formulation

By using appropriate relations, the equations 3.1 and 3.2 is written by using the fields **E** and **B** as,

$$\nabla \times \mathbf{E} = -jw\mathbf{B} \tag{3.9}$$

$$\nabla \times \mathbf{B} = \mu(\sigma + jw\epsilon)\mathbf{E} + \mu\mathbf{J}_s \tag{3.10}$$

where $\mathbf{J}_s$ is the source current density. $(\sigma + jw\epsilon)\mathbf{E}$ corresponds to the induced currents in the medium. In cartesian coordinate system, these equations are equivalent to the following six coupled, scalar, first-order differential equations,

$$\frac{\partial E_z}{\partial y} - \frac{\partial E_y}{\partial z} = -jwB_x \tag{3.11}$$

$$\frac{\partial E_z}{\partial x} - \frac{\partial E_x}{\partial z} = -jwB_y \tag{3.12}$$

$$\frac{\partial E_y}{\partial x} - \frac{\partial E_x}{\partial y} = -jwB_z \tag{3.13}$$

$$\frac{\partial B_z}{\partial y} - \frac{\partial B_y}{\partial z} = \mu(\sigma + jw\epsilon)E_x + \mu J_x \tag{3.14}$$

$$\frac{\partial B_z}{\partial x} - \frac{\partial B_x}{\partial z} = \mu(\sigma + jw\epsilon)E_y + \mu J_y \tag{3.15}$$

$$\frac{\partial B_y}{\partial x} - \frac{\partial B_x}{\partial y} = \mu(\sigma + jw\epsilon)E_z + \mu J_z \tag{3.16}$$

The representation of these equations in other coordinate systems are straightforward.

3.2.3 A-ϕ Formulation

The curl equations 3.9 and 3.10 are sufficient to find the solutions, once $\mathbf{J}_s$ is specified. However, solving directly $\mathbf{E}$ and $\mathbf{B}$ in the solution space is computationally expensive as six unknowns (three components for each field) must be solved at each point. An alternative approach can be used by defining $\mathbf{E}$ and $\mathbf{B}$ fields in terms of an auxiliary functions.

Since the $\mathbf{B}$ field is always divergence free (3.4) it can be defined in terms of another vector field (the magnetic vector potential $\mathbf{A}$),

$$\mathbf{B} = \nabla \times \mathbf{A} \tag{3.17}$$

Substituting 3.17 into 3.9, a curl free field is obtained ($\nabla \times (\mathbf{E} + jw\mathbf{A}) = 0$). Such a field can be defined in terms of a gradient of a scalar function (ϕ). Thus, $\mathbf{E}$ can be expressed as,

$$\mathbf{E} = -\nabla\phi - jw\mathbf{A} \tag{3.18}$$

$\mathbf{E}$ and $\mathbf{H}$ can be easily calculated if ϕ and $\mathbf{A}$ are computed. There is one point to mention, however, that ϕ and $\mathbf{A}$ are not unique fields. By using a

scalar function ψ, infinitely many $\mathbf{A}$ and ϕ fields can be generated in the form $\mathbf{A} + \nabla\psi$ and $\phi - jw\psi$ without affecting the $\mathbf{E}$ and $\mathbf{H}$ fields.

To express equations 3.9 and 3.10 in terms of ϕ and $\mathbf{A}$, one may chose $\nabla \cdot (\mathbf{A} + \nabla\psi) = 0$ and $\nabla^2\psi = 0$ (Coulomb's gauge) and obtain the following equations,

$$\nabla \cdot ((\sigma + jw\epsilon)\nabla\phi) = -jw\mathbf{A} \cdot \nabla(\sigma + jw\epsilon) \tag{3.19}$$

$$\nabla^2\mathbf{A} = -\mu(\sigma + jw\epsilon)(-\nabla\phi - jw\mathbf{A}) - \mu\mathbf{J}_s \tag{3.20}$$

In cartesian coordinates, the above equations can be written in terms of 4 coupled, scalar, second-order differential functions as,

$$\frac{d(\sigma + jw\epsilon)}{dx}\frac{d\phi}{dx} + (\sigma + jw\epsilon)\frac{d^2\phi}{dx^2} + ... = -jwA_x\frac{d(\sigma + jw\epsilon)}{dx} - ... \tag{3.21}$$

$$\frac{d^2A_x}{dx^2} + \frac{d^2A_y}{dy^2} + \frac{d^2A_z}{dz^2} = -\mu(\sigma + jw\epsilon)(-\frac{d\phi}{dx} - jwA_x) - \mu J_x \tag{3.22}$$

$$\frac{d^2A_x}{dx^2} + \frac{d^2A_y}{dy^2} + \frac{d^2A_z}{dz^2} = -\mu(\sigma + jw\epsilon)(-\frac{d\phi}{dy} - jwA_y) - \mu J_y \tag{3.23}$$

$$\frac{d^2A_x}{dx^2} + \frac{d^2A_y}{dy^2} + \frac{d^2A_z}{dz^2} = -\mu(\sigma + jw\epsilon)(-\frac{d\phi}{dz} - jwA_z) - \mu J_z \tag{3.24}$$

After computing $\mathbf{A}$ and ϕ, it is easy to obtain $\mathbf{B}$ and $\mathbf{E}$ fields using equations 3.17 and 3.18, respectively.

3.2.4 Quasi-Static Formulation

The material properties (σ, ϵ and μ) and size of the body, together with the frequency band restrictions of the application may bring forth considerable simplifications in the Maxwell's equations. The common assumption for biological applications is the quasi-static assumption. As the name implies, the quasi-static condition assumes slowly varying electromagnetic fields such that they can be considered as nearly static.

For quasi-static fields, the Maxwell's equations for $\mathbf{E}$ and $\mathbf{B}$, and $\mathbf{A}$-ϕ formulations are expressed as follows:

$$\nabla \times \mathbf{E} = -jw\mathbf{B} \tag{3.25}$$

$$\nabla \times \mathbf{B} = \mu\mathbf{J}_s \tag{3.26}$$

$$\nabla \cdot \sigma \nabla \phi = -jw\mathbf{A} \cdot \nabla \sigma \quad (3.27)$$

$$\nabla^2 \mathbf{A} = -\mu\sigma(-\nabla\phi - jw\mathbf{A}) - \mu\mathbf{J}_s \quad (3.28)$$

where the dropped terms represents the contribution of the displacement currents inside the biological medium.

By using these equations, and assuming a negligible change in $\mathbf{A}$ due to induced currents in the conductive medium (induced currents are much smaller than the primary currents $\mathbf{J}_s$ in the coil system) the solution of electromagnetic fields can be considerably simplified.

3.2.5 Boundary Conditions

To solve the electromagnetic fields in a specific region in space, boundary conditions must be specified. .

A conceivable condition for the unknown evanescent field is that the field strength is negligible for considerably distant points from the source. This brings forth,

$$\mathbf{E} = 0 \quad (3.29)$$

$$\mathbf{B} = 0 \quad (3.30)$$

$$\mathbf{A} = 0 \quad (3.31)$$

$$\phi = 0 \quad (3.32)$$

at the boundary. The Maxwell's equations are not differentiable at the interface of Ω_N and Ω_C regions, therefore the normal components of the electric and magnetic field densities ($\mathbf{D}$ and $\mathbf{H}$) to the interface should be continuous.

A more conceivable condition for the solution of *evanescent fields* can also be obtained. Let the field ξ splits into two components, i.e., *linearly* as $\xi = \xi_p + \xi_s$ where ξp represents primary field due to the currents in the coil and ξ_s denotes the secondary field due to induced currents. Instead of forcing $\xi_p + \xi_s$ to be zero at a distant point from the object and source, assigning only ξ_s to be zero may lead a better solution inside the region of interest.

Moreover as explained in previous section, frequency band restrictions brings forth some simplification of equations. Decoupling of the equations provides a confinement of the solution region inside the boundary of the object. Since the permittivity of the body tissues are much more higher than the free space permittivity, the normal component of electric field density should vanish at the interface. The boundary condition for $\mathbf{E}$ and ϕ fields can be adopted by using the fact that the normal component of $\mathbf{J}$ is zero at the body boundary (Neumann type boundary). By using equations 3.18 and 3.8, conditions for the $\mathbf{E}$ and ϕ fields can be written on the object boundary as,

$$\mathbf{E} \cdot \mathbf{n} = 0 \tag{3.33}$$

$$\frac{\partial \phi}{\partial n} = -jw\mathbf{A} \cdot \mathbf{n} \tag{3.34}$$

where $\mathbf{n}$ is the outward unit normal to the boundary.

3.3 Measurement of Electromagnetic Fields

After computing the electromagnetic fields inside the body, the induced currents can be easily obtained from $\mathbf{J} = (\sigma + jw\epsilon)(-\nabla\phi - jw\mathbf{A})$. The secondary magnetic flux density due to these currents can be numerically evaluated from Biot-Savart Law,

$$\mathbf{B} = -\frac{\mu_0}{4\pi} \int ((\sigma + jw\epsilon)(\nabla\phi + jw\mathbf{A})) \times \frac{\mathbf{R}}{R^3} dV \tag{3.35}$$

where the μ_0 is the free-space permeability and $\mathbf{R}$ is the pointing vector from the source point to the field point. If the coil is carrying a current of I Amperes, the change in the impedance of the coil can be found by using the Lenz's Law as,

$$Z = -\frac{jw}{I} \int_{coil} \mathbf{B} \cdot d\mathbf{S} \tag{3.36}$$

where I is the current passing through the coil, and $d\mathbf{S}$ is the unit surface vector normal to the coil axis.

3.3.1 Sensitivity Analysis

To understand the capabilities of the system, the sensitivity maps should be investigated. Since both ϕ and $\mathbf{A}$ is dependent on the electrical properties, the relationship is rather complicated [45]. The effect of a perturbation in conductivity $\Delta\sigma$ or permittivity $\Delta\epsilon$ to the field measurements $\Delta\mathbf{B}_s$ can be formulated. A perturbation in conductivity will cause a change in ϕ and $\mathbf{A}$ fields by $\Delta\phi$ and $\Delta\mathbf{A}$, respectively. Therefore if a small change in conductivity is assumed,

$$\mathbf{B}_\sigma = -\frac{\mu_0}{4\pi}\int((\sigma+\Delta\sigma)+jw\epsilon)(\nabla(\phi+\Delta\phi)+jw(\mathbf{A}+\Delta\mathbf{A})))\times\frac{\mathbf{R}}{R^3}dV \quad (3.37)$$

and by separating the integrals,

$$\begin{aligned}\mathbf{B}_\sigma = &-\frac{\mu_0}{4\pi}\int((\sigma+jw\epsilon)(\nabla\phi+jw\mathbf{A}))\times\frac{\mathbf{R}}{R^3}dV\\ &-\frac{\mu_0}{4\pi}\int((\sigma+jw\epsilon)(\nabla(\Delta\phi)+jw\Delta\mathbf{A}))\times\frac{\mathbf{R}}{R^3}dV\\ &-\frac{\mu_0}{4\pi}\int(\Delta\sigma(\nabla\phi+jw\mathbf{A}))\times\frac{\mathbf{R}}{R^3}dV\\ &-\frac{\mu_0}{4\pi}\int(\Delta\sigma(\nabla(\Delta\phi)+jw\Delta\mathbf{A}))\times\frac{\mathbf{R}}{R^3}dV\end{aligned} \quad (3.38)$$

The last term in the right had side has second order variation and neglected and it is easy to see that the first integral above is equal to $\mathbf{B}_s$. Consequently the change between the fields is defined as ($\Delta\mathbf{B}$=$\mathbf{B}$-$\mathbf{B}_s$),

$$\begin{aligned}\Delta\mathbf{B}_\sigma = &-\frac{\mu_0}{4\pi}\int((\sigma+jw\epsilon)(\nabla(\Delta\phi)+jw\Delta\mathbf{A}))\times\frac{\mathbf{R}}{R^3}dV\\ &-\frac{\mu_0}{4\pi}\int(\Delta\sigma(\nabla\phi+jw\mathbf{A}))\times\frac{\mathbf{R}}{R^3}dV\end{aligned} \quad (3.39)$$

A similar formulation can be made to calculate the change of the field of the sensor to perturbations in permittivity,

$$\begin{aligned}\Delta\mathbf{B}_\epsilon = &-\frac{\mu_0}{4\pi}\int((\sigma+jw\epsilon)(\nabla(\Delta\phi)+jw\Delta\mathbf{A}))\times\frac{\mathbf{R}}{R^3}dV\\ &-\frac{\mu_0}{4\pi}\int(jw\Delta\epsilon(\nabla\phi+jw\mathbf{A}))\times\frac{\mathbf{R}}{R^3}dV\end{aligned} \quad (3.40)$$

Once the field perturbation is obtained, impedance change of the coil is found by equation 3.36

Another approach to calculate the sensitivity maps is using the generalized version of Geselowitz relationship [7] which is generally used for EIT sensitivity calculations based on the reciprocity theorem. The mutual impedance is a function of electrical properties of the object,

$$\Delta Z = \int (\Delta\sigma + jw\Delta\epsilon)\mathbf{L}_1 \cdot \mathbf{L}_2 dv + jw \int \mu \mathbf{K}_1 \cdot \mathbf{K}_2 dV \tag{3.41}$$

where the generalized electric and magnetic lead vectors are defined as,

$$\mathbf{L}_1 = \frac{\mathbf{E}_1}{I_1}, \mathbf{L}_2 = \frac{\mathbf{H}_1}{I_1} \tag{3.42}$$

$$\mathbf{L}_2 = \frac{\mathbf{E}_2}{I_2}, \mathbf{K}_2 = \frac{\mathbf{H}_2}{I_2} \tag{3.43}$$

Since in biological sources the second term related with the permeability can be neglected and using the equation $\mathbf{E} = -\nabla\phi - jw\mathbf{A}$, it is easy to derive,

$$\begin{aligned}\Delta Z = \frac{1}{I_1 I_2} \int & [\Delta\sigma(\nabla\phi_1 \cdot \nabla\phi_2 - w^2 \mathbf{A}_1 \cdot \mathbf{A}_2) - w^2\Delta\epsilon(\mathbf{A}_2 \cdot \nabla\phi_1 + \mathbf{A}_1 \cdot \nabla\phi_2)] \\ & + j[w\Delta\sigma(\mathbf{A}_2 \cdot \nabla\phi_1 + \mathbf{A}_1 \cdot \nabla\phi_2) + w\Delta\epsilon(\nabla\phi_1 \cdot \nabla\phi_2 - w^2 \mathbf{A}_1 \cdot \mathbf{A}_2)] dV\end{aligned} \tag{3.44}$$

where subscripts $_1$ and $_2$ corresponds to the transmitter and receiver coils. It can be shown that if the conducting body has antisymmetric geometry $\nabla\phi$ will vanish which will result in,

$$\Delta Z = -\frac{w^2}{I_1 I_2} \int (\Delta\sigma + jw\Delta\epsilon)(\mathbf{A}_1 \cdot \mathbf{A}_2) dV \tag{3.45}$$

If the receiver and transmitter coils are the same,

$$\Delta Z = -\frac{w^2}{I_1 I_2} \int (\Delta\sigma + jw\Delta\epsilon)|A|^2 dV \tag{3.46}$$

This is the case where Z is maximum. Therefore a single coil system which acts both as a transmitter and receiver seems to be the most appropriate for measurements.

CHAPTER 4

SOLUTION METHODS OF THE FORWARD PROBLEM

The differential equations governing the behavior of electromagnetic fields generated by a sinusoidal current carrying coil are given as,

$$\nabla \cdot ((\sigma + jw\epsilon)\nabla\phi) = -jw\mathbf{A} \cdot \nabla(\sigma + jw\epsilon) \quad (4.1)$$

$$\nabla^2\mathbf{A} = -\mu(\sigma + jw\epsilon)(-\nabla\phi - jw\mathbf{A}) - \mu\mathbf{J}_s \quad (4.2)$$

To solve the above equations for objects having arbitrary geometries, numerical methods must be employed. In this chapter, first the solutions for simple axi-symmetric objects will be presented, then the formulation for the adopted numerical method, the Finite Difference Method, will be introduced.

4.1 Analytical Methods

Analytical solutions are usually simple to implement, computationally less expensive, and provides a good idea of the field quantities for simple geometries. The analytical solutions for the near fields of a current carrying coil in free space are present in the literature, and it is the main concern in this section. Note that, if axi-symmetric objects are assumed, the problem reduces to that of solving the Poisson's equation in free space (i.e., $-\nabla\phi$ term vanishes).

4.1.1 Axi-symmetry Formulation

When there is axi-symmetry in coil/body configuration, solution of the following equation is required:

$$\nabla^2 \mathbf{A} = \mu_0 \mathbf{J}_s \tag{4.3}$$

From symmetry in cylindrical coordinates (ρ, ϕ, z), it is known that $\mathbf{A}$ has a single azimuthal component A_ϕ. The vector potential of a circular coil whose radius is a and carrying a current of I can be calculated as follows [4]:

$$A_\phi = \frac{\mu I}{\pi k}(\frac{a}{\rho})^{\frac{1}{2}}[(1-\frac{1}{2}k^2)K - E] \tag{4.4}$$

$$A_\phi = \frac{\mu I}{32}(\frac{a}{\rho})^{\frac{1}{2}}k^3(1+\frac{3}{4}k^2+\frac{75}{128}k^4+...) \tag{4.5}$$

where k^2 is defined as,

$$k^2 = 4a\rho[(a+\rho)^2+z^2]^{-1} \tag{4.6}$$

and K and E are the complete elliptic integrals of the first and second kind, as given below:

$$K(m) = \int_0^1 \frac{dt}{\sqrt{(1-t^2)(1-m^2t^2)}} \tag{4.7}$$

$$E(m) = \int_0^1 \frac{\sqrt{1-m^2t^2}}{\sqrt{1-t^2}}\, dt \tag{4.8}$$

where $0 \leq m \leq 1$ and $m = k^2$.

Since $\mathbf{B} = \nabla \times \mathbf{A}$, the components of the magnetic flux densities can be obtained as,

$$B_\rho = \frac{\mu I}{2\pi}\frac{z}{\rho[(a+\rho)^2+z^2]^{\frac{1}{2}}}[-K + \frac{a^2+\rho^2+z^2}{(a-\rho)^2+z^2}E] \tag{4.9}$$

$$B_z = \frac{\mu I}{2\pi}\frac{1}{[(a+\rho)^2+z^2]^{\frac{1}{2}}}[K + \frac{a^2-\rho^2-z^2}{(a-\rho)^2+z^2}E] \tag{4.10}$$

Numerical values of B_ρ and B_z can be computed for any value of ρ and z by finding k from 4.6 and finding the values of the elliptic integrals K and E.

Moreover it is seen from equation $\mathbf{E} = -\nabla\phi - jw\mathbf{A}$, that both ϕ and $\mathbf{A}$ fields are required to compute the $\mathbf{E}$ field. Since the $-\nabla\phi$ term vanishes for

axi-symmetric objects the induced currents inside the body can be found from the relation J_ϕ=$-jw\sigma A_\phi$,

$$J_\phi = -jw\sigma\frac{\mu I}{\pi k}(\frac{a}{\rho})^{\frac{1}{2}}[(1-\frac{1}{2}k^2)K - E] \tag{4.11}$$

The sensitivity of the coil can be found in a similar manner as discussed previously, (equation 3.46),

$$\Delta Z = -\frac{w^2}{I^2}\int |A|^2 dV \tag{4.12}$$

In this study, elliptic integrals are evaluated using a polynomial approximation is to reduce the computation time [3],

$$K(m) = (a_0+a_1m_1+...+a_4m_1^4)+(b_0+b_1m_1+...+b_4m_1^4)ln(1/m_1)+\epsilon(m_1) \tag{4.13}$$

$$a_0 = 1.38629436112 \qquad b_0 = 0.50000000000 \tag{4.14}$$

$$a_1 = 0.09666344259 \qquad b_1 = 0.12498593597 \tag{4.15}$$

$$a_2 = 0.03590092383 \qquad b_2 = 0.06880248576 \tag{4.16}$$

$$a_3 = 0.03742563713 \qquad b_3 = 0.03328355346 \tag{4.17}$$

$$a_4 = 0.01451196212 \qquad b_4 = 0.00441787012 \tag{4.18}$$

$$E(m) = (1+a_1m_1+...+a_4m_1^4)+(b_1m_1+...+b_4m_1^4)ln(1/m_1)+\epsilon(m_1) \tag{4.19}$$

$$a_1 = 0.44325141463 \qquad b_1 = 0.24998368310 \tag{4.20}$$

$$a_2 = 0.06260601220 \qquad b_2 = 0.09200180037 \tag{4.21}$$

$$a_3 = 0.04757383546 \qquad b_3 = 0.04069697526 \tag{4.22}$$

$$a_4 = 0.01736506451 \qquad b_4 = 0.00526449639 \tag{4.23}$$

where $\epsilon(m_1)$ is the numerical error ($|\epsilon(m_1)| \leq 2\cdot 10^{-8}$) and $m_1 = 1-m$.

4.2 Numerical Methods

In parallel with the increasing computing technology, there are also advances in the numerical methods used to solve partial differential equations. Apart from

the analytical methods, numerical methods can cope with the field solutions for more complex geometries at the cost of two major resources: computational time and physical memory needed for storage. The research in numerical algorithms is focused on the reduction of these resources in the solution of a specific problem. Variety of both time-domain and frequency-domain methods are present in the literature.

In this thesis study, the finite difference (FD) method will be used to model the field equations (Appendix A). Additionally, direct methods such as Successive Over Relaxation (SOR) or Jacobi methods are chosen for the solution. Detailed discussion can be found in Appendix B. Working with partial derivatives instead of integral equations provides some advantages, i.e, they do not need to formulate Green's functions for different structures. On the other hand, only the unknown potentials are stored and the solution is obtained by an iterative manner. These iterative field manipulations, instead of using algebraic tools (i.e. matrix inversion) to get the field solutions, causes a considerable reduction in memory usage. Since the field equation at a point is defined in terms of only neighboring fields, this leads to the massive parallel implementation of the FD approach. The major drawback of the FD method is incapability of modeling the boundaries accurately because of the the grid mesh used in the formulation [76].

4.2.1 Axi-symmetry Formulation

When the axi-symmetric objects are considered the field equation becomes,

$$\nabla^2 \mathbf{A} + k^2 \mathbf{A} = \mu_0 \mathbf{J}_s \tag{4.24}$$

where $k^2 = jw\mu(\sigma + jw\epsilon)$.

When the excitation source is a circular coil, it is suitable to use a cylindrical grid (ρ, ϕ, z) to reduce the dimension, since A_ϕ will be constant on ϕ-axis.

The definition of the Laplacian operator in cylindrical coordinate system is,

$$\nabla^2 = \frac{\partial^2}{\partial \rho^2} + \frac{1}{\rho}\frac{\partial}{\partial \rho} + \frac{\partial^2}{\partial z^2} - \frac{1}{\rho^2} \tag{4.25}$$

Therefore by using a 5-point cylindrical stencil, field equation 4.24 can be written in terms of the finite difference equations as,

$$\frac{A_{\phi 1} + A_{\phi 2} - 2A_{\phi 0}}{d\rho^2} + \frac{1}{\rho}\frac{A_{\phi 1} - A_{\phi 2}}{2d\rho} + \frac{A_{\phi 3} + A_{\phi 4} - 2A_{\phi 0}}{dz^2} - \frac{A_{\phi 0}}{\rho^2} + k_0^2 A_{\phi 0} = \mu J_\phi \tag{4.26}$$

where the subscripts at the field potential A_m denotes the grid mapping. By rearranging 4.35, $A_{\phi 0}$ can be represented as a linear combination of neighboring fields,

$$\sum_{i=0}^{4} a_i A_{\phi i} = b_0 J_\phi \tag{4.27}$$

where,

$$a_0 = -\frac{2d\rho^2 + 2dz^2 - d\rho^2 dz^2}{d\rho^2 dz^2 \rho^2} + k_0^2 \qquad b_0 = \mu \tag{4.28}$$

$$a_1 = \frac{2\rho + d\rho}{2\rho d\rho^2} \tag{4.29}$$

$$a_2 = \frac{2\rho - d\rho}{2\rho d\rho^2} \tag{4.30}$$

$$a_3 = \frac{1}{dz^2} \tag{4.31}$$

$$a_4 = \frac{1}{dz^2} \tag{4.32}$$

Note that when $\rho = 0$, the Laplacian operator 4.25 is singular. To overcome this, the two singular terms in 4.25 can be rewritten using the L'Hospital rule,

$$\lim_{\rho \to 0}\left(\frac{1}{\rho}\frac{\partial}{\partial \rho} - \frac{1}{\rho^2}\right) = \frac{\partial^2}{\partial \rho^2} \tag{4.33}$$

Thus at $\rho = 0$, the Laplacian operator 4.25 can be modified as,

$$\nabla^2 = \frac{3}{2}\frac{\partial^2}{\partial \rho^2} + \frac{\partial^2}{\partial z^2} \tag{4.34}$$

Therefore at the central axis of the coil line, the FD equations are as follows,

$$\frac{3}{2}\frac{A_{\phi 1} + A_{\phi 2} - 2A_{\phi 0}}{d\rho^2} + \frac{A_{\phi 3} + A_{\phi 4} - 2A_{\phi 0}}{dz^2} + k_0^2 A_{\phi 0} = \mu J_\phi \tag{4.35}$$

and consequently after revising the above expression we obtain,

$$a_0 = -\frac{2d\rho^2 + 3dz^2}{d\rho^2 dz^2} + k_0^2 \qquad b_0 = \mu \tag{4.36}$$

$$a_1 = \frac{3}{2d\rho^2} \tag{4.37}$$

$$a_2 = \frac{3}{2d\rho^2} \tag{4.38}$$

$$a_3 = \frac{1}{dz^2} \tag{4.39}$$

$$a_4 = \frac{1}{dz^2} \tag{4.40}$$

4.2.2 Arbitrary Shaped Object Formulation

4.2.2.1 Quasi-Static Case

For the low frequency applications, where the quasi-static assumptions hold, the equations gets decoupled as mentioned before. The **A** field is not modified by secondary fields. The relating equations can be written as,

$$\nabla \cdot \sigma \nabla \phi = -jw\mathbf{A} \cdot \nabla \sigma \tag{4.41}$$

$$\nabla^2 \mathbf{A} = \mu \mathbf{J}_s \tag{4.42}$$

where the $\mathbf{J}_s$ is the source current density. Analytical solution of the second equation is present and **A** field can be easily computed analytically. Then the resulting **A** field is substituted into first equation to solve ϕ field.

For a body of arbitrary shape, using a specific coordinate system does not provide any convenience because of the object's asymmetry. Therefore, as a routine, Cartesian grid is chosen. If 7-point cartesian stencil is used, 4.41 is expressed in terms of finite differences as,

$$\frac{\sigma_1 - \sigma_2}{2dx}\frac{\phi_1 - \phi_2}{2dx} + \sigma_0\left(\frac{\phi_1 + \phi_2 - 2\phi_0}{dx^2}\right) + ... = -jwA_{x0}\left(\frac{\sigma_1 - \sigma_2}{2dx}\right) - ... \tag{4.43}$$

where the subscript n at ϕ_n denotes the grid mapping. By some modifications the FD equation 4.43 becomes,

$$\sum_{i=0}^{6} p_i \phi_i = a_{x0}A_{x0} + a_{y0}A_{y0} + a_{z0}A_{z0} \tag{4.44}$$

where,

$$p_0 = -\frac{2\sigma_0}{dx^2 + dy^2 + dz^2} \tag{4.45}$$

$$p_1 = \frac{4\sigma_0 + \sigma_1 - \sigma_2}{4dx^2} \tag{4.46}$$

$$p_2 = \frac{4\sigma_0 + \sigma_2 - \sigma_1}{4dx^2} \quad (4.47)$$

$$p_3 = \frac{4\sigma_0 + \sigma_3 - \sigma_4}{4dy^2} \quad (4.48)$$

$$p_4 = \frac{4\sigma_0 + \sigma_4 - \sigma_3}{4dy^2} \quad (4.49)$$

$$p_5 = \frac{4\sigma_0 + \sigma_5 - \sigma_6}{4dz^2} \quad (4.50)$$

$$p_6 = \frac{4\sigma_0 + \sigma_6 - \sigma_5}{4dz^2} \quad (4.51)$$

$$a_{x0} = -jw(\frac{\sigma_1 - \sigma_2}{2dx}) \quad (4.52)$$

$$a_{y0} = -jw(\frac{\sigma_3 - \sigma_4}{2dy}) \quad (4.53)$$

$$a_{z0} = -jw(\frac{\sigma_5 - \sigma_6}{2dz}) \quad (4.54)$$

$$(4.55)$$

In quasi-static frequency band, the boundary equation for ϕ can be written as a combination of the following expressions,

$$\frac{\phi_1 - \phi_2}{2dx} = -jwA_x \quad (4.56)$$

$$\frac{\phi_3 - \phi_4}{2dy} = -jwA_y \quad (4.57)$$

$$\frac{\phi_5 - \phi_6}{2dz} = -jwA_z \quad (4.58)$$

at the object boundary. Although from the definition of central difference theorem, at the boundary grids one unknown field lies outside the grid structure, this grid can be eliminated between equations 4.43 and 4.56, 4.57, 4.58 to obtain a complete set of equations inside the domain.

4.2.2.2 High Frequency Case

For the high frequency applications, the coupled equation should be solved simultaneously. The differential equations with unknown fields ϕ and $\mathbf{A}$ for a general media is written as derived previously,

$$\nabla \cdot ((\sigma + jw\epsilon)\nabla\phi) = -jw\mathbf{A} \cdot \nabla(\sigma + jw\epsilon) \quad (4.59)$$

$$\nabla^2\mathbf{A} = \mu(\sigma + jw\epsilon)(-\nabla\phi - jw\mathbf{A}) + \mu\mathbf{J}_s \quad (4.60)$$

For an object of arbitrary shape, by using the similar notation used in quasi-static case, 4.59-4.60 are expressed in terms of finite differences as,

$$\frac{(\sigma+jw\epsilon)_1-(\sigma+jw\epsilon)_2}{2dx}\frac{\phi_1-\phi_2}{2dx}+(\sigma+jw\epsilon)_0(\frac{\phi_1+\phi_2-2\phi_0}{dx^2})+...= -jwA_{x0}(\frac{(\sigma+jw\epsilon)_1-(\sigma+jw\epsilon)_2}{2dx})-... \quad (4.61)$$

$$\frac{A_{x1}+A_{x2}-2A_{x0}}{dx^2}+\frac{A_{x3}+A_{x4}-2A_{x0}}{dy^2}+\frac{A_{x5}+A_{x6}-2A_{x0}}{dz^2}= \mu(\sigma+jw\epsilon)_0(-\frac{\phi_1-\phi_2}{2dx}-jwA_{x0})+\mu J_x \quad (4.62)$$

$$\frac{A_{y1}+A_{y2}-2A_{y0}}{dx^2}+\frac{A_{y3}+A_{y4}-2A_{y0}}{dy^2}+\frac{A_{y5}+A_{y6}-2A_{y0}}{dz^2}= \mu(\sigma+jw\epsilon)_0(-\frac{\phi_3-\phi_4}{2dy}-jwA_{y0})+\mu J_y \quad (4.63)$$

$$\frac{A_{z1}+A_{z2}-2A_{z0}}{dx^2}+\frac{A_{z3}+A_{z4}-2A_{z0}}{dy^2}+\frac{A_{z5}+A_{z6}-2A_{z0}}{dz^2}= \mu(\sigma+jw\epsilon)_0(-\frac{\phi_5-\phi_6}{2dz}-jwA_{z0})+\mu J_z \quad (4.64)$$

where the subscripts at the field potentials, A_m and ϕ_n denotes the grid mapping. After modification, the FD equation 4.61 is written as,

$$\sum_{i=0}^{6} p_i\phi_i = a_{x0}A_{x0}+a_{y0}A_{y0}+a_{z0}A_{z0} \quad (4.65)$$

where,

$$p_0 = -\frac{2(\sigma+jw\epsilon)_0}{dx^2+dy^2+dz^2} \quad (4.66)$$

$$p_1 = \frac{4(\sigma+jw\epsilon)_0+(\sigma+jw\epsilon)_1-(\sigma+jw\epsilon)_2}{4dx^2} \quad (4.67)$$

$$p_2 = \frac{4(\sigma+jw\epsilon)_0+(\sigma+jw\epsilon)_2-(\sigma+jw\epsilon)_1}{4dx^2} \quad (4.68)$$

$$p_3 = \frac{4(\sigma+jw\epsilon)_0+(\sigma+jw\epsilon)_3-(\sigma+jw\epsilon)_4}{4dy^2} \quad (4.69)$$

$$p_4 = \frac{4(\sigma+jw\epsilon)_0+(\sigma+jw\epsilon)_4-(\sigma+jw\epsilon)_3}{4dy^2} \quad (4.70)$$

$$p_5 = \frac{4(\sigma+jw\epsilon)_0+(\sigma+jw\epsilon)_5-(\sigma+jw\epsilon)_6}{4dz^2} \quad (4.71)$$

$$p_6 = \frac{4(\sigma+jw\epsilon)_0+(\sigma+jw\epsilon)_6-(\sigma+jw\epsilon)_5}{4dz^2} \quad (4.72)$$

$$a_{x0} = -jw(\frac{(\sigma+jw\epsilon)_1-(\sigma+jw\epsilon)_2}{2dx}) \quad (4.73)$$

$$a_{y0} = -jw(\frac{(\sigma+jw\epsilon)_3-(\sigma+jw\epsilon)_4}{2dy}) \quad (4.74)$$

$$a_{z0} = -jw(\frac{(\sigma + jw\epsilon)_5 - (\sigma + jw\epsilon)_6}{2dz}) \tag{4.75}$$

$$\tag{4.76}$$

and 4.62 becomes,

$$\sum_{i=0}^{6} a_{xi} A_{xi} = \sum_{l=1}^{2} p_l \phi_l + b_1 J_\phi \tag{4.77}$$

where,

$$p_1 = -\frac{\mu(\sigma + jw\epsilon)_0}{2dx} \tag{4.78}$$

$$p_2 = \frac{\mu(\sigma + jw\epsilon)_0}{2dx} \tag{4.79}$$

$$a_{x0} = -\frac{2}{dx^2} - \frac{2}{dy^2} - \frac{2}{dz^2} + jw\mu(\sigma + jw\epsilon)_0 \tag{4.80}$$

$$a_{x1} = a_{x2} = \frac{1}{dx^2} \tag{4.81}$$

$$a_{x3} = a_{x4} = \frac{1}{dy^2} \tag{4.82}$$

$$a_{x5} = a_{x6} = \frac{1}{dz^2} \tag{4.83}$$

$$b_1 = \mu \tag{4.84}$$

Since there is no major difference between 4.62 and 4.63, 4.64, detailed formulation can be obtained by using 4.62 for the rest of the two equations.

At the interior grids the above expressions hold except the interface points. At the boundary grids, the boundary conditions should be adopted. If the field is assumed to be negligible at a distant point from the source, this field is forced to be zero at these grids. However as mentioned in the previous chapter,

$$\mathbf{A} = 0 \tag{4.85}$$

$$\phi = 0 \tag{4.86}$$

At the interface grids, the permittivity of free space compared with body tissues are negligible even at high frequencies, the 4.56, 4.57, 4.58 equations are adopted at the interfaces.

CHAPTER 5

RESULTS

5.1 Analytical Solutions

The analytical solutions for axi-symmetric objects are formulated in the previous section and the results are introduced here for different models.

A circular coil of radius 1 cm and carrying a 50 kHz sinusoidal current of 1 Ampere is used for excitation source and corresponding magnetic vector potential A_ϕ is presented in Figure 5.1(a). In order to find the sensitivity of the coil, the free space is represented by circular rings placed coaxial to the coil. If the rings has a unity conductivity, the induced current density passing through them can be obtained. Therefore, by using the Biot-Savart Law, the contribution of each ring to the total impedance change can be found Figure 5.1(b).

In Figure 5.2, both cylindrical and spherical solutions of the same configuration is presented. The coil is chosen to be 1 cm above the bodies. The body conductivity is chosen as 0.2 S/m in order to resemble body tissues correctly. Maximum current density is found to be 5.2×10^{-3} A/m^3 for cylindrical case and 4.2×10^{-3} A/m^3 for spherical case.

The low frequency electrical properties of head tissues were given previously. By using these values a multi-shell spherical head model is constructed. The head model includes skin, skull, CSF, gray matter and white matter tissues from surface to the inner head respectively. Since the electrical conductivity of CSF is very high compared to other tissues, the magnitude of induced currents

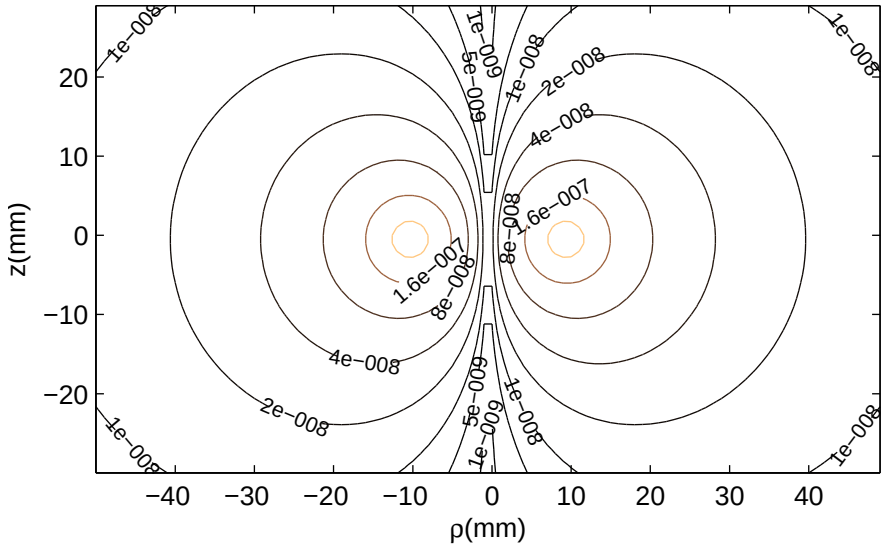

(a)

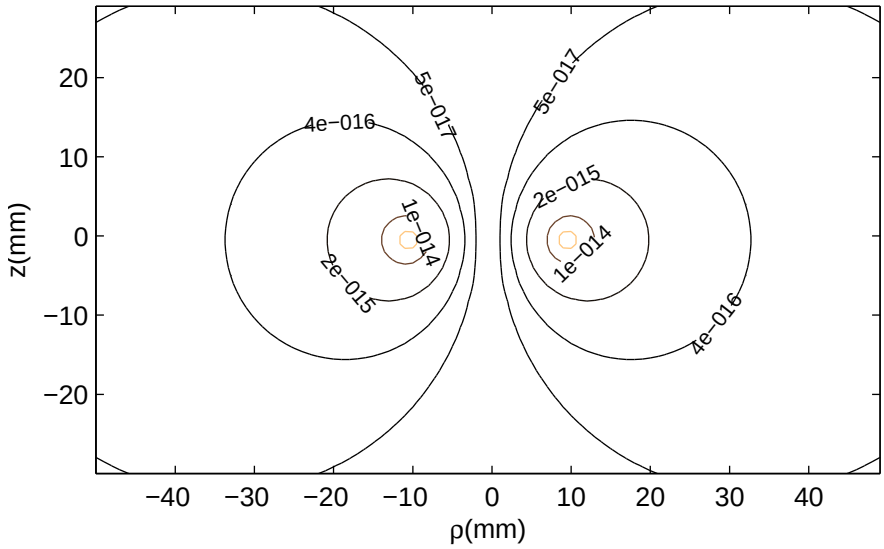

(b)

Figure 5.1: The magnetic vector potential $\mathbf{A}_\phi$ and sensitivity map for a coil of 1 cm radius in free space at 100 kHz, (a) $|\mathbf{A}_\phi|$ (Wb/m), (b) sensitivity map of the coil according to reciprocity theorem (derived in 3.41).

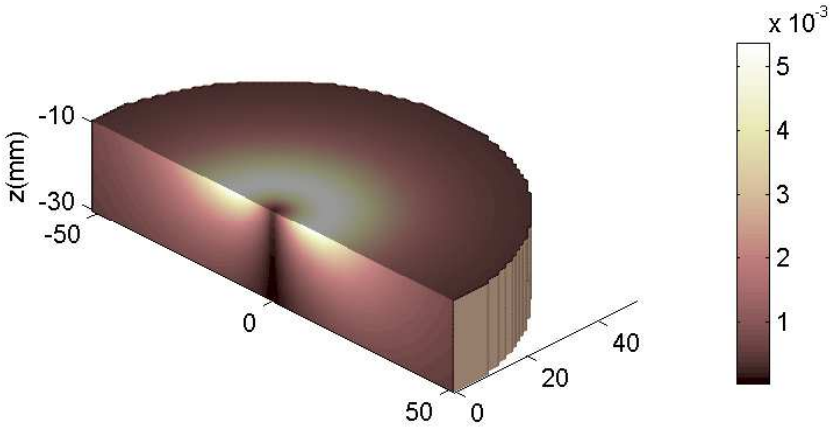

(a)

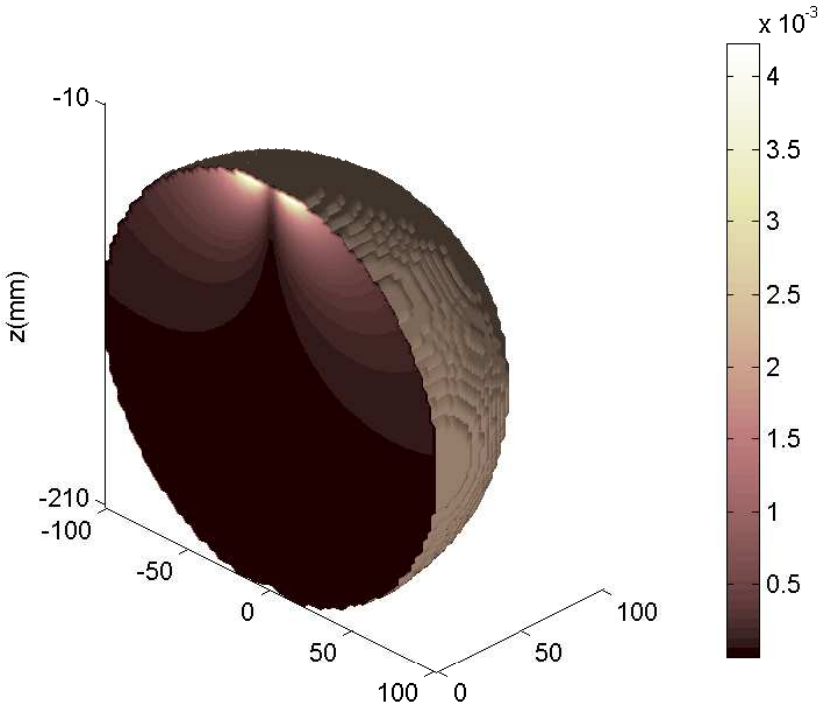

(b)

Figure 5.2: Induced current density distribution (A/m^2) inside a uniform conductive body, (a) cylindrical body, (b) spherical body. Body conductivity is chosen as the average conductivity (0.2 S/m) and operating frequency is 50 kHz. The coil is placed 10 mm above the body.

is high in CSF (Figure 5.3(a)). Since CSF is a thin layer, neglecting this tissue will result in the following current density distribution which can be seen at Figure 5.3(b). The maximum current density is found to be 8.4×10^{-3} A/m^3 in CSF tissue.

5.2 Numerical Results

The main motivation of this study is to solve the electromagnetic fields inside the head model. Therefore, initially, two models are constructed to test multi frequency measurements and to explore induced current densities inside the head tissues: the uniform head model and the multi-shell head model. In the latter studies, a realistic head model is used to achieve more realistic observations.

5.2.1 Accuracy of Numerical Solutions

To assess the performance of the numerical solutions, first the Maxwell's equations written in terms of finite differences are tested. The iterative solver also uses this principle (solves the Maxwell's equation at each grid and stops if the Maxwell's equations are satisfied) for updating the fields. The accuracy of the numerical solver is tested by comparing the results with respect to the previous models developed in the literature.

For the field computation by coil excitation, there exists analytical solutions for the models that has axi-symmetric geometries. For accuracy tests, the percentage RDM, and $RDM^\star$ are used [16],

$$\%RDM = \sqrt{\frac{\sum_{i=1}^{m}(V_i' - V_i)^2}{\sum_{i=1}^{m}(V_i')^2}} \times 100 \tag{5.1}$$

$$RDM^\star = \sqrt{\sum_{i=1}^{m}\left(\frac{(V_i')}{\sum_{i=1}^{m}(V_i')^2} - \frac{(V_i)}{\sum_{i=1}^{m}(V_i')^2}\right)^2} \tag{5.2}$$

where V' and V are chosen as the analytical and numerical solutions, respectively. In numerical computations, since it is not possible to solve the problem for the entire infinite region, the boundary conditions will contribute to the

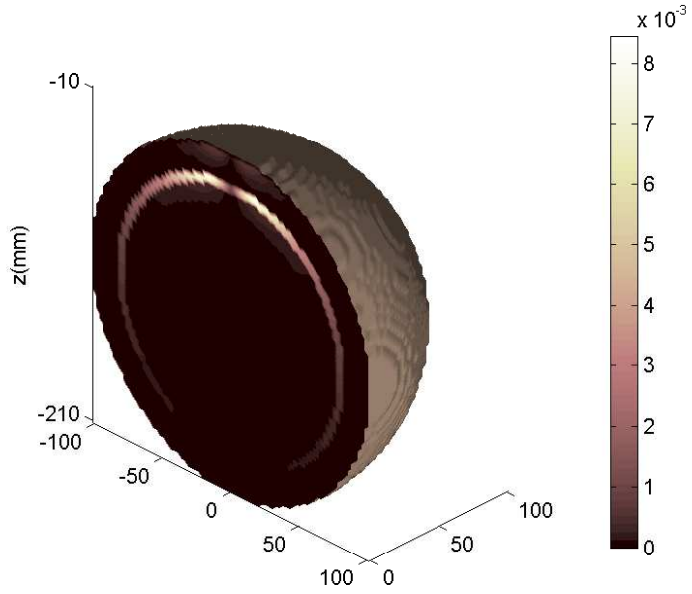

(a)

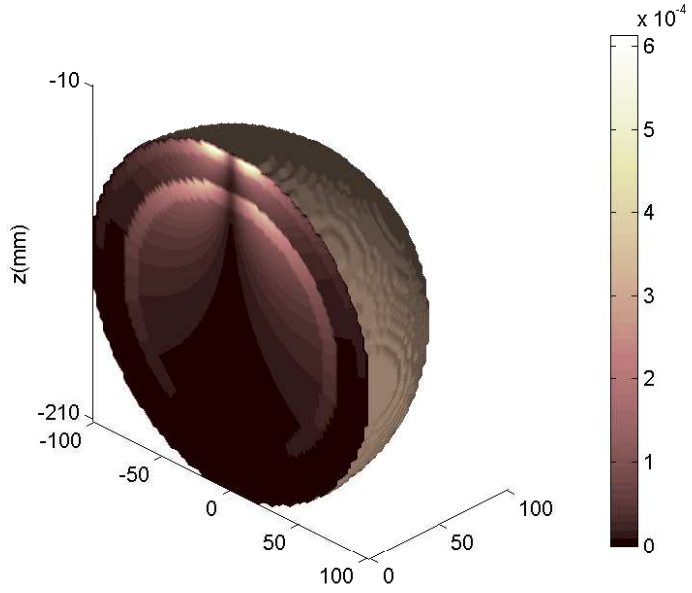

(b)

Figure 5.3: Induced current density distribution (A/m^2) inside a multi-shell head model, (a) CSF ignored, (b) CSF not ignored. Operating frequency is chosen as 50 kHz. The coil is placed 10 mm above the body.

error in the numerical solutions. As explained previously, in the numerical solutions the fields are assumed to be zero at boundaries. Therefore by increasing the computation domain, the numerical solutions are expected to converge to the analytical ones. The accuracy results for increasing the size of the computational domain as a multiple of the coil radius are given in Table 5.1. The absolute difference between the analytical and numerical results are presented in Figure 5.4.

Table 5.1: The accuracy in solutions as a function of the computational domain (calculated as a multiple of the coil radius). r_{coil} is the transmitter coil's radius and R_{domain} is the radius of computational domain.

R_{domain}	$\%RDM$	$RDM^{\star}$
$2 \times r_{coil}$	29.598	0.2436
$3 \times r_{coil}$	18.946	0.1726
$4 \times r_{coil}$	14.077	0.1331
$5 \times r_{coil}$	11.235	0.1082
$6 \times r_{coil}$	9.362	0.0911
$7 \times r_{coil}$	8.033	0.0787
$8 \times r_{coil}$	7.040	0.0693
$9 \times r_{coil}$	6.270	0.0619
$10 \times r_{coil}$	5.656	0.0560

In order to test the stability of the numerical solver, the percentage RDM, and $RDM^{\star}$ are used as well. In this case V', and V are defined as,

$$V' = \sum_{i=1}^{m} (V_i^{new} - V_i^{old}) \tag{5.3}$$

$$V = V^{old} \tag{5.4}$$

where *old* and *new* is the previous and current state of the iteration. In Figure 5.5 the percent RDM errors of the Maxwell's equations by using the SOR algorithm is shown for a realistic head model at 50 kHz operating frequency. The algorithm converges very fast in the first few iterations. It takes 30-40 iterations to reduce the error less than 1%. Similarly, in Figure 5.7, the percent RDM errors of Maxwell's equations per iteration for the same model at 10 MHz is plotted. The coupled equation is solved iteratively obtaining one field from the other field (for example, first $\mathbf{A}$ field is computed then ϕ field is

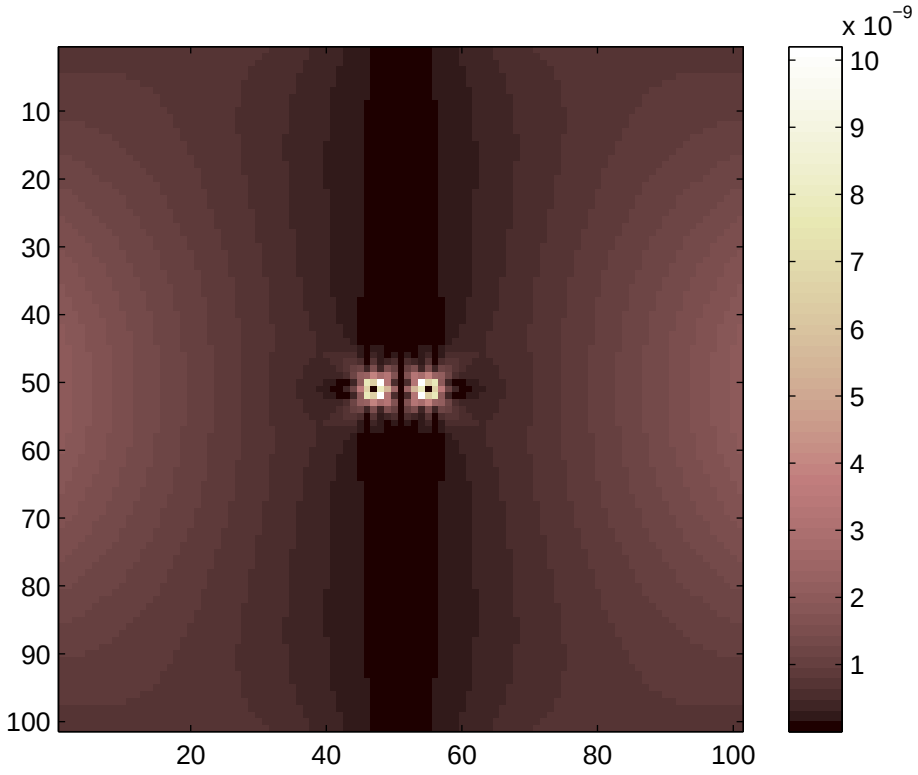

Figure 5.4: The absolute error between analytical vs. numerical computation of **A** field in free space. The coil radius is selected as 1 cm.

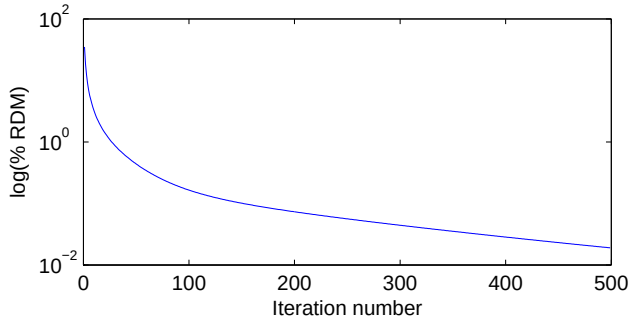

Figure 5.5: Percentage RDM values per ϕ field iterations.

updated using the computed **A** field. Afterwards **A** field is computed from the ϕ field and the iterations goes like this manner). Total of 5 major iterations are done where the number of minor iterations are chosen as 400 for **A** field computations and 200 for the ϕ field computations. As can be seen at the 400^{th}, 800^{th}, 1600^{th} and 1600^{th} iterations the **A** field is not changed considerably (It is expected to change as a result of change in ϕ field) [1]

For the first test case, the half-space problem is simulated by a $9 \times 9 \times 5$ cm body of uniform conductivity (0.2 S/m). The body is excited by a current carrying coil (1 A, 1 turn, 1 cm above the conducting body, at 50 kHz). The grid size is chosen as $2.5 \times 2.5 \times 2.5$ mm and 25920 nodes are generated. SOR of 100 iterations is used for solution. The analytical solutions for the half-space were calculated in [41]. In that study, the maximum current density and impedance change for a coplanar receiver coil (5 cm away from the transmitter coil) were reported as $4.9 \times 10^{-3} A/m^2$ and $11.4 \times 10^{-6} \Omega$, respectively. The same parameters are calculated as $4.2 \times 10^{-3} A/m^2$ and $9.6 \times 10^{-6} \Omega$ using the numerical approach. It is observed that, the analytical solutions for the half-space and the numerical solutions for the simulating bounded uniformly conductive body are quite close to each other for the same excitation conditions.

Another test can be established by observing the pattern of solutions. In Figure 5.8, a cubic model (30x30x30 mm) of conductivity (0.2 S/m) located 1 cm below of a coil of radius 1 cm is shown. The operating frequency is chosen as 50 kHz and corresponding vector based representation of the induced current

[1] Consequently it will be mentioned later that from this result it is concluded that the inductive effects and propagative effects at 10 MHz are negligibly small.

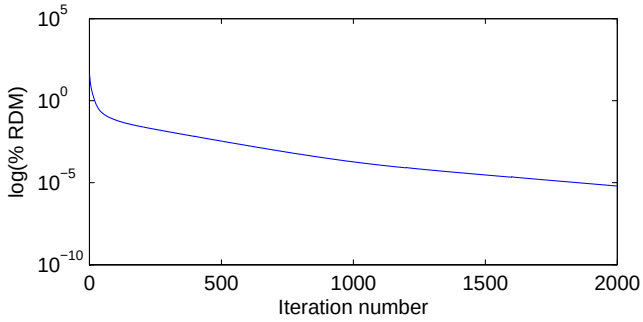

(a)

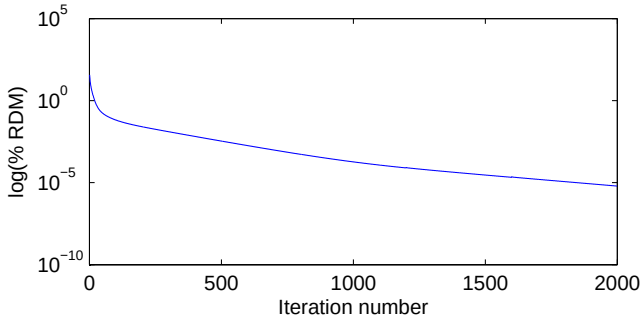

(b)

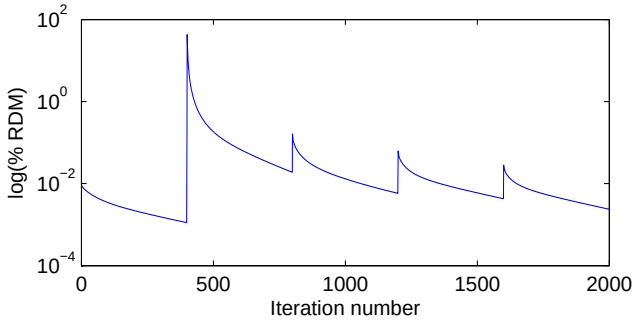

(c)

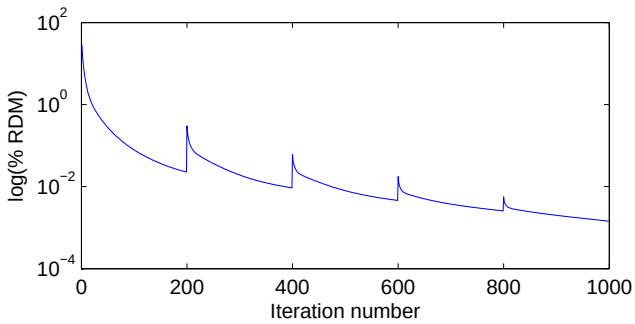

(d)

Figure 5.6: Percentage RDM values for each iteration. (a) $\mathbf{A}_x$,(b) $\mathbf{A}_y$, (c) $\mathbf{A}_z$ (d) ϕ field iterations.

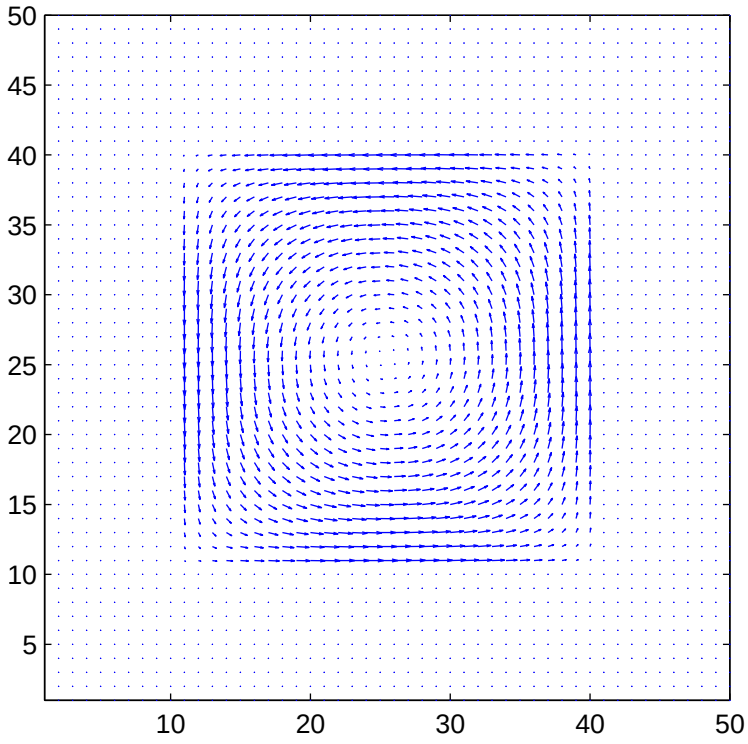

Figure 5.7: Vector based representation of the induced current density (A/m^2) inside the cubic conductive body (30x30x30 mm). The excitation coil is centrally placed above the body.

density is presented in Figure 5.8. The currents paths are shown to be normal to the surface, as expected.

5.2.2 Homogeneous Spherical Head Model

The homogeneous head model is easy to construct and requires little computation time. Furthermore, it gives chances to explore the behavior of the magnetic vector potential **A** for high frequencies. The electrical properties of the model is chosen as the typical values of head tissues. The simulation results for 50 kHz are presented in the previous parts. In this subsection, the results for operating frequencies $> 10MHz$ is shown. The simulations are achieved in 3 frequencies, 10 MHz, 100 MHz and 500 MHz to cover a wide frequency range. For each case, the primary and secondary magnetic vector potentials are compared.

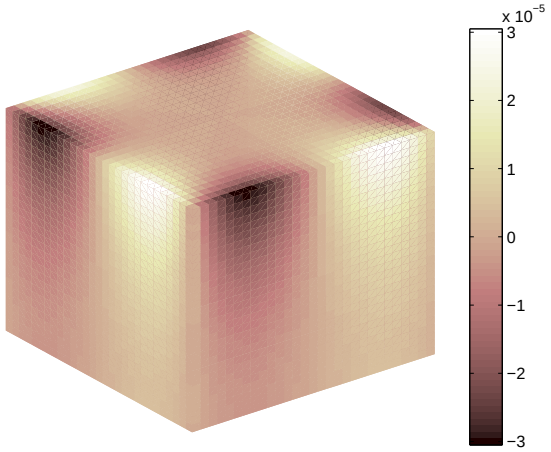

(a)

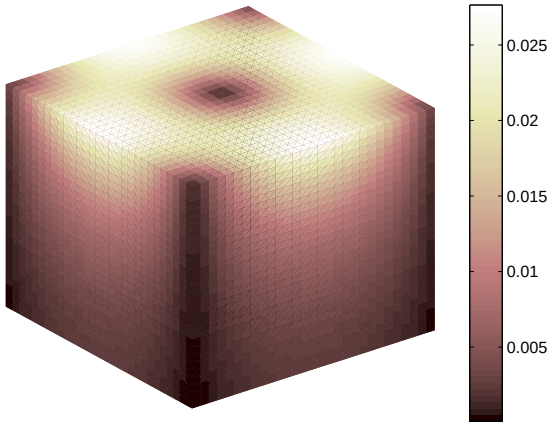

(b)

Figure 5.8: A cubic model (30x30x30 mm) of average body conductivity (0.2 S/m) located below (1 cm) a coil of radius 1 cm, (a) scalar potentials, (b) induced current density at 50 kHz.

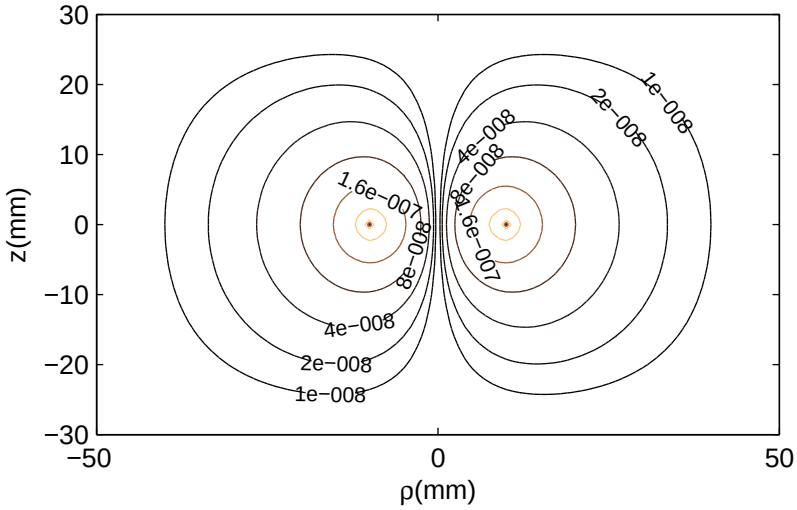

Figure 5.9: Numerical computation of $|\mathbf{A}_\phi|$ (Wb/m) using the SOR algorithm with a weighting factor of 1.95.

For spherical head models when the coil axis is in radial direction $\nabla\phi$ vanishes. Thus, solution of $\mathbf{A}$ is sufficient to obtain the induced current density distributions. Figure 5.9 shows the $\mathbf{A}$ obtained numerically. To obtain the results, the equations of the axi-symmetric formulation are updated by using the SOR algorithm with a weighting factor of 1.95. The relative error for the stopping criteria is chosen to be less than %0.1. Figure 5.10 shows $\mathbf{A}$ field for three different frequencies. It is observed that, the secondary fields are becoming comparable with the primary fields when the operation frequency is increased. Note that when the frequency is 10 MHz, the change in $\mathbf{A}$ is not noticeable. Thus,one may neglect both the induction and propagation effects for operation frequencies lower than 10 MHz for the head.

The current density distribution inside the homogeneous head model are presented in Figure 5.11 for 10 MHz. The body conductivity and permittivity values are taken as 0.45 S/m and 180.2 F/m. The maximum current density inside the model is found to be $2.2A/m^2$. The ratio of the displacement currents to conductive currents is found to be 0.23.

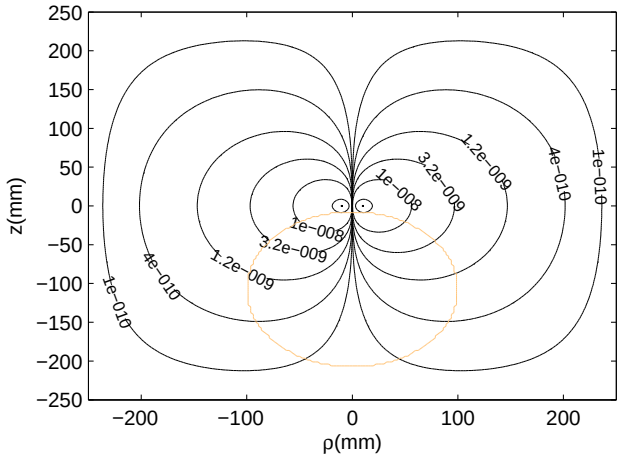

(a)

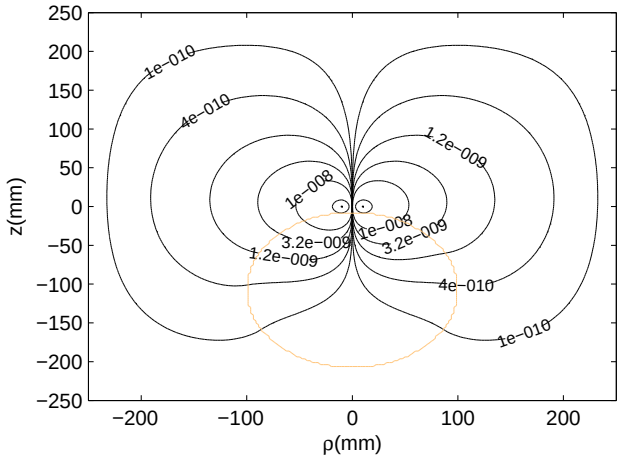

(b)

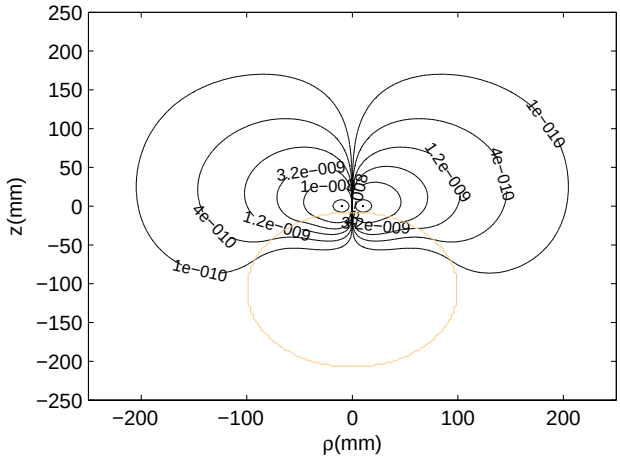

(c)

Figure 5.10: Numerical computation of the $|\mathbf{A}_\phi|$ field (Wb/m) generated by a circular coil. The coil carries 1 Ampere sinusoidal current at a frequency of (a) 10 MHz, (b) 100 MHz, (c) 500 MHZ. The SOR algorithm is used with a weighting factor of 1.95.

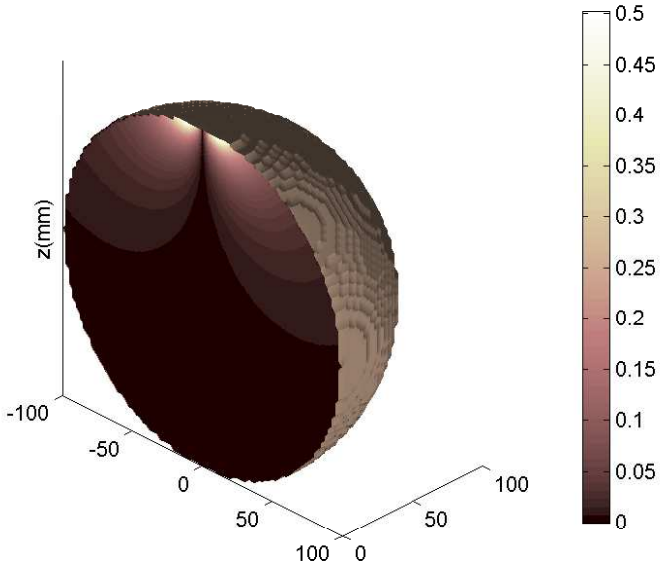

(a)

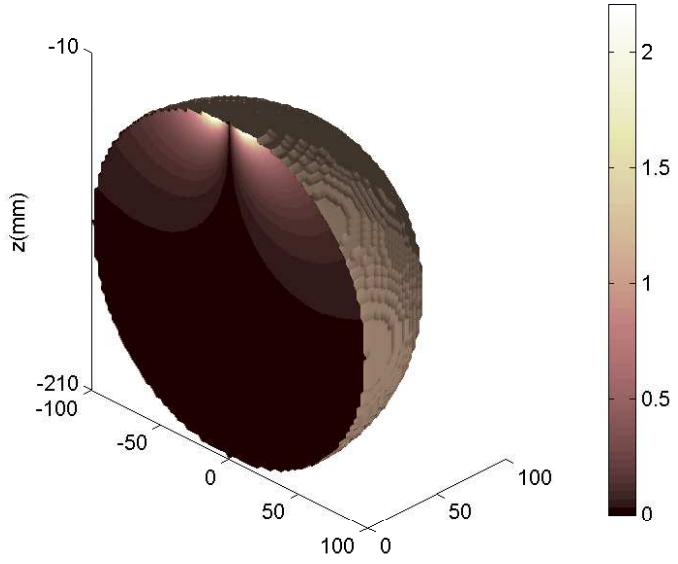

(b)

Figure 5.11: Induced current density distribution (A/m^2) inside the homogeneous head model,(a) displacement currents, (b) conduction currents at 10 MHz operating frequency.

5.2.3 Spherical concentric shell model of the head

The simulations of spherical model is improved by using concentric spherical shell models. Figure 5.12 shows the current density distributions for an operating frequency of 10 MHz. Since the electrical conductivity of CSF is very high, the induced currents are very high inside this tissue. Like the CSF, skin is the tissue closest to the excitation point, therefore the induced currents in skin is high as well.

5.2.4 Realistic Head Model

The realistic head model is constructed as explained previously. The model consists of seven tissues, CSF, gray matter, white matter, skin, muscle, fat and skull. The model resolution is chosen as 1 mm and the model consists of 220x175x185 cubic cells. The excitation source is a circular coil placed 1 cm above the head tissue and carries a sinusoidal current of 1 Ampere.

The solution of the scalar potential ϕ for a 50 kHz operating frequency is obtained after 400 iterations of the SOR algorithm neglecting the propagation effects. The weighting factor is chosen as 1.8 which is found to be the maximum over-relaxation that can be applied without divergence in solutions. For demonstration purposes, the scalar potential ϕ on the 75^{th} z-slice is presented in Figure 5.13.

The induced currents caused by $\nabla\phi$[2] and $\mathbf{A}$ can be observed individually and are presented in Figure 5.14. Since the coil is placed on the transverse plane, the A_z component is zero. The induced current distribution is shown in Figure 5.15. The magnitude plots (color and vector representations) are given in Figure 5.16 and Figure 5.17, respectively. The total induced currents inside the head model are presented in Figure 5.17 and Figure 5.18. The sensitivity of the coil on the z-axis is minimum, as expected.

[2] when the displacement currents are neglected, the scalar potential ϕ has only the imaginary component, thus $\nabla\phi$ will also be imaginary. The figures (5.14-5.19) shows the imaginary component of $\nabla\phi$.

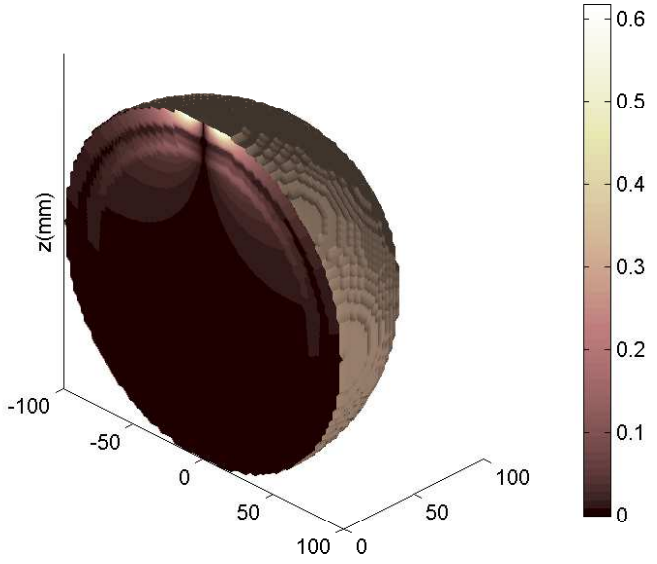

(a)

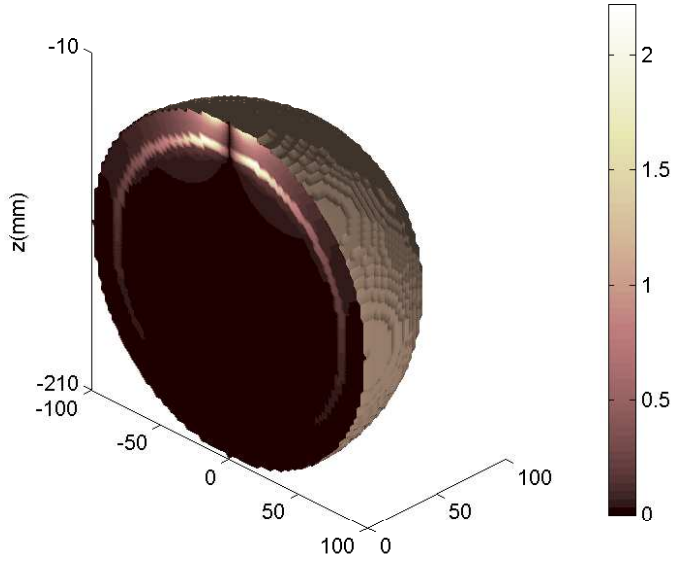

(b)

Figure 5.12: Current density distribution (A/m^2) inside the concentric shell model of the head,(a) displacement currents, (b) conduction currents at 10 MHz operating frequency.

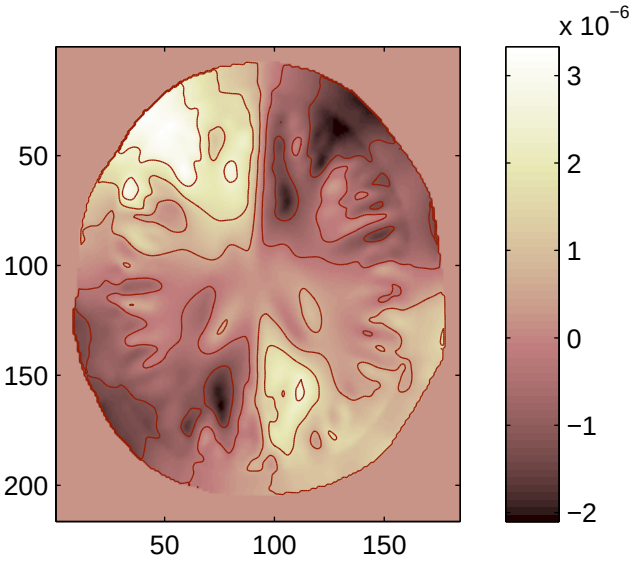

Figure 5.13: The scalar potential distribution ϕ inside the realistic head model at 50 kHz operating frequency (75^{th} slice). The transmitter coil is 1 turn, carries 1 Ampere sinusoidal current and is placed 1 cm above the head.

5.2.5 Intracranial Hemorrhage Model

To model the hemorrhage inside the head, a small sphere is placed inside the head. The blood conductivity and permittivity values are assigned as the electrical properties of this sphere. The operating frequency is chosen as 1 MHz in order to achieve a high contrast between the electrical properties of these tissues. In Figure 5.20 and Figure 5.21, the assigned conductivity distribution and the induced current densities are presented. The maximum current density of the hemorrhage tissue is found to be $7mA/m^2$ which is 10 times lower than the maximum current density inside the head. The induced currents are high at skin and CSF tissues, since the first one is closer to the excitation and the latter one has a high conductivity.

5.2.6 Cerebral Oedema Model

The cerebral oedema inside the head is again modeled as a sphere placed in the head. There are several studies that had modeled this type of anomaly but still the electrical properties of this tissue is not clear. The head model formed by Netz *et al.* was separating the brain hemispheres and filling NaCl solutions

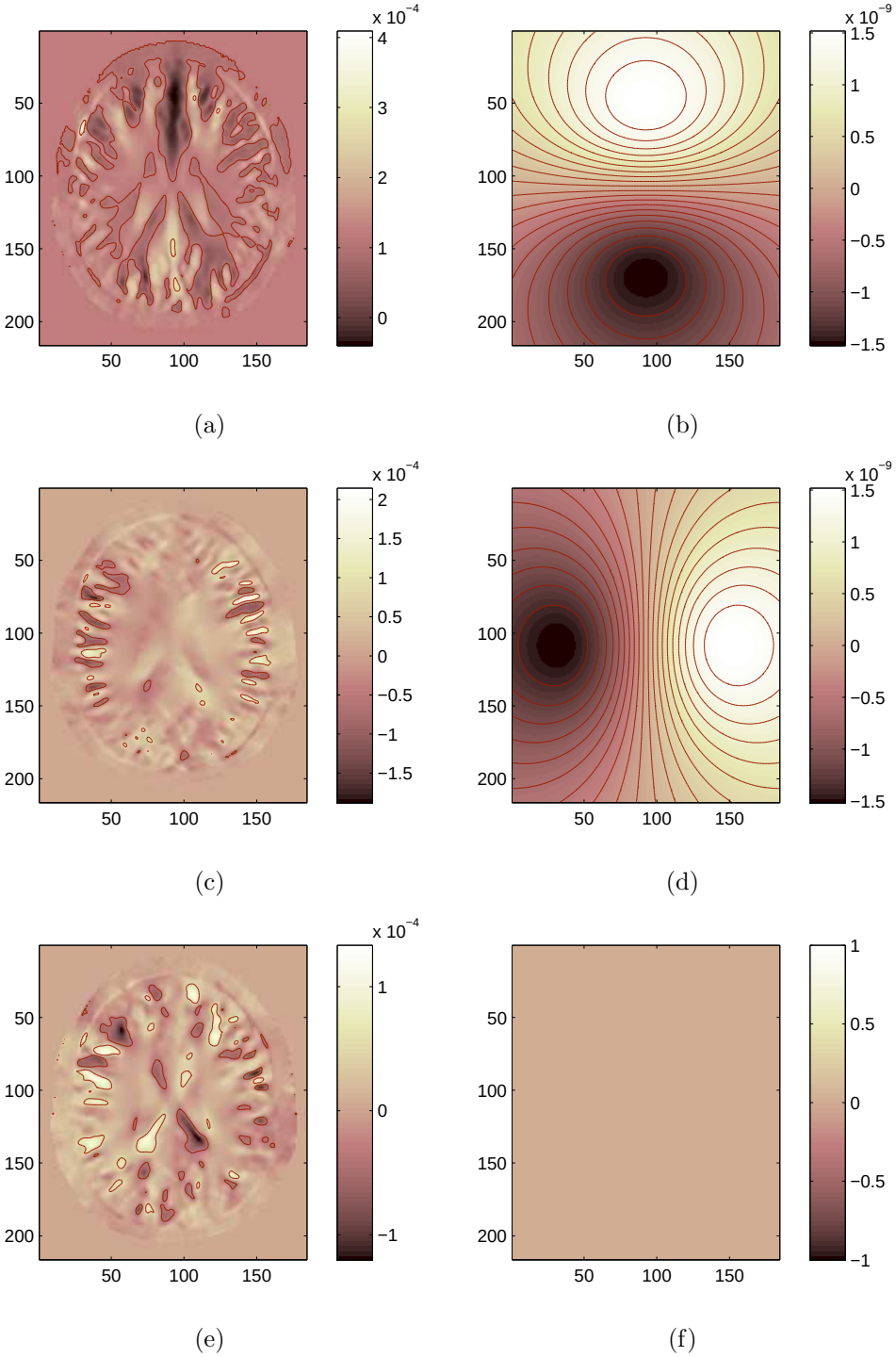

Figure 5.14: -$\nabla\phi$ and -j$\mathbf{A}$ distribution at an operating frequency of 50 kHz (a) $\frac{\partial\phi}{\partial x}$, (b) $\mathbf{A}_x$, (c) $\frac{\partial\phi}{\partial y}$, (d) $\mathbf{A}_y$, (e) $\frac{\partial\phi}{\partial z}$, (f) $\mathbf{A}_z$. The 1 turn transmitter coil is placed 1 cm above the head phantom and carries 1 Ampere.

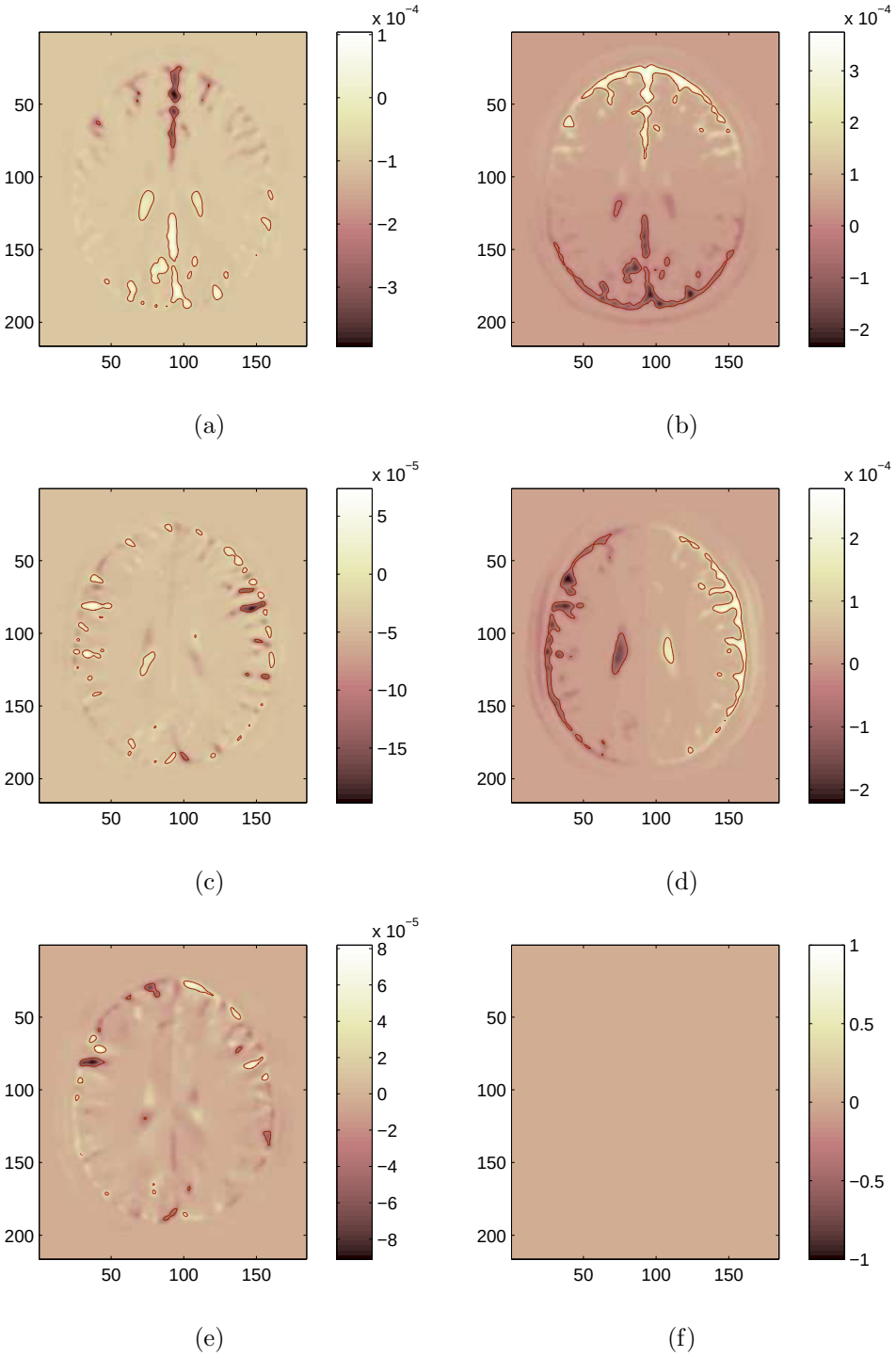

Figure 5.15: $-\sigma\nabla\phi$ and $-\sigma jw\mathbf{A}$ distribution (A/m^2) at an operating frequency of 50 kHz . (a) -$\sigma\frac{\partial\phi}{\partial x}$, (b) -$\sigma jw\mathbf{A}_x$, (c) -$\sigma\frac{\partial\phi}{\partial y}$, (d) -$\sigma jw\mathbf{A}_y$, (e) -$\sigma\frac{\partial\phi}{\partial z}$, (f) -$\sigma jw\mathbf{A}_z$. The 1 turn transmitter coil is placed 1 cm above the head phantom and carries 1 Ampere.

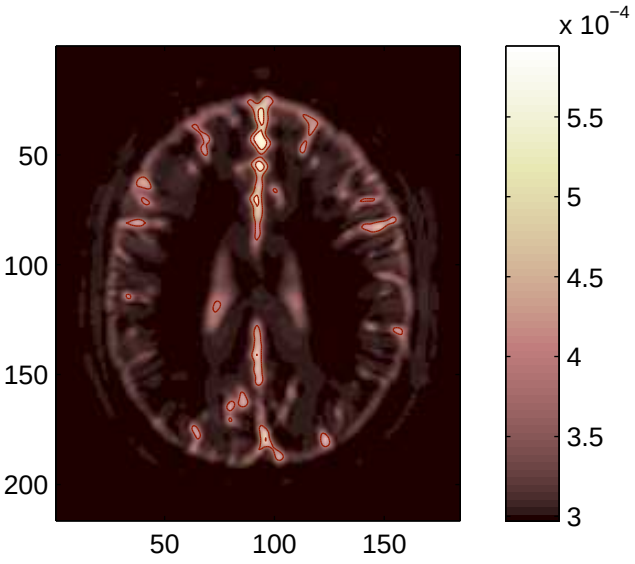

(a)

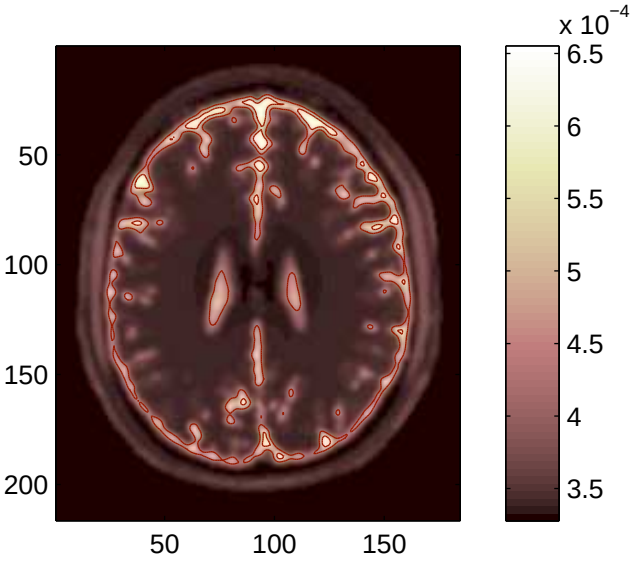

(b)

Figure 5.16: The magnitudes of the current components at 50 kHz operating frequency: (a) $|\sigma\nabla\phi|$, (b) $|\sigma jw\mathbf{A}|$ distribution (A/m^2) . The 1 turn transmitter coil is placed 1 cm above the head phantom and carries 1 Ampere.

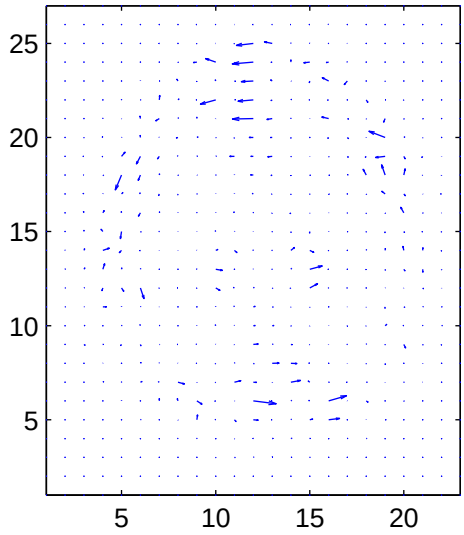

(a)

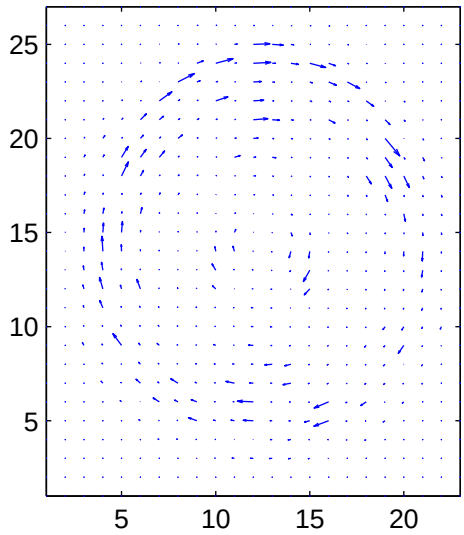

(b)

Figure 5.17: Vector plots of the current density components at 50 kHz operating frequency: (a) $-\sigma\nabla\phi$, (b) $-w\sigma\mathbf{A}$ distribution (A/m^2). The 1 turn transmitter coil is placed 1 cm above the head phantom and carries 1 Ampere.

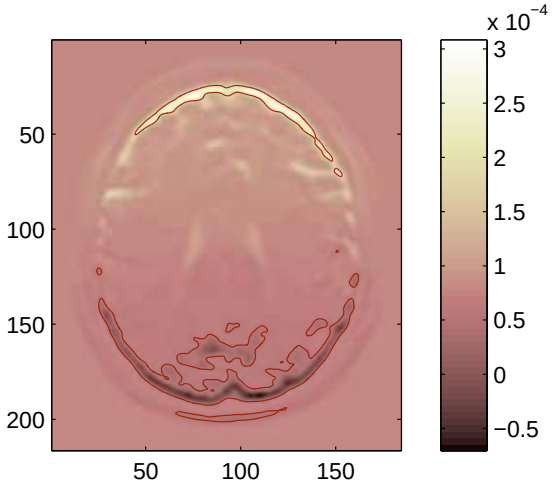

(a)

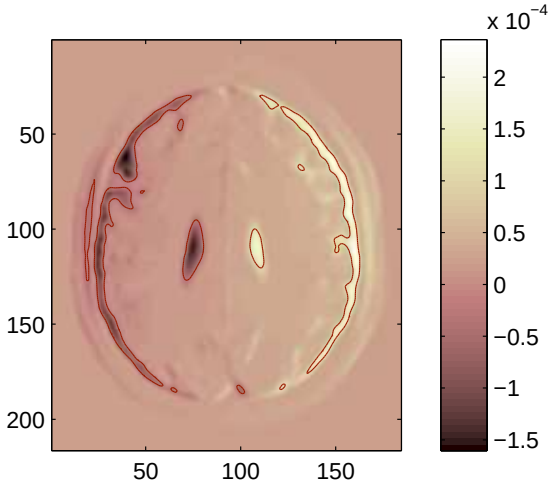

(b)

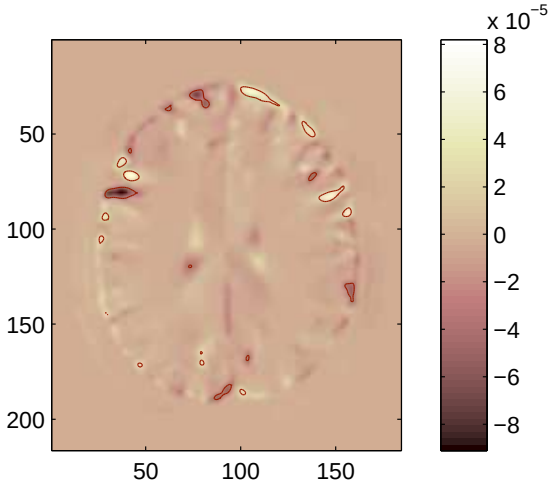

(c)

Figure 5.18: The three components of the total current density $\mathbf{J} = \sigma(-\nabla\phi - jw\mathbf{A})$ distribution (A/m^2) at 50 kHz operating frequency: (a) J_x, (b) J_y, and (c) J_z. The 1 turn transmitter coil is placed 1 cm above the head phantom and carries 1 Ampere.

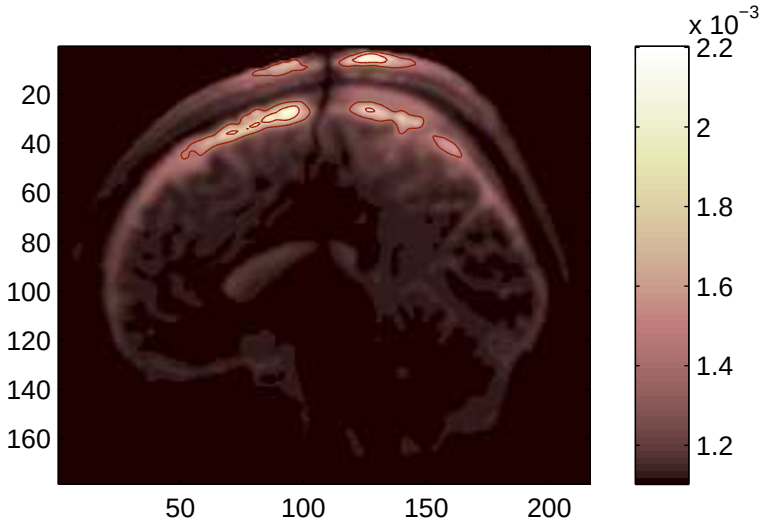

(a)

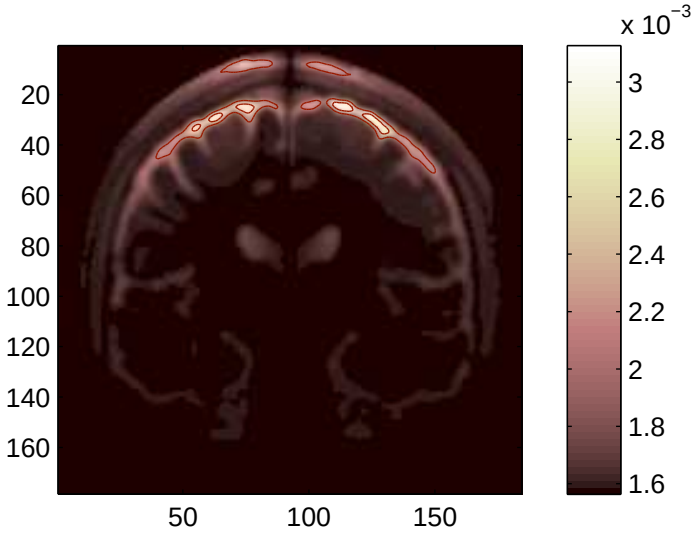

(b)

Figure 5.19: The magnitude of the total current density **J** distribution (A/m^2) at 50 kHz operating frequency on the other two orthogonal slices. (a) y-slice, (b) x-slice below the sensor. The 1 turn transmitter coil is placed 1 cm above the head phantom and carries 1 Ampere.

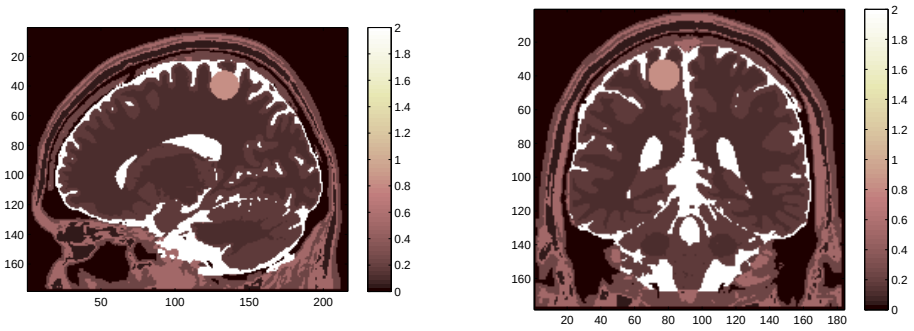

(a) (b)

Figure 5.20: Electrical conductivity distribution of intracranial hemorrhage model inside the head model.

with different concentrations to simulate the normal and oedematous tissue in the brain [25]. The oedematous hemisphere was taken as half of the conductivity value corresponding to healthy hemisphere. Spherical modeling of this oedema also simulated by Merwa *et al.* [67]. They have chosen the electrical conductivity of the oedema as twice the value of white matter conductivity and electrical permittivity as half of the white matter permittivity. Thus, the model is exactly the same as in Figure 5.20, except the change in the electrical properties.

Figure 5.25 shows the impedance change when the distance between the coil and the surface of the head is increased. The coil has 100 turns and carries a current of 1 Ampere. The operating frequency is 1 MHz. The difference between the impedance value of the oedema and the hemorrhage tissues are found to be $100\mu\omega$. The perturbation of the impedance change is found to be 1.39%.

5.3 Safety Considerations

To reveal the safety conditions for this technique, the effects of the electromagnetic waves to the human body should be investigated in a wide frequency range. For the current imaging modality, the operating frequency is assumed to in the 10 kHz-100 MHz range. Generally radiation in this range is non-ionizing radiation and the possible effects are heating through the tissues caused from

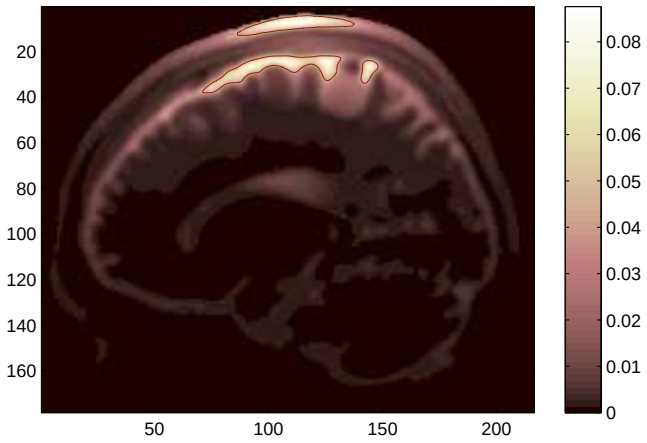

(a)

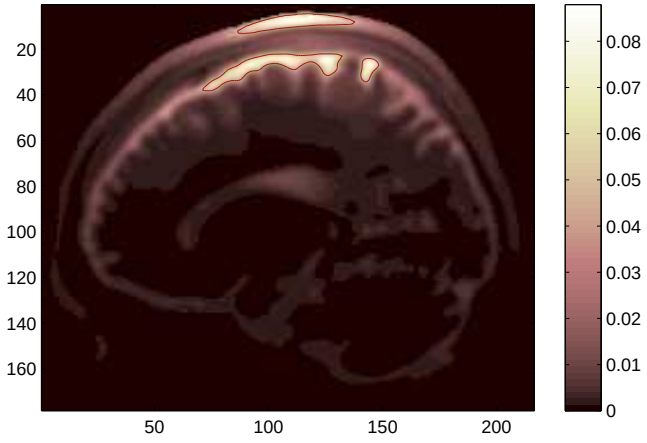

(b)

Figure 5.21: Induced current density distribution (A/m^2) inside the (a) intracranial hemorrhage model and, (b) cerebral oedema model at 1 MHz. The 1 turn transmitter coil is placed 1 cm above the head phantom and carries 1 Ampere.

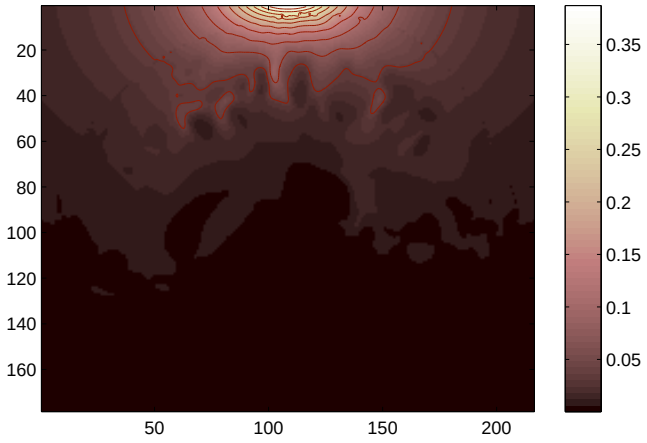

(a)

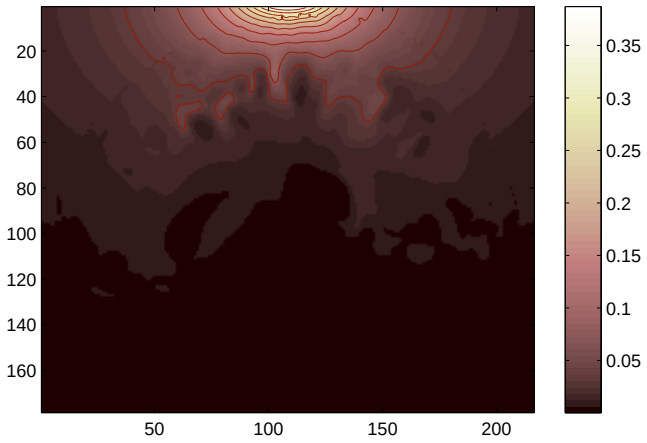

(b)

Figure 5.22: Electric field strengths (V/m) (a) intracranial hemorrhage model and, (b) cerebral oedema model at 1 MHz. The 1 turn transmitter coil is placed 1 cm above the head phantom and carries 1 Ampere.

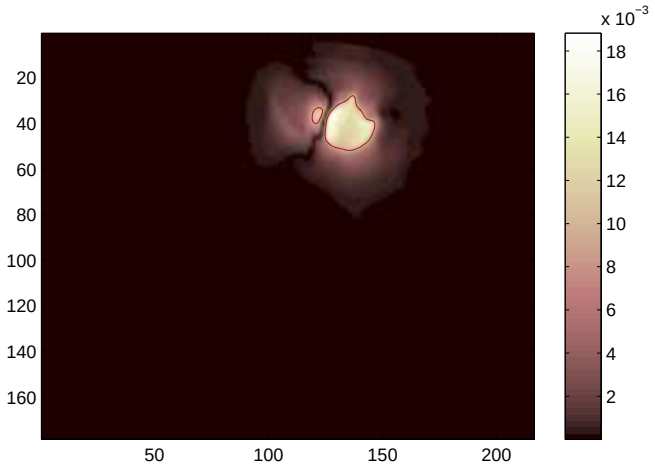

(a)

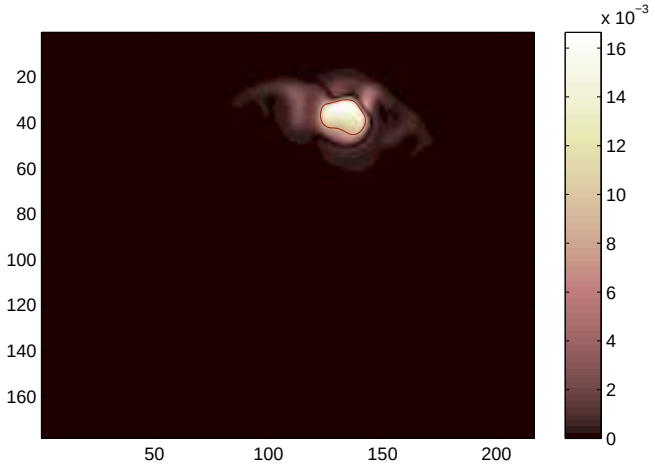

(b)

Figure 5.23: Difference of (a) the electric field strength distribution (V/m) and, (b) the induced current density distribution (A/m^2) between the intracranial hemorrhage and cerebral oedema model at 1 MHz. The 1 turn transmitter coil is placed 1 cm above the head phantom and carries 1 Ampere.

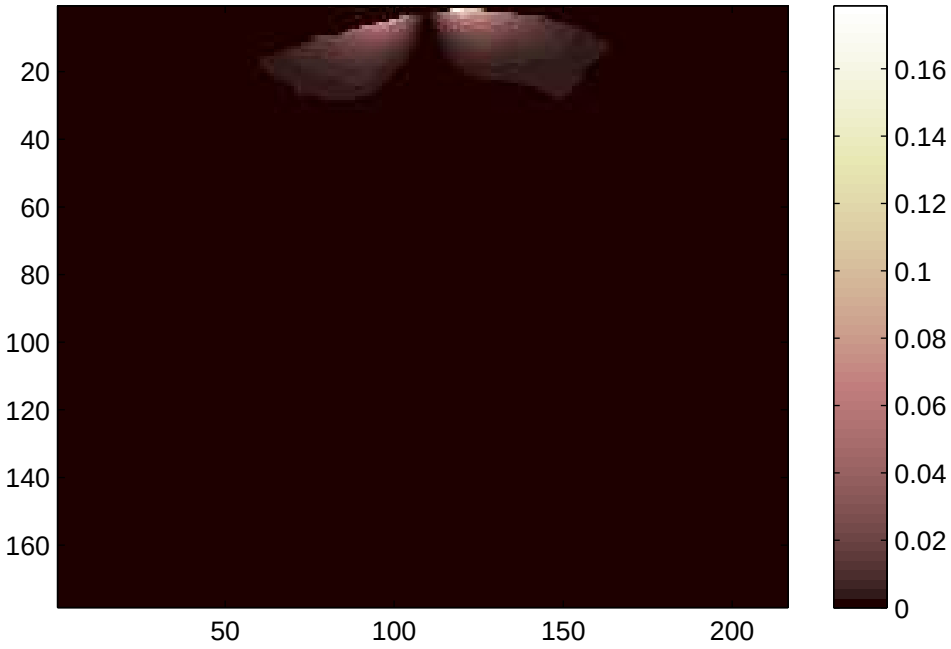

Figure 5.24: Sensitivity map of the coil according to the reciprocity theorem (derived in 3.41). The 1 turn transmitter coil is placed 1 cm above the head phantom and carries 1 Ampere.

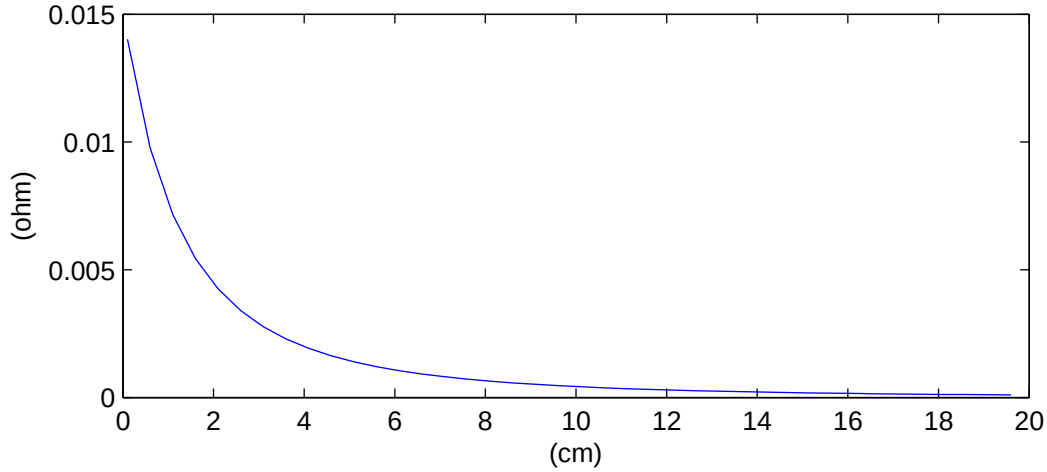

Figure 5.25: The impedance change of the coil (Ω) as the distance between the coil and the surface of the head is increased. The coil has 100 turns and carries 1 Ampere. The operating frequency is 1 MHz.

Table 5.2: Exposure Limits for persons not classed as RF and microwave exposed workers (Including the General Public).

Frequency (MHz)	Rms Electric Field Strength (V/m)	Rms Magnetic Field Strength (A/m)	Averaging Time (min)
0.003-1	280	2.19	6
1-10	280/f	2.19/f	6
10-30	28	2.19/f	6
30-300	28	0.073	6

the flow of induced currents. Other effects resulting cancer development have been demonstrated in animals. The maximum allowable electric field and magnetic field strengths in human body are given in Table 5.2 for the 3 kHz-300 MHz frequency range [48].

In this study, the safety conditions are studied for a specific coil configuration (Circular coil of radius 1 cm at 1 cm distance from the head. The coil carries a sinusoidal current of 1A) nearby the head. The excitation frequency in chosen to be 50 kHz, 1 MHz and 100 MHz. For an operating frequency of 50 KHz, the maximum electric field strength is found to be $\simeq 30mV/m$ which is lower than the safety limit (280 V/m) (6-min time-averaged). Similarly, for an excitation frequency of 1 MHz, the electric field strength is found $\simeq 600mV/m$ which is still much lower than the safety limit (280 V/m). However, at 100 MHz the electric field strength inside the skin tissue is greater than $\simeq 100V/m$ which is much more than the safety limit (28 V/m) at that frequency.

Consequently, for that specific coil configuration, it looks feasible to operate in the safe mode up to 10 MHz. However, if the operating frequency is increased, for example, to 50 MHz or higher, the coil configuration parameters should be adjusted to achieve safety.

CHAPTER 6

CONCLUSIONS AND DISCUSSIONS

6.1 Summary

In this study, the goals are (1) to solve the induced current density distribution inside the realistic head model resulting from a sinusoidal excitation via a transmitter coil and (2) to calculate the impedance change of the same coil due to the induced current distribution inside the head. For these purposes, first, a realistic head model is formed and the electrical properties of the model (conductivity and permittivity) is assigned as a function of frequency. The solution method is based on the over-relaxation type algorithms. The validity of the quasi-stationary assumptions are explored for a wide frequency range specifically for the head tissues.

The novel contributions of this study are,

- The 7-tissue multi-frequency realistic head model is used in the simulations. In the literature, simulations are only realized for simple geometries in order to test the experimental setups.

- It is found that displacement currents should not be neglected for the head applications. Although in earlier studies the displacement currents are taken into account (for torso applications, [**?**]), in the recent studies the displacement currents are ignored. In this study, the importance of the displacement currents are emphasized especially for the head applications.

- Electrical impedance spectrums of body tissues in a predefined frequency band are investigated and optimum frequencies for different regions of the body are determined. Some preliminary inferences are established for the ongoing multi-frequency studies.

- A possible clinical application area is determined. Distinguishing the intracranial hemorrhage from the cerebral oedema inside the head seems promising.

6.2 Conclusions

6.2.1 Quasi-stationary

The displacement currents through the skin tissue are dominant even at low frequencies (at 10 kHz it is 6 times greater than the conduction currents). Since the skin is the closest tissue to the sensor, the displacement currents should not be neglected even at low frequencies. Also the displacement currents through the gray and white matter should not be neglected for frequencies greater than 10 kHz. The realistic head model simulations showed that induction and propagation effects are negligible for the frequencies lower than 10 MHz. Therefore numerical solution of only the scalar potential is sufficient to obtain the solutions. This simplification not only reduces the excessive size of the solution domain, but also reduces the number of unknowns by a factor of 4. In the higher frequencies $> 10MHz$, however, the induction and propagation effects becomes more important.

6.2.2 Applications

The electrical properties of CSF is very different (conductivity is high, permittivity is low when compared with the other tissues of the brain). Thus, diagnosing some abnormalities in this tissue seems a promising application.

It is observed that, for each frequency there is a conductivity contrast relative to blood. Thus dynamic monitoring of hemorrhage at any frequency

seems feasible. In this thesis study, the frequency range 1 - 10 MHz is proposed for hemorrhage applications and it is tested at 1 MHz. The impedance change of the coil due to the hemorrhage to intracranial oedema is found to be 100 $\mu\Omega$. Therefore, the impedance change is found to be around 1% between two cases.

Apart from the diagnosis of hemorrhage, respiratory system monitoring can also be attempted, as the deflated and inflated lung conductivity contrast is high. Similarly, circulatory system monitoring is also applicable. For head tissues it is desirable to work with $> 1MHz$ in order to distinguish the soft tissues of the brain (cerebellum, gray and white matter).

6.3 Future Work

Future works can be listed as,

- The forward problem solution is time consuming. New methods should be investigated, especially to cope with the coil arrays.
- Other ways, implementing the solver on a hardware chip, should be explored to speed up solution. Also fast processors (Graphic cards, Play Stations, etc.) can be programmed to boost up the speed, as well.
- Up to now direct solution methods are used, since they are less memory consuming and much more controllable. However, for future studies, other solution methods should be used and different solver types should be compared.
- Absorbing boundary conditions can be implemented in order to reduce the solution region for high frequency applications.
- Up to now, limited number of image reconstruction techniques have been implemented. Novel algorithms can be developed to increase the imaging performance.
- There are still shortage on the electrical properties of pathological tissues. Therefore these data sets should be formed for the desired frequency

band. Moreover, anisotropic data even for muscles, brain and bones are not still available to simulate the anisotropy in conductivity.

REFERENCES

[1] J. C. Maxwell, *A Dynamical Theory of the Electromagnetic Field,* Philosophical Transactions of the Royal Society of London, 155, pp. 459-512, 1865.

[2] R. Plonsey, R. Collin, *Principles and Applications of Electromagnetic Fields* New York: McGraw-Hill Book Company, 1961.

[3] Abramowitz and Stegun, *Handbook of mathematical functions with formulas, graphs and mathematical tables,* Washington:Govt. Print. Off., 1964, pp. 590-592.

[4] W. R. Smythe, *Static and dynamic electricity,* New York:McGraw Hill, 1965, pp. 290-291.

[5] P. P. Tarjan, "Electrodeless Measurements of Resistivity Fluctuations in the Human Torso and Head," Syracuse University, Syracuse, USA, Ph. D. thesis, 1968.

[6] P. P. Tarjan and R. McFee, "Electrodeless Measurements of the Effective Resistivity of the Human Torso and Head by Magnetic Induction," *IEEE Tran. Bmed. Eng.*, Vol BME-15, No 4, October 1968.

[7] J. R. Mortarelli, "A Generalization of the Geselowitz Relationship Useful in Impedance Plethysmographic Field Calculations," *IEEE Tran. Bmed. Eng.*, Vol BME-27, No 11, November 1980.

[8] J. R. Wait, *Geo-Electromagnetism.* Academic Press, New York, 1982.

[9] J. H. Tripp, "Physical concepts and mathematical models," *Biomagnetism an Interdisciplinary Approach.*, Ed: S. J. Williamson, G. L. Romani, L. Kaufman, I. Modena, pp. 101-139, 1983.

[10] D. C. Barber and B. H. Barber, "Applied Potential Tomography," *J. Phys. E: Sci. Instrum.* Vol. 17, pp 723-733, 1984.

[11] D. Isaacson, "Distinguishability of conductivities by electric current tomograph," *IEEE Trans. Med. Im.* Vol. 5, pp. 91-95, 1986.

[12] D. Isaacson, "Distinguishability of conductivities by electric current computed tomography," *IEEE Trans. Med. Imag.*, 5: 91-95, 1986.

[13] S. Webb, "The Physics of Medical Imaging," *IOP Publising Limited*, Bristol, 1988.

[14] L. W. Hart, H. W. Ko, J. H. Meyer, JR., D. P. Vasholz, R. I. Joseph, "A Noninvasive Electromagnetic Conductivity Sensor for Biomedical Applications," *IEEE Tran. Bmed. Eng.*, Vol 35, No 12, December 1988.

[15] A. J. Surowiec, S. S. Stuchly, J. R. Barr, A. Swarup, "Dielectric Properties of Breast Carcinoma and the Surrounding Tissues," *IEEE Tran. Bmed. Eng.*, Vol 35, No 4, April 1988.

[16] J. W. H. Meijs, O. Weier and M. J. Peters, "On the accuracy of boundary element method," *IEEE Tran. Bmed. Eng.*, Vol 36, pp 1038-1049,1989.

[17] G. H. Golub and C. F. Van Loan, *Matrix Computations.* Baltimore: Johns Hopkins University Press, second edition, 1989.

[18] A. A. Kaufman and G. V. Keller, *Induction Logging.* Elsevier Science Publishers, Amsterdam, Netherland, 1989.

[19] Y. Z. Ider, N. G. Gencer, E. Atalar and H. Tosun, "Electrical Impedance Tomography of Translationally Uniform Cylindrical Objects with General Cross Sectional Boundaries," *IEEE Transactions Medical Imaging*, Vol. 37, No 6, pp. 624-631, March 1990.

[20] M. Sadiku, *Numerical techniques in electromagnetics,* CRC Press, 1992, pp. 23-24.

[21] B. H. Brown and D. C. Barber, "Electrical Impedance Tomography," *Clin. Phys. Physiol. Meas.* Vol. 13, Suppl. A, p. 207, 1992.

[22] W. R. Purvis, R. C. Tozer and I. L. Freeston, "Induced Current Impedance Imaging," *IEEE proc.*, pt. A, Vol.140, No.2, pp. 135-141, March 1993.

[23] N. G. Gencer. "Electrical Impedance Tomography Using Induced Currents," METU, Ankara, Turkey, Ph. D. Thesis, 1993.

[24] S. Al-Zeibak and N. Saunders, "A feasibility study of in vivo electromagnetic imaging," *Phys. Med. Biol.*, vol. 38, pp. 151-160, 1993.

[25] J. Netz, E. Forner, and S. Haagemann, "Contactless impedance measurement by magnetic induction- a possible method for investigation of brain impedance," *Physiol. Meas.*, Vol. 14, pp. 463-471, 1993.

[26] M. S. Bazaraa, H. D. Sherali, and C. M. Shetty, *Nonlinear Programming Theory and Algorithms.* John Wiley & Sons, Inc., 1993.

[27] N. G. Gencer, M. Kuzuoglu and Y. Z. Ider, "Electrical impedance tomography using induced currents," *IEEE Tran. Med. Im.*, vol. 30, no. 2, June 1994.

[28] E. T. McAdams, J. Jossinet, "Tissue impedance: a historical overview," *Physiol. Meas.* Vol. 16, A1-A13, 1995.

[29] I. L. Freeston and R. C. Tozer, "Impedance Imaging using Induced Currents," *Physiol. Meas.* Vol. 16, (suppl. 3A), pp. 257-266, 1995.

[30] M. Osypka, E. Gersing, "Tissue impedance spectra and the appropriate frequencies for EIT," *Physiol. Meas.*, Vol. 16, A49-A55, 1995.

[31] S. Gabriel S, R. W. Lau, C. Gabriel, Dielectric properties of biological tissues, 1. Literature survey, *Phys Med Biol*, 41, pp. 2231-2249, 1996.

[32] C. Gabriel, S. Gabriel, E. Corthout, Dielectric properties of biological tissues, 2. Measurements, *Phys Med Biol*, 41, pp. 2251-2269, 1996.

[33] S. Gabriel, R. W. Lau, C. Gabriel, The dielectric properties of biological tissues: III. Parametric models for the dielectric spectrum of tissues, *Phys Med Biol*, 41, pp. 2271-2293, 1996.

[34] N. G. Gencer, Y. Z. Ider and S. J. Williamson, "Electrical Impedance Tomography: Induced Current Imaging Achieved with a Multiple Coil System," *IEEE Trans. medical imaging* , Vol. 43, No:2, pp. 139-149, 1996.

[35] J. P. Morucci and B. Rigaud, "Biolectrical Impedance Techniques in Medicine," In John R. Bourne, Editor, *Crit. Rev. Biomed. Eng.* Vol. 24 (4-6), 655-677, 1996.

[36] A. J. Peyton, Z. Z. Yu, S Al-Zeibak, J. Ferreira, J. Velez, F. Linhares, A. R. Borges, H. L. Xiong, N. H. Saunders, M. S. Beck "An overview of electromagnetic inductance tomography: description of three different systems" *Meas. Sci. Technol.*, 7, pp. 261-271, 1996

[37] M. N. Tek and N. G. Gencer, "A new 3D FEM formulation for the Solution of Potential Fields in Magnetic Induction Problems," *IEEE EMBS 19th Annual International Conf.*, 1997.

[38] K. Boone, D. Barber and B. Brown, "Imaging with electricity: Report of the European Concerted Action on Impedance Tomography," *Journal of Med. Eng. Tech.* Volume 21, Number 6, pp 201-232, 1997.

[39] A. Korzhenevskii, V. Cherepenin, Magnetic induction tomography," *J. Commun. Tech. Electron.*, vol. 42, pp. 46974, 1997.

[40] Z. Z. Yu, A. J. Peyton, L. A. Xu, M. S. Beck Electromagmetic inductance tomography (EMT): sensor electronics and image reconstruction algorithm for a system with a rotatable parallel excitation field IEE Proc. Sci. Meas. Technol., Vol. 145, No.1, pp. 20-25, 1998

[41] N. G. Gencer and M. N. Tek, "Imaging Tissue Conductivity via Contactless Measurements: A Feasibility Study," *TUBITAK Elektrik Journal*, Vol. 6, No.3, pp. 183-203, 1998.

[42] W. H. Press, B. P. Flannery, S. A. Teukolsky, W. T. Vetterling "Numerical Recepies in C" Cambridge University Press, 1998.

[43] D. L. Collins, A. P. Zijdenbos, V. Kollokian, J. G. Sled, N. J. Kabani, J. Holmes, A. C. Evans, "Design and construction of a realistic digital brain phantom," *IEEE T Med Img*, 1998, Vol.17 No.3 pp. 463-468.

[44] H. Griffiths, W. R. Stewart, and W. Gough, "Magnetic induction tomography. a measuring system for biological tissues," *Ann. N Y Acad. Sci.*, vol. 873, pp. 335-345, 1999.

[45] N. G. Gençer and M. N. Tek, "Forward problem solution for electrical conductivity imaging via contactless measurements," *Phys. Med. Biol.*, Vol. 44, pp. 927–940, April 1999.

[46] N. G. Gençer and M. N. Tek, "Electrical conductivity imaging via contactless measurements," *IEEE Transactions on Medical Imaging*, vol. 18, pp. 617–627, July 1999.

[47] A. V. Korjenevsky and V. A. Cherepenin, "Progress in realization of magnetic induction tomography", *Ann. N Y Acad. of Sci.*, v. 873, pp 346-352, 1999

[48] "Limits of Human Exposure to Radiofrequency Electromagnetic Fields in the Frequency Range from 3 kHz to 300 GHz - Safety Code 6", *Ann. Minister of PublicWorks and Government Services*, Canada 1999.

[49] A. Korjenevsky, V. Cherepenin, and S. Sapetsky, "Magnetic induction tomography: Experimental realization," *Physiol. Meas.*, Vol. 21, pp. 89–94, 2000.

[50] A. Korjenevsky, S. Sapetsky, Methods of measurements and image reconstruction in magnetic induction tomography," Proc. 2nd EPSRC Engineering Network Meeting on Biomedical Applications of EIT, 57 April, London, 2000.

[51] T. Ahmad, N. Gencer, Development of a data acquisition system for electrical conductivity images of biological tissues via contactless measurements," Proc. 23rd EMBS International Conferance, 2528 October, stanbul, 2001.

[52] H. Scharfetter, H. Lackner, and J. Rosell, "Magnetic induction tomography: Hardware for multi-frequency measurements in biological tissues," *Physiol. Meas.*, vol. 22, pp. 131–146, 2001.

[53] J. Rosell, R. Casanas, H. Scharfetter, "Sensitivity maps and system requirements for magnetic induction tomography using a planar gradiometer," *Physiol. Meas.*, Vol. 22, pp. 121-130, 2001.

[54] S. Zlochiver, M. M. Radai, S. Abboud, "Injected versus induced current approaches for monitoring brain cryosurgery in a two-dimentional model of the head," *Proc. XI Int. Conf. Electr. Bioimp.*, 665-668, 2001.

[55] H. Griffiths, "Magnetic Induction Tomography", *Meas. Sci. Technol.* ,12, pp. 1126-1131, 2001

[56] A. Morris, H. Griffiths, W. Gough, "A numerical model for magnetic induction tomographic measurements in biological tissues," *Physiol. Meas.*, Vol. 22, pp. 113-119, 2001.

[57] S. Watson, R. J. Williams, H. Griffiths, W. Gough, A. Morris, "Frequency downconversion and phase noise in MIT," *Physiol. Meas.*, Vol. 23, pp. 189-194, 2002.

[58] H. Scharfetter, P. Rui, M. Populo, J. Rosell, "Sensitivity maps for low-contrast perturbations within conducting background in magnetic induction tomography," *Physiol. Meas.*, Vol. 22, pp. 195-202, 2002.

[59] H. Scharfetter, R. Casanas, J. Rosell, "Biological Tissue Characterization by Magnetic Induction Spectroscopy (MIS): Requirements and Limitations," *IEEE Tran. Bmed. Eng.*, Vol 50, No 7, July 2003.

[60] R. Merwa, K. Hollaus, B. Brandstatter, H. Scharfetter, "Numerical solution of the general 3D eddy current problem for magnetic induction tomography (spectroscoby)," *Physiol. Meas.*, Vol. 24, pp. 545-554, 2003.

[61] B. U. Karbeyaz, N. Gencer, "Electrical Conductivity Imaging via Contactless Measurements: An Experimental Study," *IEEE Tran. Bmed. Eng.*, Vol. 22, no 5, May 2003.

[62] W. Gough, "Circuit for the measurement of small phase delays in MIT," *Physiol. Meas.*, Vol. 24, pp. 501-507, 2003.

[63] S. Watson, R. J. Williams, H. Griffiths, W. Gough, A. Morris, "Magnetic induction tomography: phase versus vector-voltmeter measurement techniques," *Physiol. Meas.*, Vol. 24, pp. 555-564, 2003.

[64] D Haemmerich, ST Staelin, JZ Tsai, S Tungjitkusolmun, DM Mahvi, JG Webster, "In vivo Electrical Conductivity of Hepatic Tumours," *Physiol. Meas.*, Vol 24, pp 251-260, 2003.

[65] S. Watson, A. Morris, R. J. Williams, H. Griffiths, W. Gough, "A primary field compensation scheme for planar array magnetic induction tomography," *Physiol. Meas.*, Vol. 25, pp. 271-279, 2004.

[66] C. H. Riedel, M. Keppelen, S. Nani, R. D. Merges, O. Dossel, "Planar system for magnetic induction conductivity measurement using a sensor matrix," *Physiol. Meas.*, Vol. 25, pp. 403-411, 2004.

[67] R. Merwa, K. Hollaus, O. Biro, H. Scharfetter, "Detection of brain oedema using magnetic induction tomography: a feasibility study of the likely sensitivity and detectability," *Physiol. Meas.*, Vol. 25, pp. 347-354, 2004.

[68] R. Casanas, H. Scharfetter, A. Altes, A. Remacha, P. Sarda, J. Sierra, R. Merwa, K. Hollaus, J. Rosell, "Measurement of liver iron overload by magnetic induction using a planar gradiometer: preliminary human results.," *Physiol. Meas.*, Vol. 25, pp. 315-323, 2004.

[69] K. Hollaus, C. Magele, R. Merwa, H. Scharfetter "Fast calculation of the sensitivity matrix in magnetic induction tomography by tetrahedral edge finite elements and the reciprocity theorem," *Physiol. Meas.*, Vol. 25, pp. 159-168, 2004.

[70] K. Hollaus, C. Magele, R. Merwa, H. Scharfetter, "Numerical Simulation of the Eddy Current Problem in Magnetic Induction Tomography for Biomedical Applications by Edge Elements," *IEEE Tran. on Magn.*, Vol 40, No 2, July 2004.

[71] H. Scharfetter, S. Rauchenzauner, R. Merwa, O. Biro, K. Hollaus, "Planar gradiometer for magnetic induction tomography (MIT): theoretical and experimental sensitivity maps for a low-contrast phantom," *Physiol. Meas.*, Vol. 25, pp. 323-333, 2004.

[72] H. Scharfetter, R. Merwa, K. Pilz, "A new type of gradiometer for the receiving circuit of magnetic induction tomography (MIT)," *Physiol. Meas.*, Vol. 26, pp. 307-318, 2005.

[73] R. Merwa, K. Hollaus, P. Brunner, H. Scharfetter, "Solution of the inverse problem of magnetic induction tomography (MIT)," *Physiol. Meas.*, Vol. 26, pp. 241-250, 2005.

[74] S. Watson, C. H. Igney, O. Dossel, R. J. Williams, H. Griffiths, "A comparison of sensors for minimizing the primary signal in planar-array magnetic induction tomography," *Physiol. Meas.*, Vol. 26, pp. 319-331, 2005.

[75] C. H. Igney, S. Watson, R. J. Williams, H. Griffiths, O. Dossel, "Design And Performance of A Planar-Array MIT System With Normal Sensor Alignment," *Physiol. Meas.*, Vol. 26, pp. 263-278, 2005.

[76] A. Taflove and S. C. Hagness, *Computational Electrodynamics The Finite-Difference Time-Domain Method,* Artech House, Inc., 2005, pp. 2-3.

[77] İ. E. Çolak, "An Improved Data Acquisition System For Contactless Conductivity Imaging," METU, M. Sc. Thesis, 2005.

[78] K. Ö. Özkan, "Multi-Frequency Electrical Conductivity Imaging Via Contactless Measurements," METU, M. Sc. Thesis, 2006.

APPENDIX A

FINITE DIFFERENCE METHOD

In essence, FD method is applied in order to convert the differential equations to simple algebraic equations. In order to achieve that the space is divided into grids and the unknown fields are assigned to a node on each grid. Afterwards the field equation on this node is written in terms of fields on neighboring nodes.

It is known from the Taylor's expansion that,

$$\psi_{x+h,y,z} = \psi_{x,y,z} + h\frac{d}{dx}\psi_{x,y,z} + \frac{1}{2}h^2\frac{d^2}{dx^2}\psi_{x,y,z} + \frac{1}{6}h^3\frac{d^3}{dx^3}\psi_{x,y,z} + ... \quad \text{(A.1)}$$

$$\psi_{x-h,y,z} = \psi_{x,y,z} - h\frac{d}{dx}\psi_{x,y,z} + \frac{1}{2}h^2\frac{d^2}{dx^2}\psi_{x,y,z} - \frac{1}{6}h^3\frac{d^3}{dx^3}\psi_{x,y,z} + ... \quad \text{(A.2)}$$

where the function ψ is evenly divided into grids of size h. Therefore when the computational domain is discretisized as above, it is easy to express the first

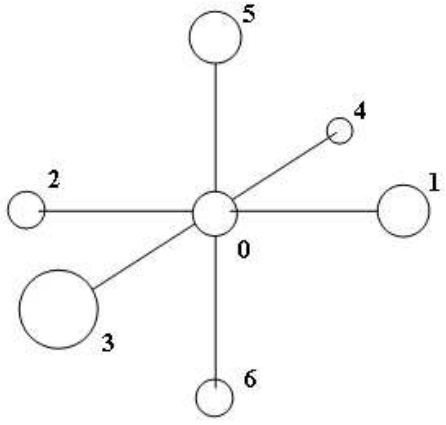

Figure A.1: The 7-point stencil.

and second derivatives as,

$$\frac{\partial \psi_{x,y,z}}{\partial x} = \frac{\psi_{x+h,y,z} - \psi_{x-h,y,z}}{2h} + O(h^2) \tag{A.3}$$

$$\frac{\partial^2 \psi_{x,y,z}}{\partial x^2} = \frac{\psi_{x+h,y,z} + \psi_{x-h,y,z} - 2\psi_{x,y,z}}{h^2} + O(h^2) \tag{A.4}$$

where ψ is a scalar quantity defined at each grid and $O(h^2)$ represents the higher order terms. If the higher order terms are dropped this usually leads to an acceptable approximation for the derivative of the function.

APPENDIX B

SOLUTION METHODS[1]

B.1 Jacobi Method

The Jacobi method is an iterative algorithm in order to solve a system of linear equations. The Jacobi iteration is,

$$\phi^{n+1} = \mathbf{D}^{-1} - ((\mathbf{L} + \mathbf{U})\phi^n + \mathbf{B}) \tag{B.1}$$

where **D**, **L**, and **U** represent diagonal, lower triangular, and upper triangular parts of the coefficient matrix **A** and n is the iteration count. The representation of the above iteration in terms of the matrix elements is given below,

$$\phi_i^{n+1} = \frac{1}{a_{ii}}(b_i - \sum_{j \neq i} a_{ij}\phi_j^n), \qquad i = 1, 2, .., n \tag{B.2}$$

Note that the computation of ϕ_i^{n+1} requires each element in ϕ^n for the computation. Therefore in Jacobi Method the physical memory needed for storage is at least double of the unknown elements. By using finite differences the iteration is very simplified since the equations are defined only in terms of neighboring unknown elements.

B.2 Gauss-Seidel Method

The Gauss-Seidel iteration is,

$$\phi^{n+1} = (\mathbf{D} - \mathbf{L})^{-1}(\mathbf{U}\phi^n + \mathbf{B}) \tag{B.3}$$

[1] The simulations are realized on a AMD Athlon XP 1.83GHz computer which has 1.5 GB of RAM, operates at 333MHz. The operating system of the computer is Mandrake 10.0 Linux and all the codes are implemented on MATLAB.

The element based approach of **??** is given below,

$$\phi_i^{n+1} = \frac{1}{a_{ii}}(b_i - \sum_{j<i} a_{ij}\phi_j^{n+1} - \sum_{j>i} a_{ij}\phi_j^n), \qquad i = 1, 2, .., n \tag{B.4}$$

In Gauss-Seidel iterations, the unknown fields are updated at each iteration. This means that no additional storage other than the unknown elements is required. The main difference between Jacobi and this method is this. Although this may seem unimportant, if large number of equation systems are considered, this method is very advantageous.

B.3 Successive Over-relaxation Method

Successive Over-relaxation (SOR) is the improved version of the Gauss-Seidel method where an additional relaxation parameter w is added to tune the convergence. The SOR iteration is defined by,

$$(\mathbf{D} + w\mathbf{L})\phi^{n+1} = (-w\mathbf{U} + (1-w)\mathbf{D})\phi^n + w\mathbf{B} \tag{B.5}$$

The iteration reduces to the Gauss-Seidel iteration for $w = 1$. As with the Gauss-Seidel method, the computation may be done in place, and the iteration is continued until the changes made by an iteration are below some tolerance. For symmetric, positive-definite matrices it choosing w between 0 and 2 will generally lead to convergence. $w < 1$ will lead to a slow convergence and $w > 1$ will lead to a fast convergence. Thus it is aimed to increase w as much as possible. The element based iteration of SOR is,

$$\phi_i^{n+1} = (1-w)\phi_i^n + \frac{w}{a_{ii}}(b_i - \sum_{j=1} a_{ij}\phi_j^{n+1} - \sum_{j=i+1} a_{ij}\phi_j^n), \qquad i = 1, 2, .., n \tag{B.6}$$